PHYSICAL REGULATION OF CELL SURFACE ACCESS AND CELL ADHESION BY MEMBRANE-ANCHORED HYALURONAN

A Dissertation

Presented to

The Academic Faculty

by

Patrick S. Chang

In Partial Fulfillment

of the Requirements for the Degree

Doctor of Philosophy in the

School of Physics

Georgia Institute of Technology

December, 2016

PHYSICAL REGULATION OF CELL SURFACE ACCESS AND CELL ADHESION BY MEMBRANE-ANCHORED HYALURONAN

Approved by:

Dr. Jennifer E. Curtis, Advisor
School of Physics
Georgia Institute of Technology

Dr. Andres J. Garcia
School of Mechanical Engineering
Georgia Institute of Technology

Dr. James C. Gumbart
School of Physics
Georgia Institute of Technology

Dr. Harold D. Kim
School of Physics
Georgia Institute of Technology

Dr. Peter Yunker
School of Physics
Georgia Institute of Technology

Date Approved: November 14, 2016

ACKNOWLEDGEMENTS

I would like to thank my advisor, Jennifer Curtis, for her guidance, encouragement and patience. I could not have done it without her. I am extremely lucky to have her as my mentor. I appreciate all the help and encouragement from all my classmates, lab mates and collaborators. I especially want to thank Dr. Louis McLane, whose work in our lab laid the foundation for my research. I also want to thank Dr. Dan Kovari, Wenbin Wei, Rebecca Keate, who helped me a lot along the way.

On a more personal note, I would like to thank my family for all of their supports and sacrifices, especially to my wife, Sonia. Leaving her family and friends to move to Atlanta for me was a big change. I don't think I could have made it through without her company in all these nights and days in the lab. I can feel her supports not only from her encouragement, but also from all the delicious lunch and dinner boxes she prepared every day. I am truly grateful.

TABLE OF CONTENTS

ACKNOWLEDGEMENTS III

LIST OF TABLES IX

LIST OF FIGURES X

LIST OF SYMBOLS AND ABBREVIATIONS XVII

SUMMARY XVIII

CHAPTER

1. Introduction 1
2. Background Information
    - 2.1 Hyaluronan 5
    - 2.2 Hyaluronan Binding Protein 6
    - 2.3 Pericellular Matrix 7
    - 2.4 Pericellular Matrix Functions 8
    - 2.5 Particle Transport through PCM 10
    - 2.6 PCM *in vivo* versus *in vitro* 10
    - 2.7 Focal Adhesions 11
    - 2.8 Focal Adhesion and Hyaluronan 13
    - 2.9 Focal Adhesion Area and Traction Force 14
3. Organization and Microstructure of the Pericellular Matrix
    - 3.1 Overview 15
    - 3.2 Materials and Methods
        - 3.2.1 Cell culture and sample preparation 16
        - 3.2.2 Particle exclusion assay 17
        - 3.2.3 GFPn labeling of hyaluronan 18
        - 3.2.4 Optical force probe assays 20
    - 3.3 Results

3.3.1 Traditional Particle Exclusion Assay characterization of cell lines……21
3.3.2 Quantitative Particle Exclusion Assay……..25
3.4 Discussion...……....28
3.5 Conclusion and Outlook……..32
4. CELL SURFACE ACCESS IS MODULATED BY TETHERED BOTTLEBRUSH PEOTEOGLYCANS
4.1 Overview…… ……..……34
4.2 Materials and Methods
4.2.1 Cell culture and sample preparation…….……37
4.2.2 Particle exclusion assay (PEA)…..…….……37
4.2.3 Time-dependent swelling of PCM…… ……38
4.2.4 Fluorescent protein labeling…… ……....…38
4.2.5 Optical force probe assays…… ……....39
4.2.6 Fluorescent aggrecan exchange assay…….....39
4.2.7 GFPn labeling of hyaluronan…… ……39
4.2.8 Chondroitin sulfate digestion assay……..40
4.3 Results and Discussion
4.3.1 PCM swells with increasing aggrecan concentration... ….40
4.3.2 PCM maximal extension occurs before bottlebrush saturation…… ……..43
4.3.3 Fluorescent aggrecan assay reveals free binding sites in PCM……...45
4.3.4 Bottlebrush-enriched PCM reduced mesh size and permeability to nanoparticles…… ……48
4.3.5 Increasing bottlebrush concentration drives PCM microstructure toward spatial uniformity…….……..52
4.3.6 Unbound aggrecan diffuses swiftly through the PCM……53
4.3.7 Electrostatic sequestration of positively charged ~20 kDa molecules in the PCM…… ……56
4.4 Conclusion and Outlook…… ……....61

5. Hyaluronan Mediated Cell Adhesion

5.1 Overview……..…63

5.2 Materials and Methods

5.2.1 Cell culture and sample preparation……64

5.2.2 Glass coverslip coating……..64

5.2.3 GFPn production and use…… ……..65

5.2.4 Transfection of fluorescent paxillin…… ……...65

5.2.5 Reflection Interference Contrast Microscopy… ……..66

5.2.6 Spinning disk apparatus…… ……66

5.2.7 Adhesion strength measurement…… ……..67

5.2.8 Enzyme treatment digesting PCM……..……68

5.2.9 Myosin II inhibition…… ……...69

5.2.10 HA synthase suppression……..……..69

5.3 Results

5.3.1 Hyaluronan is organized in patches at the cull-substrate interface……..…70

5.3.2 Spatial anti-correlation of focal adhesions and HA patches…… ……..71

5.3.2.1 RCJ-P cells……..……..…...72

5.3.2.2 PC3 prostate cancer cells……..…….....74

5.3.2.3 Hs578T breast cancer cells……75

5.3.3 Topographical variation at the cell-interface decrease after hyaluronan removal……76

5.3.3.1 Topography of RCJ-P cell plasma membrane……..…....77

5.3.3.2 Topography of PC3 cells……80

5.3.4 HA matrix decreases the adhesion strength…….....80

5.3.4.1 Evaluation of cell area as a criterion to apply spinning disk……...82

5.3.4.2 Spinning disk results consistently show that interfacial HA weakens cell adhesion……85

5.4 Discussion……87
5.4.1 Assumption I: Focal adhesion strength does not significantly change in response to the HAdase treatment
5.4.1.1 FA area remains constant during and after HAdase treatment……90
5.4.1.2 Adhesion strength is not increased due to myosin II contractile activity……....92
5.4.1.3 Adhesion strength remains constant after enzyme treatment of cells not expressing HA....93
5.4.1.4 Signaling through HA cell surface receptors is under investigation……..…...94
5.4.2 Assumption II: HA can exert a repulsive force at the cell-substrate interface……...97
5.4.3 Assumption III: The HA force and adhesion force can be superimposed…….....100
5.4.4 Assumption IV: The non-specific adhesion energy between the cell and the substrate is minimal compared to the total adhesion energy……100
5.4.5 Full disclosure: other possible issues in approach and the analysis used to study HA-mediated cell adhesion
5.4.5.1 Drift of adhesion strength over time and issues with reproducibility……...….101
5.4.5.2 HAdase calibration not done quantitatively.102
5.4.5.3 PBS lacking ions impacts FA response…..103
5.4.5.4 Role of extracellular matrix proteins in hyaluronan mediated adhesion……....104
5.4.5.5 Cell shape and size control……..106
5.5 Conclusion and Outlook…….....107
6. CHONDROITIN SULFATE MEDIATED CELL ADHESION
6.1 Overview…… ….....109
6.2 Materials and Methods

6.2.1 Cell culture and sample preparation…… ……..111
6.2.2 Enzyme treatment…… …….111
6.2.3 Spinning disk adhesion assay…… …….111
6.2.4 Immunocytochemistry with antibody CS56…… 111
6.2.5 Fluorescently labeled histone……..112
6.3 Results
6.3.1 Cell adhesion strength increases after chondroitin sulfate enzymatic degradation……..…….112
6.3.2 Exogenous aggrecan does not alter cell adhesion strength…… ……...114
6.3.3 Efforts to confirm that bottlebrush CSPG exists at the cell-substrate interface……..…….115
6.3.3.1 Antibody labeling of CS with CS56……..…115
6.3.3.2 Electrostatic labeling with fluorescently-labeled positive proteins (histones)……..……...116
6.3.3.3 RICM shows topography not flatten after CS digestion……116
6.3.3.4 Indirect evidence: Aggrecanase……..….118
6.4 Discussion
6.4.1 CS effect on adhesion also shown in HAdase results….118
6.4.2 PCM composition differences between cell types shown in adhesion change…… ……...118
6.4.3 Possible source of interfacial CS on HA receptor ……119
6.5 Conclusion and Outlook…… ….....120
7. PCM Characterization on Migrating Cell
7.1 Overview…… ……....121
7.2 Wound healing assay to generate directional cell migration…… ..…122
7.3 Asymmetric PCM on migrating cells…… ..…123
7.4 Conclusion and Outlook…… ..…125
8. CONCLUSIONS AND OUTLOOK…… ….…126
REFERENCES…… ……..…..132

LIST OF TABLES

Table 3.1: Summary of physical measurements of the PCM on RCJ-P cells. 22

Table 3.2: Effective thickness of RCJ-P control cells shows varying pore size in the matrix. 27

Table 5.1: Summary of the measured adhesion strengths (and standard error) of HA-rich cells, RCJ-P and PC3, before and after enzymatic degradation of HA. 84

Table 5.2: Adhesion strength increase (% of control value) of various conditions for RCJ-P and PC3 cells. 88

Table 6.1: Adhesion strength percent change (comparing to control adhesion strength) of various enzyme treatment on RCJ-P and PC3 cells. 113

LIST OF FIGURES

Figure 1.1: PCM visualized as the exclusion region around the cell without particle presence. (a) Rat's chondrocyte cell, RCJ-P (b) Human prostate cancer cell, PC3 (c) Human breast cancer cell, MDA-MB-231 (d) Human breast cancer cell, Hs578T. Particles were fixed erythrocytes. 2

Figure 2.1: Pericellular matrix (PCM) is comprised of HA chains tethered to cell surface through surface proteins, HA synthases and HA receptors, decorated with proteoglycans. 8

Figure 2.2: 3D image of fluorescently labeled PCM shows it being the interface between cell and the surrounding. 9

Figure 2.3: Focal Adhesion organization. Used by permission from **MBInfo** www.mechanobio.info; Mechanobiology Institute, National University of Singapore. 11

Figure 3.1: Traditional PEA on (a) RCJ-P rat's chondrocyte, (b) human mesenchymal stem cell. Yellow line indicates the position where PCM thickness is measured. Scale bar is 10 μm. 21

Figure 3.2: GFPn and PEA show the extent of PCM around the same RCJ-P cell (a) GFPn before adding RBC for PEA (b) superimpose image of GFPn and bright field image after adding RBC (c) GFPn image after adding RBC. 23

Figure 3.3: RCJ-P visualized with (a) 100 nm size particles in red and (b) 2 μm size particles in cyan. The cells membrane is shown in white by WGA staining. 25

Figure 3.4: (a) Quantitative particle exclusion assay (qPEA) using monodisperse passivated beads ranging from 40 nm to 500 nm in diameter. (b) The effective thickness, d_{eff}, is measured to be distance from cell membrane to the position where bead intensity reach plateau (profile of 100 nm beads). This profile of the 100nm bead distribution is smoother than that in (a) because it is the average over 30 images taken of the same cell. The diffusing beads smooth out the variations. 26

Figure 3.5: (a) Schematic of the qPEA showing measurements of d_{eff} for different bead sizes. Experimentally only one bead size is added at a time. (b) The effective thickness associated with bead size increases until it plateaus at ~8.5 μm where 500 nm size beads and larger are excluded from the PCM completely. 27

Figure 3.6: Comparison between the correlation length profile calculated from the optical force probe assay (OFPA) and the quantitative particle exclusion assay (qPEA) data. 30

Figure 4.1: (a) Cross-sectional confocal image of pericellular matrix swollen with exogenous aggrecan on RCJ-P cell (c_{ACAN}=333 μg/mL, yellow=aggrecan, white=plasma membrane). The PCM extends in a three dimensional halo around the cell, with aggrecan intensity visible at distances more than 20 μm from cell surface. (b) Schematic of the PCM. Hyaluronan polymers (green) bind to the plasma membrane via HA-binding membrane proteins (blue). Bottlebrush proteoglycans (black) bind along the chain and stretch the HA into an extended configuration. (c) Erythrocyte particle exclusion assay shows the extent of the cell surface-grafted PCM on aggrecan-saturated mesenchymal stem cell (333 μg/mL for 2 hrs). (d) Erythrocyte particle exclusion assay shows the extent of the cell surface-grafted PCM on a native RCJ-P cell. 36

Figure 4.2: Treatment with chondroitinase-ABC (ChABC) at concentration of 0.27 unit/mL degrades the PCM in less than five minutes, as determined by erythrocyte PEA (a) before and (b) after treatment (5 mins later). The remaining gap between the erythrocytes and the cell surface is likely from the surface bound hyaluronan which is still decorated by the protein backbones of the ACAN. Cells are labeled with 1 μM calcein. 41

Figure 4.3: (a) PCM thickness measured perpendicular to the cell surface on human bone marrow derived mesenchymal stem cells (MSC) and rat chondrocytes (RCJ-P) versus exogenous aggrecan concentration. (b) Time-dependent swelling of the PCM after addition of aggrecan shows that reaching equilibrium extension requires one hour (c_{ACAN}=333 μg/mL). Data is an average for N=10 cells with 2 standard error reported. 43

Figure 4.4: (a) Fluorescently-labeled exogenous aggrecan at low concentration (39 μg/mL) swells the PCM. (b) Profiles of the aggrecan distribution versus distance to the cell surface at four concentrations. 46

Figure 4.5: The PCM is slightly perturbed by gentle exchange of the media. Measured using particle exclusion assays (PEA), we found that PCMs change less than 10% in width (increase or decrease). This is approximately the resolution of the erythrocyte PEA. This change may result from the loss of endogenous ACAN, whose binding is necessary for swollen PCM; or it could be due to loss of HA strands due to the perturbation, or some combination of the two processes. Given the small change in thickness, we surmise that most of the endo-ACAN is tightly bound to the HA by the reinforcement garnered by link protein. 47

Figure 4.6: Aggrecan co-localizes with hyaluronan in the cell coat. Cells were incubated with fluorescent aggrecan (333 μg/mL, 594 nm) for two hours, followed by incubation with GFPn (0.15 μM, 488 nm) for 10 minutes. (a) Fluorescent image of aggrecan distribution in the PCM. (b) Fluorescent image of HA labeled with GFPn. (c) Profiles of HA and ACAN taken perpendicular to the cell surface. 48

Figure 4.7: (a) Quantitative particle exclusion assay (qPEA) on RCJ-P cells using 100 nm fluorescent beads incubated for 2 hrs with 333 μg/mL aggrecan. The visible gradient in red intensity shows how the average local concentration of beads decreases towards the cell surface. (b) Typical profiles of nanoparticle distributions in RCJ-P cells swollen with 333 μg/mL aggrecan. 50

Figure 4.8: (a) Bacteria grown with samples of RCJ-P cells show slowed infection due to the PCM, which acts as a barrier. The size of the bacteria is larger than the threshold mesh size found for native RCJ-P cells using qPEAs (500 nm). (b) Mesh size versus distance to the cell surface: the mesh size decreases towards the surface. For swollen PCMs (c_{ACAN}=333 μg/mL), red curve, the porosity is reduced and it changes more slowly throughout the PCM. Maximum mesh size for native and exogenous aggrecan RCJ-P swollen coats: 500 nm, 300 nm. 51

Figure 4.9: (a) Optical tweezer measured equilibrium force in PCM on native and aggrecan-saturated RCJ-P cells (c_{ACAN}=333 μg/mL, 2 hrs). (b) Estimate of PCM porosity (mesh size) using polymer theory and equilibrium force measurement at four different aggrecan concentrations. The mesh size decreases with increasing aggrecan and becomes more uniform. All error bars are 2 standard errors. 53

Figure 4.10: Fluorescent BSA (66 kDa, AP-4510-60; SeraCare Life Sciences, Milford, MA) penetrates the PCM and reaches to the cell plasma membrane, which is fluorescently labeled by WGA. 54

Figure 4.11: Time dependent replacement of PCM bound fluorescent aggrecan with unlabeled aggrecan. (a) Fluorescent profiles of the aggrecan distribution versus time. The first curve marked ‘Before’ is taken after the fluorescent-aggrecan is removed and replaced with media (no aggrecan). Then the buffer is exchanged with a media containing the same concentration of aggrecan but with no fluorescent label (c_{ACAN}=333 μg/mL). (b) Integrated aggrecan intensity (over entire PCM) versus time. A reproducible drop occurs in the first step and then the aggrecan turnover proceeds linearly. (c) Monitoring aggrecan change at fixed positions in the PCM reveals that after the first time step, only locations 7.5 μm and closer to the cell continue to significantly change. 55

Figure 4.12: (a) Fluorescent histones (cyan) are barely detectable within the PCM of native RCJ-P cells (c_H=232 μg/mL for 20 mins). (b) The majority of histones bind very close to the surface and are largely injested by the cells. Labeling of the HA in the PCM with GFPn confirms as expected the PCM extends beyond the region where histones bind. (c) In aggrecan-enriched PCMs (c_{ACAN}=333 μg/mL), the histones bind strongly to the PCM, whose presence is confirmed by PEA (c_H=232 μg/mL for 20 mins). The PCM is thinner than histone-free measurements, indicating a collapse driven by crosslinking (see Figures 4.13, 4.14). (d) GFP and histones co-localize in the aggrecan-enriched PCM. 57

Figure 4.13: Histones bind to exogenous aggrecan in the cell coat of RCJ-P cells. Measurement of the fluorescently labeled aggrecan and histones shows co-localization of the molecules. (a) Fluorescent image of aggrecan-swollen PCM (333 μg/mL, 2 hours, yellow) with (b) histones added (232 μg/mL for one hour, light blue). (c) Profiles of exog-ACAN and histones in the PCM. The zero is arbitrary and does not indicate the cell surface. Histones were left in solution when taking image, hence the slightly higher background. The binding of the histones reduces the usually extensive PCM via histone-mediated crosslinking of the aggrecans. 58

Figure 4.14: Evidence for PCM crosslinking by histone proteins, whose multiple positive charges could simultaneously bind multiple aggrecan molecules, crosslinking the PCM. This leads to the formation of fibers and bundles around and between the cells. In both images, the samples where incubated with aggrecan (333 μg/mL) for two hours, followed by replacing with media containing fluorescent histones (232 μg/mL). 59

Figure 4.15: (a) Fluorescent histone treatment of aggrecan-incubated RCJ-P cells shows significant visible labeling of the PCM. (c_{ACAN}=333 μg/mL, 2 hours; c_H=232 μg/mL, 20 minutes) (b) The histones partially block digestion of the PCM by the enzyme ChABC (0.27 unit/mL) for at least 30 minutes. Without histones, the PCM is removed in less than five minutes. (c) Profile of the histone distribution perpendicular to the cell surface before and after ChABC treatment. There is a decrease in the histone intensity and slight degradation of the cross-linked fibers between the cells. 60

Figure 4.16: (a) Fluorescent histone treatment of RCJ-P cells does not show significant visible labeling of the PCM; however, the PCM remains, as shown by PEA. (232 μg/mL, 20 minutes) (b) Digestion of the PCM by the enzyme ChABC (0.27 unit/mL, 20 minutes) is blocked by the presence of the histones. (c) Profile of the histone distribution perpendicular to the cell surface before and after ChABC treatment. There is little change in the intensity. 60

Figure 5.1: (a) HA matrix under fixed RCJ-P (green). (b) Spatial anti-correlation between HA matrix (green) and vinculin FA (red) under fixed RCJ-P cells. 70

Figure 5.2: Live RCJ-P cells (a) GFP-paxillin shows elongated FA concentrated at edge of cell. (b) mCherry-paxiilin also label FA but not as clear as GFP-paxillin. 73

Figure 5.3: (a) GFP-paxillin on live PC3 cells shows FA more punctate than RCJ-P. (b) The vinculin antibody labels FA on fixed PC3 cells, also revealing showing punctate FAs (N>30). 74

Figure 5.4: Confocal image under live PC3 cells (a) GFPn labeling HA matrix. (b) GFPn labeling HA matrix (green) and mCherry paxillin showing FA (red). 75

Figure 5.5: mCherry-paxillin (red) and GFPn (green) shows spatial anti-correlation between FA and HA patches under cells. Imaged on live Hs578T breast cancer cell. 76

Figure 5.6: (a) RICM image on live RCJ-P cell and (b) GFP-paxillin labelling of the FA on the same cell. The dark patches in the RICM corresponds to the FAs. 77

Figure 5.7: RICM images of live RCJ-P cells showing the distance between cell and substrate (a) before and (b) after 20 minutes bovine HAdase treatment. 78

Figure 5.8: Pixel intensity histogram under single cell before and after bovine HAdase treatment show the cell's ventral topography flatten and distance shorten. 79

Figure 5.9: The average pixel intensity standard deviation before and after bovine HAdase treatment for 20 minutes. N=44 for RCJ-P and N=31 for PC3. 80

Figure 5.10: Histogram of projected cell area (a) control cells (CN), (b) after bovine HAdase (HV), and (c) after bacterial HAdase treatment (HC) of 15 minutes on RCJ-P cells. 82

Figure 5.11: PC3 cell area distribution showing it is suitable for spinning disk apparatus. 83

Figure 5.12: Comparison of adhesion strength of RCJ-P cells for control (CN), bovine HAdase (HV) and bacterial HAdase (HC) treatments. Left and middle are short time (15-30min) exposure, right is long time (2hr) exposure to HAdase. * $p<0.05$, ** $p<0.01$, *** $p<0.001$. 85

Figure 5.13: Comparison of adhesion strength of PC3 cells for control (CN), bovine HAdase (HV) and bacterial HAdase (HC) treatments (short and long term enzyme treatments); * $p<0.05$, ** $p<0.01$, *** $p<0.001$. 86

Figure 5.14: Simple mechanical interpretation of the increase of adhesion strength. Left (black box) is on control cells with HA matrix under cell and the right (purple box) is when HA matrix degraded. Red is the FA. Green arrow represents

the repulsive force from HA matrix. Blue arrow represents the extra hydrodynamic force required to break FA bonds. 89

Figure 5.15: FA size distribution of RCJ-P (a) before and (b) after bovine HAdase treatment. 90

Figure 5.16: Change in FA area after bovine HAdase treatment is small. 91

Figure 5.17: FA labeled by GFP-paxillin before (red) and after (green) bovine HAdase treatment on RCJ-P. The third column is the superposition of the two images. 92

Figure 5.18: Adhesion strength change on RCJ-P with blebbistatin treatments (BL) and after bacterial HAdase treatment of 30 minutes (HC). $p<0.01$. 93

Figure 5.19: Interfacial HA (a) before and (b) after oligo-HA treatment for two hours on RCJ-P cells. 95

Figure 5.20: Interfacial HA (a) before and (b) after oligo-HA treatment for two hours on PC3 cells. 96

Figure 5.21: HA labeled by GFPn under (a) 4-MU treated cells and (b) 2 hours after 4-MU washed off showing HA patches grown back under cells. Images are on the same RCJ-P cell using the same settings (which is why the figure on the right is saturated). 97

Figure 5.22: Adhesion strength change on RCJ-P with 4-MU treatment (4MU) and after HA growth (HA); $p<0.05$. 99

Figure 5.23: Adhesion strength of RCJ-P control cells drift over time. 101

Figure 5.24: Adhesion strength of PC3 control cells drift over time. 102

Figure 5.25: Adhesion strength of control and bovine HAdase treated cells RCJ-P in PBS (+/+) with divalent ions, and control cells in PBS (-/-) without ions; *** $p<0.001$. 103

Figure 5.26: Adhesion strength of RCJ-P on various surfaces; *** $p<0.001$. 105

Figure 5.27: Adhesion strength of RCJ-P cells decreased after bovine HAdase (HV) and bacterial HAdase (HC) treatments of 15 minutes on fibronectin coated surface; * p<0.05, ** p<0.01, *** p<0.001. 106

Figure 6.1: Histogram of projected cell area (a) before and (b) after ChABC treatment of 15 minutes on RCJ-P cells. 114

Figure 6.2: The average pixel intensity standard deviation before and after enzyme treatment for 20 minutes on RCJ-P cells. N=44 for HAdase and N=35 for ChABC. 117

Figure 7.1: (a) RCJ-P wound healing assay at 0 hours (b) RCJ-P wound healing assay at 24 hours. 123

Figure 7.2: GFPn labeled asymmetric HA on migrating RCJ-P, 3 μm above glass. Cell migrating towards lower right corner, as indicated with yellow arrow, showing more HA accumulation at the trailing edge of cell. 124

Figure 7.3: (a) GFPn labeled asymmetric HA on migrating RCJ-P cell, 3 μm above glass. Cell migrating towards lower right corner, as indicated with yellow arrow. (b) GFPn labeled HA under the same migrating cell showing more gaps between HA patches at the leading edge of cell. 125

LIST OF SYMBOLS AND ABBREVIATIONS

PCM	pericellular matrix
HA	hyaluronan
HAS	hyaluronan synthase
ECM	extracellular matrix
GAG	glycosaminoglycan
PEA	Particle exclusion assay
RBC	red blood cell
qPEA	quantitative particle exclusion assay
OT	optical trap
OFPA	optical force probe assay
RCJ-P	rat chondrocyte joint cells
PC3	human prostate cancer cells
MDA-MB-231	human breast cancer cells
Hs578T	human breast cancer cells
d_{eff}	effective thickness
GFPn	green fluorescent protein-neurocan link protein
MSC	mesenchymal stem cells
CS	chondroitin sulfate
CSPG	chondroitin sulfate proteoglycan
HAdase	hyaluronidase
ChABC	chondroitinase ABC
RICM	reflection interference contrast microscopy
CN	control cells
HV	bovine hyaluronidase
HC	bacterial hyaluronidase
4-MU	4-methylumbelliferone
FA	focal adhesion

SUMMARY

Pericellular matrix (PCM) is a hyaluronan rich polymer matrix anchored to the outer cell membrane surface. Negatively charged bottlebrush proteoglycans also play an important role in the matrix giving it its structure. In the past decade, it has been increasingly appreciated that this often microns-thick cell coat is involved in regulating a range of key physiological processes, including proliferation, migration, synaptogenesis, and wound healing. How the PCM impacts these processes is not well understood, but it is likely in part via physical and/or physiochemical processes, resulting from the bulky size and high negative charge of hyaluronan and its associated proteoglycans. This thesis work introduces new methods to quantify and probe the physical function of the PCM, and addresses two fundamental biophysical questions (i) how the PCM impacts transport of objects to the surface and (ii) whether surface-associated hyaluronan matrix mechanically regulates cell adhesion.

A detailed picture of the *in vitro* PCM microstructure and its impact on the transport of molecules and particles to the cell surface is reported for the first time. The work shows that particles 40 nm and larger are significantly impacted by the PCM, which acts to filter and reduce the number reaching the surface in a size-dependent fashion – a consequence of the decreasing pore size of the PCM towards the cell surface. Molecular accessibility to the cell is less impacted unless the species is positively charged, in which case studies show that it sequesters strongly within the PCM, binding to the negatively-charged bottlebrush proteoglycans. Studies with exogenous proteoglycans demonstrate opportunities to modify the thickness and pore size of the sieve-like PCM. Addition of proteoglycan into the matrix extends the matrix's thickness and decreases its pore size. Different concentrations of exogenous proteoglycan provide the ability to tune the matrix reach and tightness.

Mechanical quantification of cell adhesion strength versus hyaluronan patches at the cell interface reveals that PCM reduces adhesion to substrates in several cell types. Complementary

studies with interferometric microscopy reveal that HA increases the roughness of the cell interface at the substrate, reducing contact, potentially weakening adhesion. The outcome of these detailed studies strongly imply that the role of cell-surface associated hyaluronan *in vivo* deserves much more attention than previously garnered. The PCM acts as a gatekeeper in modifying what reaches and adheres to the cell surface – two processes fundamental in the regulation of multicellular organisms.

CHAPTER 1

Introduction

The negatively charged polysaccharide hyaluronan (HA) is found throughout the natural world, including in vertebrates, algae, mollusks (1) and a subset of microbes. HA is ubiquitous in vertebrates playing various roles in many different tissues ranging from the brain to joints to the eye to connective tissue. Three transmembrane proteins called hyaluronan synthases (HAS: HAS1, HAS2, HAS3) are responsible for synthesizing and extruding HA through the plasma membrane in vertebrates. The size of the HA depends on the synthase, where HAS2 produces the highest molecular mass products. Studies have demonstrated that HA is required for normal development and has several therapeutic functions (2–6). For example, in embryonic morphogenesis, deletion of HAS2 in mouse embryos abrogates cardiac morphogenesis and causes the embryo to die during mid-gestation (7, 8). Furthermore, HA expression is correlated with fundamental processes as broad cell proliferation and migration, synaptogenesis, inflammation, cancer metastasis, and wound healing.

Hyaluronan in vertebrates can be found in three different contexts: bodily fluids (synovial fluid (9, 10), vitreous humor (11)), extracellular matrix (ECM)(12, 13), and pericellular matrix (PCM) (14). The focus of this thesis is the pericellular matrix (PCM), a robust polymer matrix that is grafted on the membrane of many cells (see Figure 1). The main components of this extended, often microns-thick cell coat are the polymer hyaluronan (HA), hyaluronan-binding bottlebrush-shaped chondroitin sulfate proteoglycans (CSPG), e.g. versican or aggrecan, and HA surface receptors, such as CD44 (2). The PCM's components are ubiquitous, and its appearance in diverse biological contexts, suggest that there is no single defining function for the PCM, but rather it is involved in a wide range of process that are important to the function of single cells and

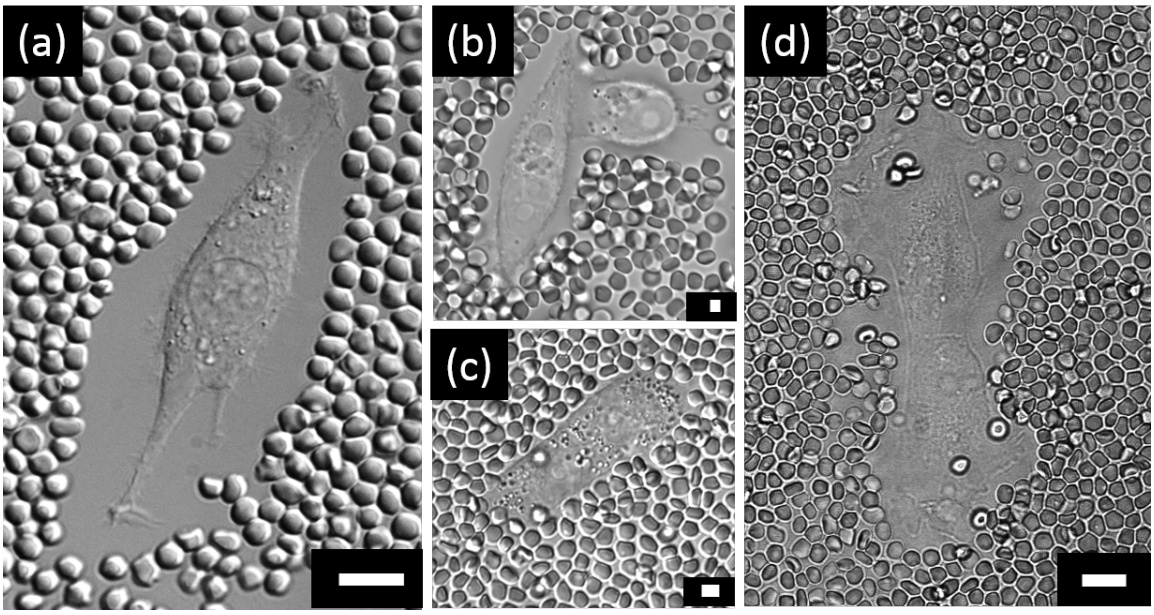

Figure 1.1: PCM visualized as the exclusion region around the cell without particle presence. (a) Rat's chondrocyte cell, RCJ-P (b) Human prostate cancer cell, PC3 (c) Human breast cancer cell, MDA-MB-231 (d) Human breast cancer cell, Hs578T. Particles were fixed erythrocytes.

tissues. Previous work has shown that it is involved in fundamental biophysical processes such as cell adhesion, migration, and proliferation (3-6). The role of the PCM in human health remains to be fully explored but there is mounting evidence to suggest that it is involved in the onset and progression of cancer (7, 8), wound healing (9), and infertility (10).

The role of surface bound hyaluronan (PCM) is generally not well understood, yet it is abundant in the body. The fact that the PCM is fundamentally a cell-regulated interface between the cell and its exterior, positions the cell coat to play a gatekeeper role in negotiating the integration of cells into tissues as well as what passes to and from the cell surface. The magnitude and importance of PCM function is unclear, but by its very nature and presence, it is logical that the HA-bottlebrush proteoglycan matrix must play an integrative role with other surface adhesion receptors that regulate cell adhesion to ECM or other cells. The most telling and extreme version

of this, already verified, is synaptogenesis, where a PCM comprised of hyaluronan and neurocan suppresses formation of new synapses and stabilizes established synapses (15).

Historically the role of PCM has been neglected or underappreciated for several reasons. The first is that its extreme high hydration makes it impossible to see in bright field microscopy and fixation procedures destroy the extended matrix. Therefore, until recently the tools to characterize the PCM were crude and limited. Many researchers were not even aware that such a construct might extend at least a few hundred nanometers if not microns from cell surfaces in their *in vitro* cell culture. Second, any topic that involves glycobiology has generally been considered difficult and few researchers were involved (16, 17). And finally, even for those researchers interested in and studying PCM, limited biophysical tools existed to probe and investigate the mechanisms behind PCM biology. A consequence of the state of the field is that there are numerous very interesting questions to be pursued if one can provide a few tools to characterize both the PCM and the underlying biology.

This thesis represents one of the first systematic efforts to date to probe the microstructure and mechanics of the PCM. In particular, our efforts in the lab throughout the duration of this thesis have been primarily focused on characterizing the physical impact of PCM on the two most obvious possible processes that the cell coat might have: (i) passage of objects to and from the surface and (ii) the mechanics of cell adhesion.

The remaining of this thesis will be presented in seven chapters. Chapter 2 will provide additional background and context, in particular providing an overview of the literature regarding what is known about the correlation of hyaluronan expression with cell adhesion-dependent processes. In chapter 3, I present a novel approach to quantify the spatial varying pore size of the pericellular matrix and provide a deeper understanding of the PCM structure. Chapter 4 introduces various biophysical techniques and demonstrates the ability to tune the accessibility of cell surfaces through the bottlebrush proteoglycan in the PCM. Chapter 5 shows that adhesion

strength, the force required to detach cells from the substrate, changes with various HA conditions and provides evidence of the mechanical impact of the matrix on focal adhesions and the overall adhesions state of a cell. Chapter 6 expands the adhesion results to another possibility, chondroitin sulfate (CS) mediated adhesion. Chapter 7 summarizes our nascent but promising efforts to characterize the HA matrix during cell migration. Finally, chapter 8 concludes with summary of the results, and presents an outlook of the exciting questions and directions that can be pursued by building on the techniques and insights achieved in this body of work.

CHAPTER 2

Background Information

2.1 Hyaluronan (HA)

HA is a long linear polysaccharide consisting of a repeating disaccharide unit. The disaccharide in HA is composed of D-glucuronic acid (GlcUA) and D-N-acetylglucosamine (GlcNAc). Each disaccharide is about 1 nm long and 0.5 nm wide (18). The carboxyl group on the monomer makes HA a negatively charged at physiological pH (13, 19). HA is synthesized at plasma membrane by hyaluronan synthase (HAS) and mostly exists in extracellular regions. HA is among the largest polysaccharides in nature. HA molecules can have up to 25, 000 disaccharide residues, corresponding to 9.5 MDa in molecular weight and 25 μm in length. Measured in 0.15M NaCl at 37 ˚C using multi-angle light scattering, the radius of gyration R_g of HA of molecular weight ranging from 40 kDa to 5.5 MDa are about 15 nm to 286 nm, and persistence length of HA is estimated to be 7.5 nm (20). HA behaves as a stiffened random coil and exhibits non-Newtonian rheology properties which are heavily influenced by both HA concentration and length (21). Partially due to the length-dependent rheological properties, the biological functions of HA are strongly depending upon its length (22). Long HA polymers are space filling, anti-angiogenic, and immunosuppressive and that regulate differentiation, possibly by suppressing cell-cell interactions; medium length hyaluronan chain are involved in ovulation, embryogenesis, and wound repair; short HA fragments are inflammatory (23), immune-stimulatory, and angiogenic; HA oligomers made of a few disaccharide residues are antiapoptotic and inducers of heat shock proteins (24). With its broad biological functions, HA is used in an increasing number of applications including osteoarthritis, wound healing, ophthalmic surgery, adhesive prevention, drug delivery.

2.2 HA binding proteins

Inside the extracellular matrix (ECM) there are abundant of glycosaminoglycan (GAG), which are long unbranched polysaccharides consisting of a repeating disaccharide unit. They do not normally occur as free chains *in vivo*. They usually form proteoglycans, which are the GAG chains linked to a protein (25). There are different types of proteoglycans depending on the different GAG chains and protein combinations. A specific group of proteoglycans consisting of a protein core and chondroitin sulfate side chains are therefore known as chondroitin sulfate proteoglycan (CSPG). They are known to be structural components of various human tissues, including cartilage and involved in certain cell physiological processes, such as cell migration, cell growth and interaction with other ECM constituents (26). When the hydrophilic GAG chains covalently bound and arranged onto the protein backbones to form a bottlebrush shape, they are identified as bottlebrush CSPGs, also known as lecticans or hyalectans. Four members are in the lectican family: aggrecan is a major component in cartilage (27); versican is widely expressed in connective tissues including vascular smooth muscle, skin epithelial cells and the cells of central and peripheral nervous system (28); neurocan and brevican are largely restricted to neural tissues (29). All hyalectins contain a common HA-binding domain (G1) that allows them to aggregate densely along HA, nearly permanently when reinforced by an additional protein called link protein (30). The key physical characteristics of the bottlebrush proteoglycans stem from a second domain (G2) that contains a dense region of highly-sulfated glycosaminoglycans (GAGs). The third and last domain (G3) is smaller and consists of specific binding sites for various biomolecules. They also have been shown to interact with a variety of other matrix components including laminin, fibronectin (31, 32), collagen (33, 34), and other bioactive molecules such as growth factor and cytokine (35).

2.3 Pericellular Matrix

Pericellular matrix (PCM) is a polymer matrix end-grafted on cells' surface, and it's sometimes referred to the cell coat or pericellular coat. The PCM is comprised of hyaluronan (HA) and bottlebrush proteoglycans (PGs) whose side chains consist primarily of the highly-negatively charged chondroitin sulfate. Strands of high molecular weight, linear HA are anchored to the cell surface by HA synthase and HA receptors (*e.g.* CD44, RHAMM). The HA-binding bottlebrush PGs then assemble along the HA strands. These PCM components localize in micron-sized pockets under the cell, and remain distinctly spatially segregated from, but in coexistence with focal adhesions (36–39). The PCM has received minimal attention in the context of classic integrin regulated cell adhesion (39); yet many studies point to HA-rich PCM as playing a key role in mediating cell adhesion-dependent processes including embryogenesis, migration, proliferation, synaptogenesis, wound healing, and cancer (14).

Both *in vitro* and *in vivo*, the PCM can also decorate the rest of the cell surface, embedding the cell in a halo of highly-hydrated supermolecular assemblies of HA and PGs, forming a hierarchical forest of bottlebrushes (Figure 2.1) (30). The swollen highly-negatively charged matrix repels objects away from the cell surface, demonstrating how the same components might exert forces on the substratum, resisting contact and adhesion to the surface by integrin-ECM interactions. Indeed, this repulsive effect is the basis of the so-called particle exclusion assay (PEA), the most common method used to determine whether a cell is enveloped by a sugary polymer coat (40). It is an indirect way to visualize the PCM where fixed red blood cells are added around the cells. The red blood cells are excluded from penetrating the area occupied by the matrix, and this exclusion region is the representation of the PCM's physical extent (41–46). Like its ability to repel particles from reaching the cell surface, a plethora of direct and indirect data suggests that the PCM plays a similar role at the interface between the cell and the substratum

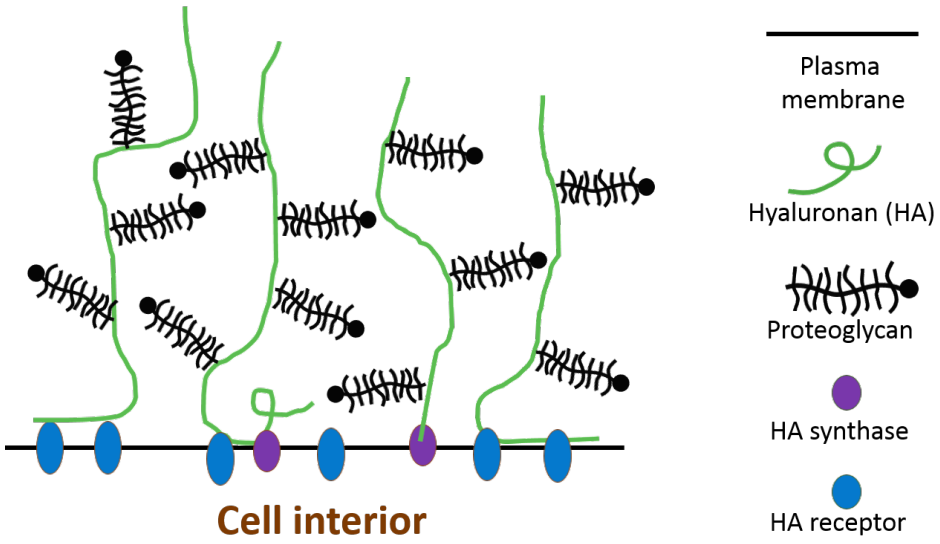

Figure 2.1: Pericellular matrix (PCM) is comprised of HA chains tethered to cell surface through surface proteins, HA synthases and HA receptors, decorated with proteoglycans.

or other cells. It appears that the PCM likely plays a dual role, regulating a delicate balance of weak attachment and strong repulsion, interfering with the ability/kinetics of integrin-ECM binding.

2.4 Pericellular matrix functions

The mechanism of PCM in the diverse functions are poorly defined but researches have shown evidences of the matrix impacts a wide range of diverse fundamental cell processes and disease states. The viscoelastic nature, makes the PCM play an important role in tissue homeostasis and biomechanical integrity, and a good mechanic protector inside cartilages to decrease the friction in the join (47). The PCM stands between the cell and its surrounding, so exogenous molecules pass through the matrix to gain access to the cells, hence it acts as a gatekeeper and is important in drug delivery (48) or localization and concentration of molecules, such as growth factor (35, 49) (Figure 2.2).

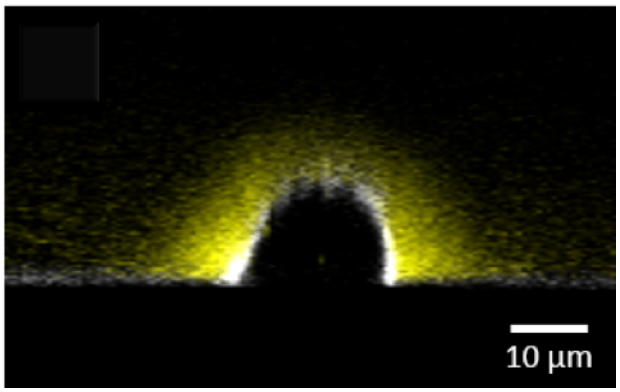

Figure 2.2: 3D image of fluorescently labeled PCM shows it being the interface between cell and the surrounding.

PCM and its components have been shown to have anti-adhesive properties and affect many adhesion-based physiological processes. For example, inside PCM, the interaction between HA and cell surface receptor increases the rate of cell proliferation (50) and migration (51, 52). The matrix is thus found to be important in wound healing (6, 53). The anti-adhesive property of PCM is also prominent in other area as well. The lecticans in the PCM regulate the synaptogenesis that removal of the PCM enhances the synaptic puncta (15). At the same time, HA macromolecules are essential for embryonic development, and lacking HA causes severe cardiac and vascular abnormalities which leads to the eventual death of the embryos (7, 54).

Because of the high synthesis rate, PCM can also be used as marker for some diseases, *e.g.* osteoarthritis (55) and in various forms of cancer invasion. Many studies demonstrated PCM and its components, *e.g.* HA, lecticans and surface receptors, promote metastatic abilities of malignant cells (56–58). However, an special case on the naked mole rats showing the cancer resistant ability of this peculiar rodent came from the presence of HA, while downregulation of HA expression in the rats increase the cells' susceptibility to cancer (59). It is also speculated that PCM facilitates cell mechanotransduction (60, 61).

2.5 Particle Transport through PCM

PCM interacts with particles around the cells and affect their accessibility to the cell surface. PCM has been known for its ability to exclude large particles. As mentioned before, researchers have been relying on this characteristic of the PCM to visualize and study this invisible layer on the cell with the technique Particle Exclusion Assay (Figure 1.1) (41–46). It was hypothesized that the complex structure of the PCM affects particles differently by size, *e.g.* 70 nm dextran reaches about half a micron distance to the cell surface while the fixed erythrocytes, about 3 μm in size, are stopped several microns away from the surface (62). Even smaller molecules seem to be allowed through the matrix and gain access to the cells because the nutrition molecules can reach the cell and maintain cell viability. Those smaller molecules are not blocked by their sizes, but the HA matrix around cells still change how they diffuse through the matrix by electrostatic interactions (63). The electrostatic filtering prevents a portion of the particles reaching the surface, but for the ones reached the surface, research shows that PCM is helping the retention rate of the particles around the cells and enhance the intake (64). Our further studies of PCM's impact on cell surface accessibility by particles/molecules are documented in Chapter 3 and 4.

2.6 PCM *in vivo* vs *in vitro*

Many of the experiments done on the PCM, including ours, are performed in vitro. Granted, the conditions of the PCM are different when it is around single cells cultured from a cell line than in the natural tissue environment. But there is still so much about the mechanism of the PCM we don't know that the variable base is too large for in vivo studies to elucidate the detail mechanisms of the PCM effects on the cell. The in vitro studies are the beginning steps toward a more

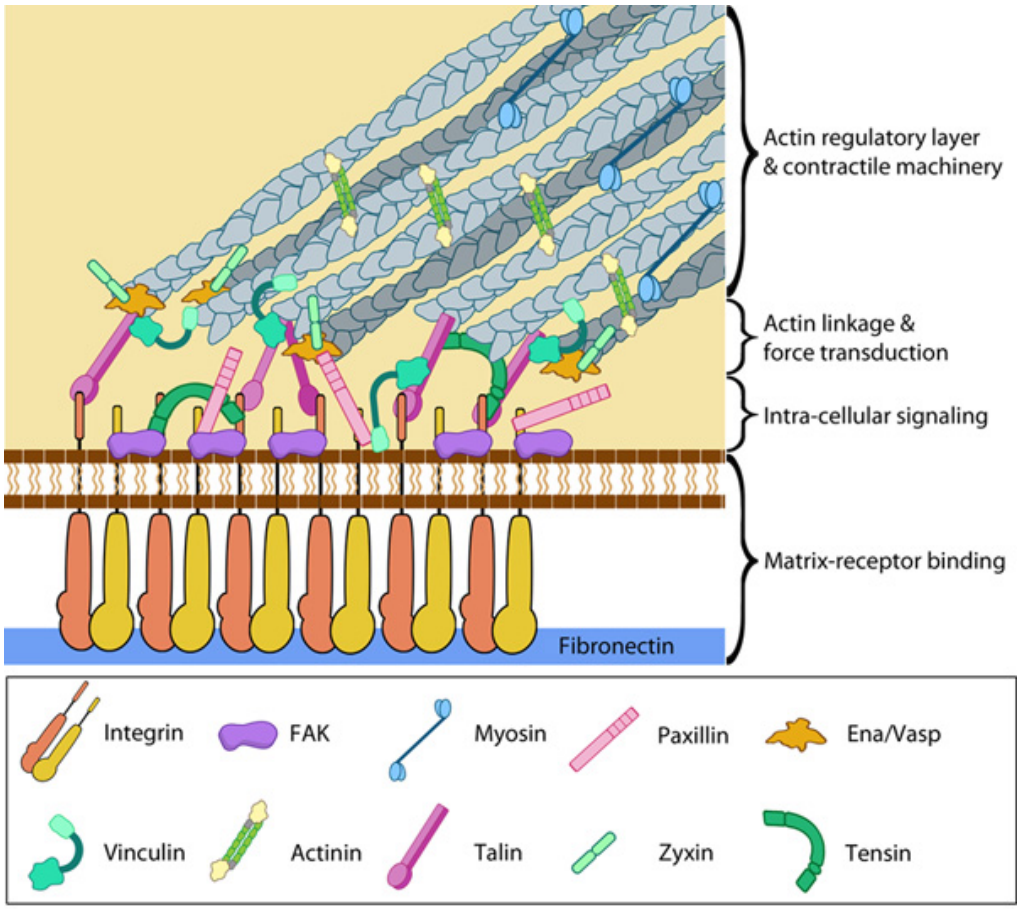

Figure 2.3: Focal Adhesion organization. Used by permission from **MBInfo** www.mechanobio.info; Mechanobiology Institute, National University of Singapore.

comprehensive in vivo study in the future. The mechanism and lessons learned in these in vitro studies will then be applied to the analysis of the future in vivo studies.

2.7 Focal adhesions

During cell adhesion, focal adhesions (FA) are formed to connect intracellular actin bundles to the extracellular matrix (Figure 2.3). The FA contains integrin and a wide variety of proteins that aggregate to the site (65). There are more than 100 different proteins at the FA, which suggests a considerable functional diversity (66). FA not only anchor the cell, it function as signal

carrier/sensor, which inform the cell about the condition of the surrounding ECM and affect the cell behaviors (67). FA is highly dynamic that grow or shrink due to the turnover of its component proteins in response to changing mechanical stresses (68–71). At the interface, the transmembrane integrin binds to ligands on the substrate via short amino acid sequences, such as RGD that could be found in proteins such as fibronectin. It can attache to actin filaments inside the cell, and after traction force exerted by actomyosin contractions produces signal transduction events such as focal adhesion kinase (FAK) phosphorylation, so more adhesion proteins, such as talin, filamin, vinculin and tensin, are recruited to the FA and promote adhesion maturation. For the immobile cells, their FAs are stable. But during migration, the FAs undergo constant assembly and disassembly process.

The dynamic assembly and disassembly of the FA plays a crucial role in cell migration. When the FA first form at the edge of the cell, integrin and some of the adapter proteins, *e.g.* talin, paxillin and tensin, are co-localized. Some of the nascent FA failed to mature and disassembled but some grew larger into a mature and stable FA by recruiting more protein, such as zyxin (72). After mature FA formed at the leading edge of a migrating cell, it become stable and the actin retrograde flow, which is the polymerization of the actin filaments at the leading edge and flow back towards the cell body, drive the cell forward (73). The matured FA stay under the cell until it reaches the trailing end of the cell edge. The FA then go through an unknown process to start disassemble and recycles the integrin and other proteins (74). Huttenlocher *et al* suggests it is regulated by calcium-dependent protease calpain, whose inhibition has been shown to inhibition of FA-ECM separation (75). In this work, we are providing another possibility.

Although HA expression at the cell interface and its presence in PCM are correlated with many processes that involve change in adhesion state (migration, proliferation, synaptogenesis, contact inhibition and the numerous activities that involve cell migration and proliferation including wound healing, cancer metastasis and embryogenesis), few studies systematically look at how the focal

adhesion machinery and hyaluronan function together and whether their apparently dual roles as an adhesive and repulsive mechanism are orchestrated in a meaningful way that impacts cell mechanics. Below we review much of what has been reported to date. The rest of this thesis, especially chapters 5, 6, and 7 are focused on providing more data and insight regarding the relationship between integrin-mediated adhesion and hyaluronan expression.

2.8 Focal Adhesion and Hyaluronan

Many studies have been done to relate HA to cell adhesion-related processes. Accumulation of HA has been shown to inhibit cell contact (76–78), increase cell migration and proliferation rate (3, 79), promotes malignant cancer phenotypes (80–82) and is important during embryogenesis (8). HA is added for better wound healing in surgery for its migration and proliferation enhancement ability (6, 83). Some studies also shown that HA plays an important role in early adhesion events (65, 84). But the mechanism of HA's regulation on focal adhesion is still unknown. Some researchers have suggested that HA and HA receptors create a rapid and transient protein tyrosine kinase signaling event to change adhesion (85). HA also has been shown to activate protein kinase signaling to modify focal adhesion also through its receptor (86). Only a handful of studies investigates the direct impact of the HA on the focal adhesion. Twarock et al showed degradation or displacing HA on cell increases the cleavage of FA and destabilize it (87). And a recent 2014 study demonstrated that HA matrix, or bulky glycocalyx, exerts force on the adhesion receptors, aggregate the integrin cluster, and regulate the adhesion assembly (88). We are aiming to take another route than those. Instead of the stability of FA, we want to study the force HA can pose on FA that directly alter the adhesion event.

2.9 FA Area and Traction Force

In Chapter 5 & 6, we discuss how the PCM affects the adhesion strength of cells, which is how much force is needed to detach the cells from substratum. In order to test our hypothesis of PCM exerting repulsive force between cell and substrate and thus decreasing the adhesion strength, we use enzyme to change the PCM condition and monitor the change in cell adhesion strength. However, to find the effect of PCM change on adhesion, our assumption is that the strength of the integrin-ligand binding strength remain after enzyme treatment.

FA composition changes in different stages of maturation. Their shape and size altered as well; they change from a circular, submicron dot to an elongated plaque with a 0.5-1 μm width and lengths up to several micrometers through maturation (89). FA size change might come from internal cytoskeleton contraction or external force (90). And many studies found direct correlation between FA size and local traction force (67, 91, 92). However, there are studies showing a complex relationship between the FA size and the force it exerts. There's one study shows an inverse correlation between the size and traction stress at the front of the migrating cell but finds no such relationship at the rear end. It has been shown that extremely large super mature FAs exerts a high stress (91), while the small FAs ~1 μm exhibit a widely variable stress (92). Striker, et al in a 2011 publication demonstrates elegantly that the size dependency of the traction force only occurs at the initial stages of myosin-mediated adhesion maturation and growth, and for mature FA, no correlation was observed (93). Hence, when monitoring the FA strength, only measuring the FA size is not enough, so other measurements are made to compliment it to test our hypothesis in chapter 5.

Chapter 3

Organization and Microstructure of the Pericellular Matrix

3.1 Overview

The functions of the PCM are not well defined but studies show that the matrix influences a wide range of fundamental cell processes and disease states including cell adhesion, proliferation (50), motility/ migration (51, 52), synaptogenesis (15), embryonic development (7, 54), mechanotransduction (60, 61), protection from viral infections (94), morphogenesis, mechanical protection (47), drug delivery (48), wound healing (6, 53), sequestration of growth factor, osteoarthritis (55) and various forms of cancer invasion (57, 58, 95).

Improved characterization methods are needed to clarify the mechanisms by which the PCM contributes to these cellular functions. Until very recently, the tools to characterize pericellular matrix were limited and crude. As a result, the fact that an extended polymer coat is present on many cell surfaces *in vitro* and *in vivo* has been neglected, and possibly underappreciated. Part of the difficulty in studying the PCM is that it is not visible in traditional bright field microscopy. Due to its hydration, the PCM has similar index of refraction as the surrounding fluid, and it appears as if nothing is there. For the small number of researchers interested in studying PCM, the most convenient and common method used to visualize is the crude particle exclusion assay (PEA) (40), introduced in Chapter 2. Others have tried to fluorescently label the hyaluronan or the lecticans but accurate characterization was thwarted by the destruction of the PCM structure by fixation procedures. Only recently have fluorescent labels for HA become available that could be used on living cells (96). This has transformed the ability to study PCM during the many physiological events described above. To study the biophysical and physiochemical roles of the PCM, our lab has made it a mission to expand the tools to characterize the cell coat. This chapter (and chapter 4 and 7) detail the latest assays that we have

established to go beyond the traditional schematic of PCM organization (Figure 2.1) and the surprising but not very informative images made with particle exclusion assays.

This chapter summarizes our development of a new technique and the information it provides during PCM characterization. We call the approach the quantitative particle exclusion assay (qPEA) (97, 98), because the basic idea is to examine how the PCM interacts with nanoparticles of different sizes. The method yields information regarding the microstructure of the PCM as well as the accessibility of the cell surface to nano-objects when the PCM is a barrier. Insight into the openings and porosity of the PCM is novel information; further, insight into how nanoparticles, exosomes and even molecules diffuse through the PCM is critical both for envisioning how PCM regulates cell-cell interaction in the body as well as for in vitro studies of classic topics ranging as far as drug delivery, phagocytosis to the new exciting area of exosome biology.

3.2 Material and Methods

3.2.1 Cell culture and sample preparation

Rat chondrocyte joint cells (RCJ-P, fetal calvaria, batch 15.01.98; Prochon Biotech, Rehovot, Israel) are cultured under 37°C, 5% CO_2 with α-MEM, 15% FBS, 2% L-glutamine (Mediatech, Manassas, VA). Human prostate cancer cells (PC3, ATCC: CRL-1435) are cultured under 37°C, 5% CO_2 with ATCC-formulated F-12K Medium (ATCC: 30-2004) with 10% FBS. The cells are plated for 18-20 hours at low density on 78.5 mm^2 ($5x10^4$ cells for RCJ-P and 30k for PC3), and measured during passages 15-40. Mesenchymal stem cells (MSC, human bone marrow-derived, Texas A&M, College Station, TX) are cultured at 37°C, 5% CO_2 with α-MEM, 16.5% FBS, 2 mM L-glutamine, 100 U/mL penicillin and 100 µg/mL streptomycin. Human breast cancer cells (MDA-MB-231, ATCC: HTB-26) are cultured under 37°C, 5% CO_2 in DMEM with 4.5 g/L glucose (Cellgro: 15-013-CV) and 10% FBS. Human breast cancer cells (Hs 578T, ATCC: HTB-126) are

cultured under 37°C, 5% CO_2 in DMEM with 2.2 g/L sodium bicarbonate (ATCC 30-2002), 10% FBS, and 0.1% bovine insulin (Sigma: I0516). Chinese hamster overy cells (CHO-K1, ATCC: CCL-61) are cultured under 37°C, 5% CO_2 with F-12K (Cellgro: 10-025CV) and 10% FBS.

Fluorescent imaging is held at 37°C and 5% CO_2 with a stage-top incubator (N. E-MSI 07-3156, Okolab, Ottaviano, NA, Italy). During RICM, a different stage-top microscope incubator (LiveCellTM, Pathology Devices, Inc., Westminster MD) maintained the cells at 37°C, 5% CO_2, 80% humidity in order to keep the cells viable for long-term experiments.

The sample holder used for experimentation is made of nonstick Teflon and has a small well in the bottom that is covered with a 25x25 mm #1.5 glass coverslip (VWR: 48366-249). RCJ-P was seeded on cleaned glass coverslip directly while PC3's coverslip was coated with collagen and Hs578T's coverslip was coated with fibronectin. Method of coating coverslip is described below. To minimize volumes used, the typical well can hold a volume of 200 µl. After assembly the sample holders are exposed to a UV light on each side in order to insure sterility.

3.2.2 Particle exclusion assay (PEA)

Traditional PEA: fixed sheep erythrocytes (R3378; Sigma Aldrich, St. Louis, MO), are suspended in PBS and then added to the sample with a final concentration of 1 mg/mL to achieve mono-layer after 10 mins. Thickness of the PCM is measured to be the perpendicular distance from the cell plasma membrane (at the flattest location on the cell, usually the middle) to the nearest erythrocyte.

Quantitative PEA (qPEA): fluorescent polystyrene spheres (FluoSpheres; Invitrogen) of different sizes are passivated before use in qPEA. For passivation, larger particles (>200 nm) are reversibly swollen with toluene to enable physical entanglement of Pluronic F127 as previously described (99). Smaller particles are covalently modified with methoxypolyergylene glycol amine

(Fluka, St. Louis, MO) (100). For qPEA, 22 µL of the microspheres (5% solid) are added to 178 µL media and allowed to settle for 10 min. The properties of passivated nanoparticles are assumed to be the same with different passivation methods but there might be differences. To facilitate image analysis, the cell surface is fluorescently labeled with wheat germ agglutinin (WGA-Alexa Fluor 633 conjugate; Sigma), which is added to the sample (125 µg/mL) 5 mins before measurements are obtained. Location of the membrane is determined to be the highest fluorescent intensity. The samples are imaged with a confocal microscope (FV1000; Olympus, Tokyo, Japan). Microsphere distribution is measured by taking the fluorescence intensity perpendicular to the cell surface at 3 µm above the glass surface and averaged over 2 µm. The effective thickness, d_{eff}, is identified to be the distance between cell surface and the plateau in the average bead intensity.

The presence of the microspheres inside cell culture media was limited to the experimental time of two hours in order to minimize the effect on cell health and behavior.

3.2.3 Hyaluronan labeling: GFPn production and use

Rauch et al. (96) designed a cDNA strand that encodes for a protein where a green fluorescent protein (GFP) molecule is connected to a neurocan link protein (96, 101). Neurocan is a proteoglycan similar to the aggrecan in our system, which has a similar structure where the first domain of the backbone is the link that binds specifically to hyaluronan. The resulting protein (called here GFPn) specifically labels hyaluronan with GFP, resulting in the ability to fluorescently image the cell coat. This plasmid is transected into HEK cells in order to produce the GFPn molecule. HEK cells were gifted by U. Rauch (Uppsala University, Uppsala, Sweden), and are cultured with a 1:1 mixed D-MEM/F12 (Mediatech), 10% FBS, 1% L-glutamine (Mediatech) and 0.01% puromycin solution (10mg/ml, Sigma). Puromycin is added after the first passage, as

puromycin can be toxic to recently thawed cells. After transfection, the HEK cells translate the cDNA into the GFPn molecule via the typical protein production cell machinery, and the GFPn is then released into the cell media. For GFPn production, the transfected HEK cells are plated into five 175 cm^2 flasks and allowed to reach confluency (~ 4 days). The media is then removed and replaced with FBS free media. Every 2 days the media is collected and replaced again with FBS free media. The collected media is a solution of media, dead cells, and molecules excreted by the cells, including the desired GFPn. The collected media is centrifuged at 2000 rpm for 20 minutes in order to separate the dead cells and large debris from the media. The supernatant is then collected and treated with protease inhibitor (Thermo Scientific). This procedure is repeated for 2-3 collections, as after this point the cells no longer produce measurable GFPn. If more GFPn is required, another set of 5 flasks must be plated and the process restarted.

After the desired quantity of collected media is taken, it is then centrifuge filtered (Millipore Amicon Ultra: 15-30 k), which collects any molecules larger than 15-30 kDA and lets those smaller pass through the filter. After initial filtration, typically 20% of the total initial volume remains. The remaining media (which contained the GFPn molecule) is then filtered again, this time with a his-tagged protein purification column (Pierce, HisPur Cobalt). In short, these columns have a resin that has a high affinity for his-tagged proteins, which is included in the design of the GFPn. The remaining media is filtered through this column 400 µl at a time. Any non his-tagged proteins and media easily pass through the resin and column, leaving only the GFPn remaining. The column is then eluted with a buffer (as directed by the product sheet), which released the GFPn from the resin, and is collected with a 200 µl volume of elution buffer. Releasing the GFPn with the elution buffer is performed three times as the first pass is not 100% efficient, resulting in three collections. The fluorescence signal of the GFPn solution is then checked with a UV Vis machine to verify collection and to quantify the amount of protein.

In order for cell treatment, the GFPn solution is then run through a buffer exchange column (Thermo Zeba desalting) in order to suspend the GFPn in PBS. The elution buffer, while required

for releasing the GFPn from the resin column, is not the correct pH or salt density for cell treatment. The buffer exchange protocol requires the desired buffer to be run through a column multiple times, followed by a run with the GFPn media. This results in a GFPn solution in PBS and is ready for cell experimentation.

GFPn solution is added directly to the samples to achieve the desired concentration. Unless otherwise noted, 10 µl of the GFPn is added to 100 µl of media in the cell sample. The GFPn solution is then allowed to incubate with the cells for 15 minutes in order to let the molecules fully incorporate themselves within the cell coat. HA patches are imaged at the glass slide level. The location of the glass is judged by the excess GFPn on the glass. Controls show that GFPn does not attach to glass without cells present and longer the cells on the glass, more GFPn concentration is present on glass.

3.2.4 Optical force probe assays (OFPA)

Optical force probe assays are performed by using a static calibrated optical trap (OT) and a programmable stage (ProScan H117; Prior Scientific, Rockland, MA). In a typical experiment, an OT holding a 3 µm passivated microsphere is positioned 20 µm outside of the PCM, where it can be translated toward and away (orthogonally) to the cell surface at 8 µm/s. The OT is paused for 5 seconds at the cell surface (always at a distance of 3 µm) and outside of the matrix. The forces on the probe are extracted by using a standard subpixel particle-tracking algorithm (102) to find the bead position in the OT. The bead height above the coverslip is ~5µm.

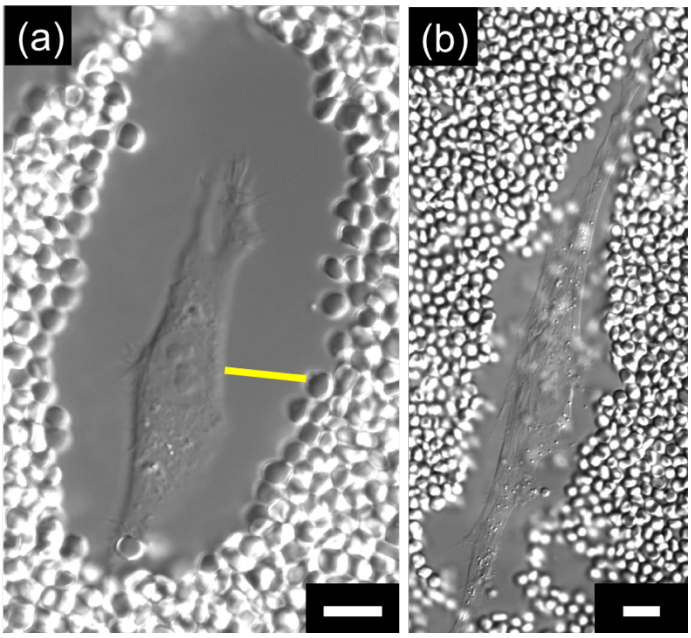

Figure 3.1: Traditional PEA on (a) RCJ-P rat's chondrocyte, (b) human mesenchymal stem cell. Yellow line indicates the position where PCM thickness is measured. Scale bar is 10 μm.

3.3 Results

3.3.1 Traditional Particle Exclusion Assay (PEA) characterization of cell lines

Characterization of the PCM using the traditional erythrocyte PEA was performed on several cell types (Figures 1.1 and 3.1), both to verify the presence of the PCM as well as for comparison with the qPEA results. More generally, we typically use PEA or fluorescent labeling of HA as a quick check for the presence of PCM before moving forward with more sophisticated assays. In these assays, the thickness of the PCM was measured to be the perpendicular distance from the plasma membrane to the edge of the erythrocytes. The measurements were performed in the middle of the side of the cell, where it is locally flat, to be consistent with the other techniques done in our lab. In other laboratories, the convention is sometimes to report the entire area of the PCM – another useful quantity. However, since we tend to think in terms of a polymer brush-like structure and try to use polymer physics to explain size, structure and other properties, the

Table 3.1: Summary of physical measurements of the PCM on RCJ-P cells.

Method	PCM Thickness
PEA	7.30 ± 0.92 μm (N=114)
OFPA Dynamic	11.50 ± 1.10 μm (N=30)
OFPA Equilibrium	8.00 ± 0.60 μm (N=30)
GFPn	6.00 ± 1.00 μm (N=30)

average thickness of the cell coat (e.g. brush) is more useful. We measure at on typical location because the relative thickness of the coat varies with position on the cell surface.

Figure 3.1a shows a typical PEA on RCJ-P cells. The PCM thickness is measured at the center on the side of the cell as indicated as the yellow line in Figure 3.1a. The average PCM thickness for RCJ-P is 7.30 ± 0.92 μm (N=114). The PCM thickness was also measured using fluorescent labeling of HA on the live cells (GFPn) and we found that the average thickness is ~6 μm (see Figure 3.2). Dr. Louis McLane, a former student in the Curtis lab also performed optical force probe assay (OFPA) by using optical tweezers (OT) to probe the PCM and found that when the probe was moving into the PCM (a dynamic measurement), a force on the probe was felt on average at distances 11.5 ± 1.10 μm from cell surface; static equilibrium OT measurements detected force (on bead held in static trap) at a distance of ~8.0 ± 0.6 μm and closer (summarized in table 3.1).

Despite measurements on the same cell line, different methods yielded different PCM thicknesses. The GFPn measurement of the cell coat thickness is similar to the visualized by PEA. But comparing to the GFPn images before adding RBC for PEA (Figure 3.2a) and after the RBC addition (Figure 3.2c), the GFPn intensity is higher at the edge of the PCM, showing HA is more concentrated at those locations. The compression of the HA at the edge of the PCM might

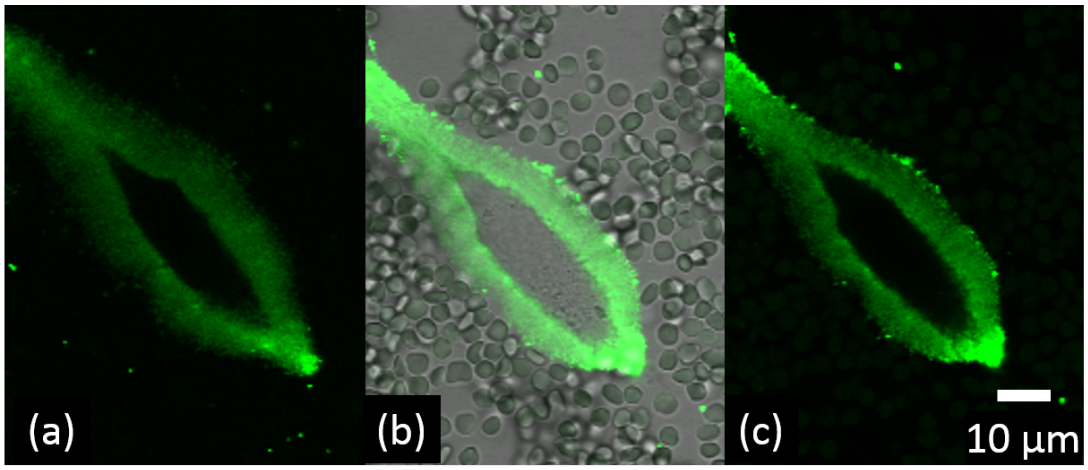

Figure 3.2: GFPn and PEA show the extent of PCM around the same RCJ-P cell (a) GFPn before adding RBC for PEA (b) superimpose image of GFPn and bright field image after adding RBC (c) GFPn image after adding RBC.

be the reason behind the detected thickness between the optical force prove and PEA. However, the GFPn labeling can also only detect the PCM up to around 6 µm due to the low concentration of HA, therefore low GFP intensity, beyond that.

Looking more closely at the images, some part of the PCM seem like there is a thin gap between the end of the GFPn signal and the location of the nearest RBC (on the left side of the cell in Figure 3.2b). It could be because the disk-like RBC are packed in a specific way and get stuck. Also it was noticed that some RBC might penetrate into the PCM more than the others depending on the orientation of the disk-like RBC (on the right side of the cell in Figure 3.2b). Again, the non-uniform shape of the RBC is decreasing the quantitative quality of the PCM thickness measurement.

On the other hand, the PCM thickness is not the same on different cell lines. To complete the record in this thesis, the PCM thickness for the following cell types we have in our lab are reported. On the human prostate cancer cells, PC3, the average thickness is 3.89 ± 0.36 µm (N=127). The breast cancer cells, MDA-MB-231, have very small PCM around them. So the PCM thickness cannot be measured by the traditional PEA. Another breast cancer cell line, Hs578T,

does not have a well-defined shape, and the PCM around those cells is seldom uniform around the cells, despite the fact that those cells produce copious amounts of HA. The average thickness reported here is taken from the thickest part of the PCM on a single cell. Many of them have no PCM thickness and that also have been factored into the average, which is 5.79 ± 0.74 μm (N=41). Human mesenchymal stem cells (MSC), have an average PCM thickness of about 6.60 ± 1.60 μm (N=72).

As mentioned above, optical force probe assay (OFPA) with optical trap technique was utilized to study the PCM. Here is a quick summary of his work (97). Optical trap pushes a 3 μm bead into the PCM. The outcome of these measurements inspired the work reported here, so the technique and results are briefly summarized here. Force on the bead can be calculated by the degree of the position deviation from center of the trap. The measurements show that the PCM is a robust yet malleable structure. The PCM tolerates repeated probing with the bead without any measurable changes. There are two different types of measurements made by the OFPA. The dynamic measurement is taken during the movement of bead and can detect the PCM presence further away from cell than the other methods (Table 3.1). The equilibrium measurement is the force measurement done after the bead stop and equilibrate at various distance to cell surface. The higher equilibrium force measured closer to the cell surface fueled the hypothesis of a varying polymer distribution, which is complementary to our observation in the next section.

As discussed in the introduction and as is evident here: traditional PEAs are an excellent tool to assess the presence of thick PCMs and for characterizing the extent in thickness and area around the cells. It is less ideal for cells with thinner PCM (or as we find cell coats comprised of long HA polymers but little bottlebrush proteoglycan) because the images are difficult to analyze and the asymmetry of the red blood cells and the error arising from their large size adds imprecision to the measurement. They may distort the PCM via pressure, as suggested by the detection of PCM at distances as far as 11 μm by dynamic optical force probe measurements.

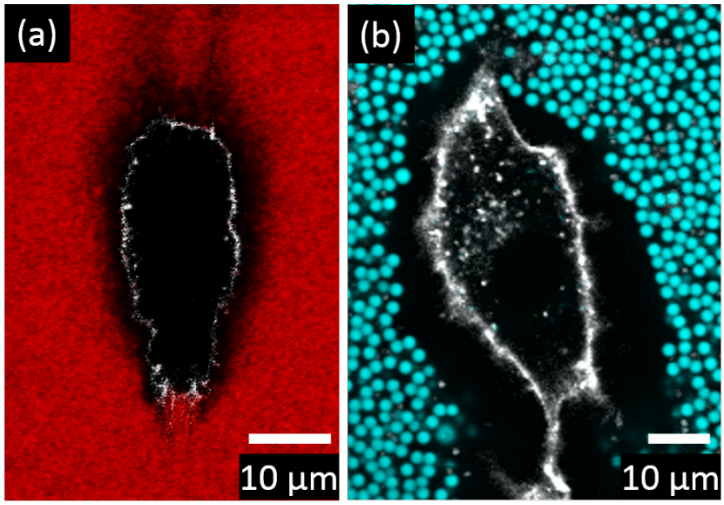

Figure 3.3 RCJ-P visualized with (a) 100 nm size particles in red and (b) 2 µm size particles in cyan. The cells membrane is shown in white by WGA staining.

Further, they provide no information to further our knowledge regarding the interior of the PCM given that the OFPA shows the PCM has an interesting varying mesh size structure (97). Therefore, we developed an improved technique to probe the internal structure of the cell coat and present it in the next section.

3.3.2 Quantitative Particle Exclusion Assay

To better investigate the structure of the PCM, we developed a complementary assay that we refer to as the qPEA. In this approach, we use passivated microspheres of well-defined sizes to probe the accessibility of the PCM for objects of different sizes (Figure 3.3). These assays show that particles become non-uniformly distributed throughout the matrix in a size-dependent fashion. To quantify the variation and size dependence, we measured the intensity profiles of fluorescent microspheres as a function of distance to the cell. Figure 3.4a shows typical intensity profiles associated with different particle sizes. A typical intensity profile for particle sizes < 500 nm consists of a nonzero intensity at the cell surface followed by a gradient of increasing intensity until it plateaus. Larger-sized beads show more abrupt changes in concentration with no transition

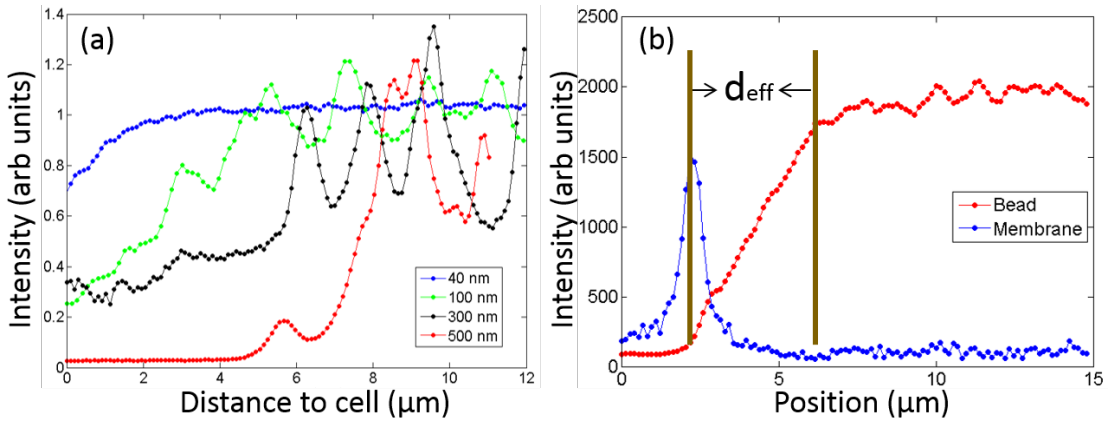

Figure 3.4: (a) Quantitative particle exclusion assay (qPEA) using monodisperse passivated beads ranging from 40 nm to 500 nm in diameter. (b) The effective thickness, d_{eff}, is measured to be distance from cell membrane to the position where bead intensity reach plateau (profile of 100 nm beads). This profile of the 100nm bead distribution is smoother than that in (a) because it is the average over 30 images taken of the same cell. The diffusing beads smooth out the variations.

zone. The oscillations in the qPEA bead profiles are due to the diffusion of the finite size particles during confocal imaging. However, as the particles diffuse about their locations, these peaks become spread out, as the confocal imaging is not instantaneous. These oscillations are smoothed out by averaging over series of images. 30 successive images are averaged to have a smoother profile (Figure 3.4b bead profile). The fluorescent bead profiles show that the bead's concentration is the lowest at the cell membrane and roughly plateaus at a distance, we term it effective thickness, that depends on the particle size. The effective thickness, or d_{eff}, is measured by the distance between the cell membrane to the plateau of the bead intensity, as showed in Figure3.4b. We extracted the average effective thickness for particle diameters of 40 nm, 100 nm, 200 nm, 300 nm, 400 nm, 500 nm, 2000 nm, and 3000 nm, as shown in Table 3.2.

Analysis of the particle distribution as a function of bead diameter show that the PCM acts as a sieve for passivated particles of different sizes. Figure 3.5b shows how the average effective thickness of the coat increases with increasing particle diameter, with results given for bead sizes ranging from 40 nm to 3000 nm. This result that different sized particles penetrate different

Table 3.2: Effective thickness of RCJ-P control cells shows varying pore size in the matrix.

Microsphere sizes	Control RCJ-P cell d_{eff}
RBC	7.30 ± 0.92 μm (N=114)
40 nm	1.40 ± 0.32 μm (N=22)
100 nm	3.64 ± 0.40 μm (N=32)
200 nm	5.28 ± 0.78 μm (N=25)
300 nm	6.67 ± 0.54 μm (N=44)
400 nm	7.13 ± 0.62 μm (N=35)
500 nm	8.69 ± 0.58 μm (N=72)
1 μm	8.09 ± 0.60 μm (N=81)
2 μm	8.13 ± 0.90 μm (N=39)
3 μm	8.56 ± 1.40 μm (N=11)

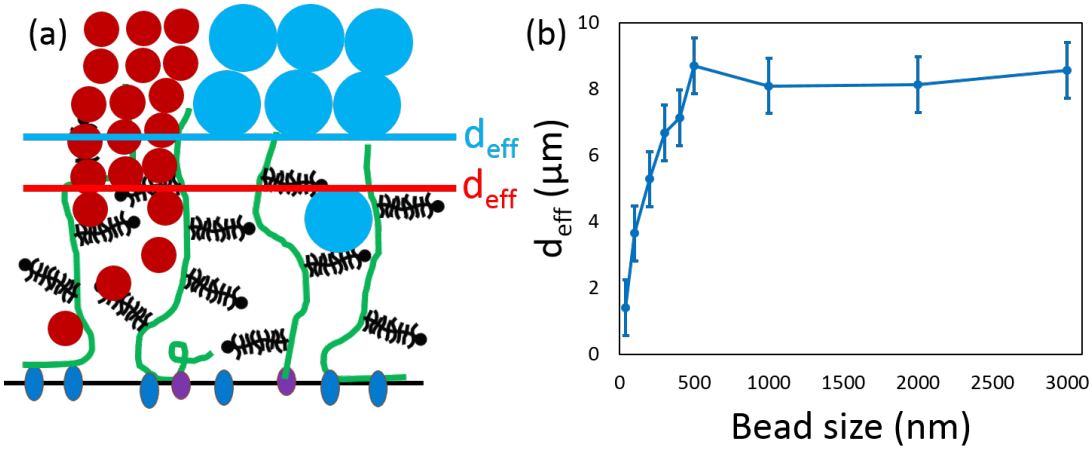

Figure 3.5 (a) Schematic of the qPEA showing measurements of d_{eff} for different bead sizes. Experimentally only one bead size is added at a time. (b) The effective thickness associated with bead size increases until it plateaus at ~ 8.5 μm where 500 nm size beads and larger are excluded from the PCM completely.

distances into the cell coat is consistent with the optical force measurements, suggesting that the ability of particles to penetrate the pericellular matrix decreases as the particle size increases, confirming that the mesh size is indeed spatially varying. Interestingly, particle sizes of 500 nm and greater have the same average effective thickness, $d_{eff,500}$= 8.5 ± 0.8 μm, suggesting that this is the edge of an inner domain within the PCM. This measurement of the edge of the cell coat is also consistent with the equilibrium thickness measured by the optical force studies, which is 8.0 ± 0.6 μm. However, it is slightly larger than the mean thickness of the red blood cell PEAs, 7.30 ± 0.92 μm, and the fluorescent HA assay, 6.00 ± 1.00 μm, as discussed below.

3.4 Discussion

The different methods of probing the PCM are shown. While they each reveal new and interesting information about the structure of the cell coat, comparison between the two assays strengthens the results and our interpretation of what these results reveal about the PCM. The optical tweezer force probe assay (OFPA) results were used to extract a pore size profile throughout the coat. Correlation length can also be thought of a ‘mesh size’, or an average opening within the polymer mesh. This non-constant correlation length profile is interpreted to mean that the average opening in the cell coat is not constant, and that the size of the openings within the coat increases at distances further away from the cell membrane. We take this concept, and use it to directly compare the OFPA results to the results from the quantitative particle exclusion assays (97). The qPEAs revealed that the cell coat acts like a sieve, separating particles by their size. Smaller beads were able to penetrate further, as their smaller sizes apparently permit them to fit inside the tighter spaces within the cell coat. This section directly compares these results in order to develop a cohesive understanding of the PCM structure.

Conceptually, the results from the OFPA and qPEA studies are highly compatible, as a varying correlation length can be directly interpreted that that the coat acts like a sieve for the cell. With the mesh size, or average opening within the coat, being smaller closer to the cell surface

larger particles will be stuck outside the cell while the smaller particles are allowed to penetrate through the cell coat. This would allow smaller molecules such as growth factors to reach the cell surface, while larger possibly undesirable matter is kept away from the cell surface. The qPEAs directly demonstrate that the cell coat behaves in this manner. The position to where a particle can easily penetrate, defined as the effective thickness (d_{eff}), correlates directly with bead size, where larger particles are held further away from the cell membrane.

Further, the qPEA results can be semi-quantitatively compared to the correlation length profile predicted by the OT work. Recall that the effective thickness, deff, for a particle is the distance to the cell surface at which the concentration of the particle distribution reaches a plateau. At this location the mesh size of the coat is considered to be the same as the size of the particle. Thus particles can easily penetrate any regions of the coat where the mesh size is larger than their diameter. However when the particles reach a mesh size that is smaller than their diameter they are stopped by the PCM, as they can no longer easily diffuse past this point. Some of the particles do pass this point, but this is likely due to the fact that the coat is not a stiffly crosslinked network, as fluctuations in mesh size and particle position result in some of the particles passing this point. The qPEA profile can then be thought of as a probability distribution for the positions of a particle within the cell coat.

Thus for a quasi-quantitative comparison, we conjecture that the bead size corresponds roughly to the correlation length in the PCM at the effective thickness where that bead size shows constant concentration. In other words, the d_{eff} from the qPEA results corresponds to the distance to the cell, and the bead size corresponds directly to the correlation length at this position. We note that 40 nm bead data are excluded from this comparison because the plateau is at $d_{eff,40}$ = 1.4 ± 0.3 μm, a distance where microvilli complicate the PCM structure on RCJ-P cells (103). With these assumptions, the qPEA data can be recast as correlation length versus position in the pericellular coat. Overlaying the optical force data with the *ad hoc* qPEA curve provides a visible comparison as shown in Figure 3.6. Overall they qualitatively agree, as both depict an increasing

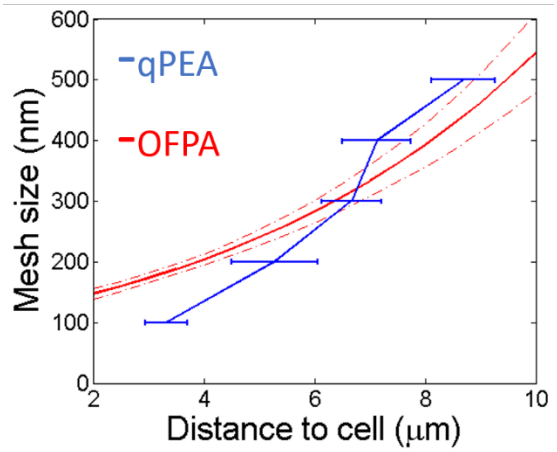

Figure 3.6: Comparison between the correlation length profile calculated from the optical force probe assay (OFPA) and the quantitative particle exclusion assay (qPEA) data.

mesh size for increasing distances from the cell. Additionally, for beads larger than 200 nm the two agree within error. Although they do not fully agree quantitatively, the two assays are conceptually consistent as they both show an increasing mesh size at distances further from the cell membrane.

The data extracted from the optical force probe and qPEA assays together provide strong evidence that the pericellular matrix has a spatially varying mesh size. The penetration of 40 nm particles to the surface and their uniform distribution at $d_{eff,40}$=1.4 μm suggests the mesh size ranges from a sub-100 nm length scale near the surface to ~500 nm at a distance of approximately eight microns from the cell surface. The comparison of the qPEA results to the correlation length profile refines our grasp of the true values for the mesh size of the cell coat, as the calculation of the correlation length is only semi-quantitative given the fact that there is an unknown scaling factor in its result.

We tried qPEA measurement on the same cell to have a better size-dependent d_{eff} comparison, but when performing qPEA with 100 nm and 1 μm beads, the effective thickness of the larger size bead fluctuated too much. The average thickness when measured with 1 μm beads alone is 8.09 μm, but when doing the qPEA with a smaller bead size (100 nm), the thickness

measured by 1 μm ranged from 3 μm to 12 μm, which was unusual in qPEA. There might be dynamic interactions between different sizes beads. To stay on track of our mission for characterizing the PCM structure, we suspended the effort for multi-size qPEA on the same cell.

The large size qPEA measure the outer edge of the PCM is at 8.5 μm where the RBC showed just a ~7 μm thick coat. As discussed before, RBC tend to compress the PCM. Also, the non-uniform size and shape of the RBC make it hard to be accurate in the thickness measurement. qPEA improves on that.

Comparing the qPEA technique to GFPn labeling, the two methods are quite different. GFPn shows the direct distribution of the PCM structure, while qPEA maps out the PCM microstructure by showing the empty space inside the matrix. And that in turn gives us an insight into how molecules can access to the cell surface. These two techniques are complimentary to each other. The information of the HA distribution combines with the open space distribution inside the matrix obtained by qPEA, the presence and distribution of other molecules, such as the large bottlebrush CSPG, could be inferred. More work on the two techniques done on the single cell is needed to have further insight.

We briefly acknowledge a few disadvantages of the qPEA assay. Most importantly, although the effect is small, the beads inside the PCM occupy the available space for the polymers and therefore change the dynamics and the configuration of the polymers. More work is needed to determine how critical this impact is. For the smaller beads (40 nm), after they reach the cell surface, they sometimes aggregate on the membrane despite the passivation or are endocytosed by the cell. This might disrupt the cell health or block hyaluronan synthesis or binding (to CD44) and interfere with long term experiments.

A technical issue worth mentioning is that during qPEA, because of the high diffusivity of the microspheres and their small size, bright field images cannot be taken to identify their positions. Indeed, even with a confocal microscope, at the concentrations used here and the sizes, dynamic imaging of the position of the beads is difficult (although our lab did do passive

particle micro-rheology of 300 nm particles in the PCM in the past (103)). This however, worked to our advantage because we were primarily interested in the probability of a particle being a certain distance from the cell surface. Therefore, blurred snapshots of particles in transit were acceptable. Indeed, we even averaged over many images (N=30) in order to achieve smoother profiles.

3.5 Conclusion and Outlook

The PCM is a neglected but important construct of single cells. A growing body of evidence suggests that the mechanical and structural properties of this cell-associated matrix influence numerous physiological processes. Meanwhile, researchers working in bioengineering and drug delivery are increasingly concerned with the influence of the PCM, and possible opportunities to manipulate it to realize their applications. In similarity to other passive and active micro-rheology approaches used to interrogate the viscoelastic properties of cells, in this work we introduce novel physical assay to nondestructively interrogate the organization of the PCM. We developed a novel qPEA to look at the size-dependent diffusion of (passivated) particles into the PCM. To the best of our knowledge, our assays provide the first quantitative evidence that the pore size of the PCM varies with distance to the cell surface. The spatial and chemical variations in the cell coat will greatly influence the transport of objects and molecules to and from the cell surface. In these studies, we minimized the role of chemical interactions to focus on steric exclusion by using PEGylated particles. The outcome demonstrates that even without the electrostatic repulsion or chemical interactions that are expected to occur in the highly negatively charged matrix due to bottlebrush CSPGs, access to the cell surface is affected by the cell coat microstructure. This has direct implications for cell defense against viral and bacterial infections, and drug delivery applications.

In conclusion, this work introduces the novel (to our knowledge) biophysical strategy to interrogate the PCM. Our investigations uncovered valuable microstructural details about the

PCM on RCJ-P cells. Experiments showed that the PCM has a varying pore size and can sieve incoming nanoparticles by their sizes. These insights and others that will be gained in future work based on these tools should provide researchers with useful clues to unravel the mechanisms by which the PCM influences so many fundamental biological processes.

Chapter 4

Cell surface access is modulated by tethered bottlebrush proteoglycans

4.1 Overview

The cell interface is critical in mediating the integration of cells into tissue via extracellular matrix (ECM) and cell-cell contacts. Cells that maintain hyaluronan-rich sugar coats on their surfaces may have enhanced capabilities to manipulate their very local environment and hence direct their interactions with cells and the ECM (13, 14) (Figure 4.1). This is particularly relevant in dynamic tissue environments, where sugar cell coats are involved in the regulation of a wide range of processes that involve cell rearrangements including cell migration (41, 42, 76), division (104), synaptogenesis (105), morphogenesis (3, 106), cancer progression and metastasis (107–109). The aim of this study is to investigate the physical role that the hyaluronan sugar coat plays in mediating cell surface access.

The potential significance and impact of the hyaluronan-rich cell coat, also called the pericellular matrix (PCM), is immediately evident when glancing at a cell endowed with a cell coat (Figure 4.1). On many cell types, the PCM extends more than 5 microns from the cell surface and on some cell types it extends up to 20 microns (14). Indeed, PCM visualization is traditionally achieved by utilizing one of the important properties of this surface-anchored polymer matrix, *i.e.* its ability to repel objects from the cell surface (Figure 4.1b). There are three essential components in the cell coat (14): the linear carbohydrate hyaluronan (HA), HA-binding proteins at the cell surface, and HA-binding bottlebrush-shaped proteoglycans, also known as hyalectins (110). In the PCM, HA polymers are anchored to the cell surface by proteins (e.g. CD44, RHAMM) or they remain tethered to the enzyme HA synthase, which directly extrudes HA from the plasma membrane. With lengths ranging from ~2-25 μm (13), cell-surface tethered HA becomes significantly stretched when it aggregates bottlebrushes along its chain. The family of hyalectins

which includes aggrecan, versican, neurocan and brevican, consists of core proteins that are extremely similar within the N- and C-terminal globular domains and have central domains of variable length with multiple sites for the addition of chondroitin sulfate or dermatan sulfate chains and O-linked oligosaccharides. The hyalectins are present in the ECM and PCM of many tissues, with aggrecan featured in cartilage, brevican and neurocan abundant in the central nervous system, and versican expressed in most soft tissues of the body (111). All hyalectins contain a common HA-binding domain (G1) that allows them to aggregate densely along HA, nearly permanently when reinforced by an additional protein called link protein (30). The key physical characteristics of the bottlebrush proteoglycans stem from a second domain (G2) that contains a dense region of highly-sulfated glycosaminoglycans. The third and last domain (G3) is smaller and consists of specific binding sites for various biomolecules. Cell coats can exist without bottlebrushes but unless the HA is grafted so densely that a polymer brush forms (as on some bacteria (112)), the PCM is relatively thin even when comprised of large HA molecules. It is the aggregation of bottlebrush proteoglycans in the PCM that generates its voluminous expansion on most mammalian cells (30, 113), and which dominates the physical and chemical functions of the PCM.

Little work has focused on spatial characterization of bottlebrush molecules in the cell coat nor how their distribution and physical properties impact accessibility of the cell surface. Most biophysical studies have focused on structural and biomechanical properties (97, 103, 114, 115). While chondroitin sulfate proteoglycans are known to have important biochemical roles (35, 111), their unusually large size, their ability to be densely aggregated on HA, and their high negative charge should also strongly influence the physical interaction of proteoglycan-rich PCM (and ECM) with molecules (35), cells (15) and particles (43) including drug delivery vehicles, exosomes, and supermolecular aggregates. The work presented here examines the spatial distribution of bottlebrush proteoglycans in the PCM of living cells. We demonstrate how objects

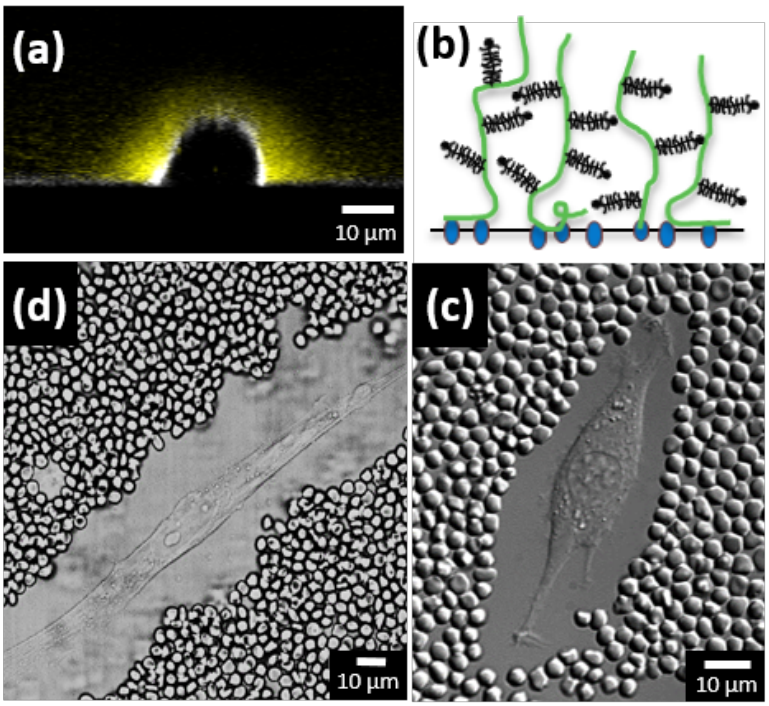

Figure 4.1: (a) Cross-sectional confocal image of pericellular matrix swollen with exogenous aggrecan on RCJ-P cell (c_{ACAN}=333 µg/mL, yellow=aggrecan, white=plasma membrane). The PCM extends in a three dimensional halo around the cell, with aggrecan intensity visible at distances more than 20 µm from cell surface. (b) Schematic of the PCM. Hyaluronan polymers (green) bind to the plasma membrane via HA-binding membrane proteins (blue). Bottlebrush proteoglycans (black) bind along the chain and stretch the HA into an extended configuration. (c) Erythrocyte particle exclusion assay shows the extent of the cell surface-grafted PCM on aggrecan-saturated mesenchymal stem cell (333 µg/mL for 2 hrs). (d) Erythrocyte particle exclusion assay shows the extent of the cell surface-grafted PCM on a native RCJ-P cell.

40 nm and larger are altered in their access to the cell surface; we report that free bottlebrushes diffuse through the PCM, and demonstrate that positively charged molecules become sequestered in the PCM on chondroitin sulfate side chains of bottlebrush proteoglycans. These systematic investigations have direct implications for PCM function and are a first step towards delineating the physical roles of bottlebrush proteoglycans in diverse range of contexts and tissues.

4.2 Materials and Methods

All data are reported with 2 standard error in text and in plots.

4.2.1 Cell culture and sample preparation

Rat chondrocyte joint (RCJ-P) cells (fetal calvaria, batch 15.01.98; Prochon Biotech, Rehovot, Israel) were cultured under 37°C, 5% CO_2 with α-MEM, 15% FBS, 2% L-glutamine. Mesenchymal stem cells (MSC) (human bone marrow-derived, Texas A&M, College Station, TX) were cultured at 37°C, 5% CO_2 with α-MEM, 16.5% FBS, 2mM L-glutamine, 100 U/mL penicillin and 100 µg/mL streptomycin. Cells were seeded on glass coverslips in Teflon sample holders for ~20 hours to achieve 50% confluency of the 0.8 cm^2 surface with 2 mL of media. During the imaging, samples were held at 37°C, 5% CO_2 and 80% humidity with a stage-top incubator (N.E.-MSI 07-3156; Okolab, Ottaviano, Italy).

4.2.2 Particle exclusion assay (PEA)

Traditional PEA: fixed sheep erythrocytes (R3378; Sigma Aldrich, St. Louis, MO), were suspended in PBS and then added to the sample with a final concentration of 1 mg/mL to achieve mono-layer after 10 mins. Thickness of the PCM was measured to be the perpendicular distance from the cell plasma membrane (at the flattest location on the cell, usually the middle) to the nearest erythrocyte.

Quantitative PEA (qPEA): fluorescent polystyrene spheres (FluoSpheres; Invitrogen) of different sizes were passivated before use in qPEA. Larger particles (>200 nm) were reversibly swollen with toluene to enable physical entanglement of Pluronic F127 as previously described (99). Smaller particles were covalently modified with methoxypolyergylene glycol amine (Fluka, St. Louis, MO) (100). For qPEA, 22 µL of the microspheres (5% solid) were added to 178 µL

media and allowed to settle for 10 min. To facilitate image analysis, the cell surface was fluorescently labeled with wheat germ agglutinin (WGA-Alexa Fluor 633 conjugate; Sigma), which was added to the sample (125 μg/mL) 5 mins before measurements were obtained. The samples were imaged with a confocal microscope (FV1000; Olympus, Tokyo, Japan). Microsphere distribution was measured by taking the fluorescence intensity perpendicular to the cell surface at 3 μm above the glass surface and averaged over 2 μm. The effective thickness, d_{eff}, identified to be the distance between cell surface and the plateau in the average bead intensity.

Bacterial PEA: cells were intentionally exposed to non-sterile environment in lab and allowed to go resultant bacterial infection.

4.2.3 Time-dependent swelling of PCM

PCM of RCJ-P cells were visualized with PEA. Then 333 mg/mL aggrecan was added to the sample. The PEA is then used to monitor the aggrecan-driven extension of the cell coat versus time.

4.2.4 Fluorescent protein labeling

Bovine articulate aggrecan (A1960; >2500 kDa, Sigma Aldrich, St. Louis, MO) was dissolved in PBS to reach 2 mg/mL. Histone type II-A (H9250; ~20kDa, Sigma Aldrich, St. Louis, MO) was dissolve in PBS to reach 1 mg/mL. Similar procedures used for BSA 66 kDa, AP-4510-60; SeraCare Life Sciences, Milford, MA). Fluorescent-labeling was achieved by incubating the protein with ATTO NHS ester dye at 2 mg/mL for one hour followed by a Zeba desalting column (89882; Thermo Scientific, Waltham, MA) to remove excess dye.

4.2.5 Optical force probe assays

Optical force probe assays were performed by using a static calibrated optical trap (OT) and a programmable stage (ProScan H117; Prior Scientific, Rockland, MA). In a typical experiment, an OT holding a 3 μm passivated microsphere was positioned 20 μm outside of the PCM, where it could be translated toward and away (orthogonally) to the cell surface at 8 μm/s. The OT was paused for 5 seconds at the cell surface (always at a distance of 3 μm) and outside of the matrix. The forces on the probe were extracted by using a standard subpixel particle-tracking algorithm (102) to find the bead position in the OT. The bead height above the coverslip was ~5μm.

4.2.6 Fluorescent aggrecan exchange assay

Cells were incubated with the fluorescent aggrecan (333 μg/ml concentration) for two hours at 37 °C and 5% CO_2. Media was replaced with fresh media without aggrecan before imaging the initial fluorescent aggrecan distribution with a confocal microscope (FV1000; Olympus, Tokyo, Japan). The media was then replaced (within 1 minute) with non-fluorescently labeled aggrecan solution (333 μg/ml concentration), and then imaged over time to monitor the fluorescent intensity of the aggrecan in the PCM. All fluorescent intensity profiles were taken perpendicular to the center of the cells at 3 μm height and averaged over 2 μm.

4.2.7 GFPn labeling of hyaluronan

Fluorescent labeling of HA was achieved using neurocan-G1 EGFP fusion protein (GFPn) expressed by HEK 293 EBNA cells, which were cultured at 37°C and 5% CO_2 in DMEM/F12, with 10% FBS, 1% L-glutamine with 0.1% puromycin (EMD Biosciences, CA) (96, 103). Cells were grown to confluence, at which time serum was removed from culture media and the cells were

then incubated for 48 hours under serum free conditions. 50 mL of conditioned media was collected from a total of 5 culture flasks and concentrated to ~2 mL by centrifugal ultrafiltration with a membrane cut-off of 30 kDa (Millipore, MA). The His-tagged fusion protein was purified on a HisPur Cobalt spin column (Thermo Scientific, IL). During HA labeling, 10 µL of GFPn was added to 90 µL of sample for 15 min incubation.

4.2.8 Chondroitin sulfate digestion assay

Chondroitinase ABC (ChABC) from Proteus vulgaris (C2905; Sigma Aldrich, St. Louis, MO) was used to digest the chondroitin sulfate side chains of aggrecan. ChABC was dissolved in PBS and then directly added to cell sample to achieve a final concentration of 0.27 unit/mL.

4.3 Results and Discussion

4.3.1 PCM swells with increasing aggrecan concentration

The bottlebrush proteoglycans largely determine the extent of the PCM (together with HA length). The PCM can be removed from the cell surface by digestion of the HA with enzymes; or it can be collapsed to a thin layer at the cell surface by digestion of the chondroitin sulfate side chains on the proteoglycans. Treatment of RCJ-P chondrocyte cells and human mesenchymal stem (MSC) cells with chondroitinase ABC (ChABC) nearly eliminates the native 7 µm thick PCM on both cell types (Figure 4.2). Upregulation of versican increases the thickness of PCM on smooth muscle cells (116), whereas work in our lab confirms that down regulation of aggrecan expression with si-RNA in RCJ-P cells eliminates the PCM detectable by particle exclusion assay or optical force probe assays (data not shown). Interestingly, Knudson *et al* showed that both digested and displaced pericellular matrices can be reconstructed by the addition of exogenous

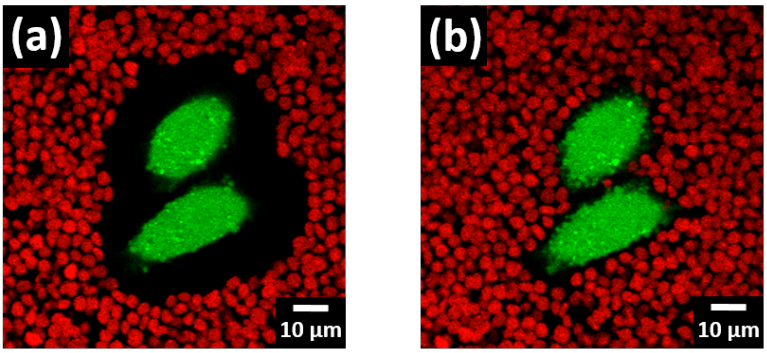

Figure 4.2: Treatment with chondroitinase-ABC (ChABC) at concentration of 0.27 unit/mL degrades the PCM in less than five minutes, as determined by erythrocyte PEA (a) before and (b) after treatment (5 mins later). The remaining gap between the erythrocytes and the cell surface is likely from the surface bound hyaluronan which is still decorated by the protein backbones of the ACAN. Cells are labeled with 1 µM calcein.

HA and aggrecan, where aggrecan is an essential component for the detectable matrix by particle exclusion assays (30, 113).

Following a similar approach to that of Knudson but without first digesting the cell coat, we examined how the equilibrium thickness of the PCM varies with the solution concentration of exogenous aggrecan. For RCJ-P and MSC cells, the PCM width increases until it plateaus at a value 250% larger than its original thickness (7.0 ± 0.9 µm; 6.6 ± 1.6 µm; N_{RCJP}=114; N_{MSC}=72). For the RCJ-P cells, the PCM thickness reaches a maximum size of 17.8 ± 1.2 µm at c_{ACAN}=180 µg/mL (N=73). For the MSC cells, the critical concentration to achieve maximal extension is slightly higher, c_{ACAN}=260 µg/mL, with a similarly large extent of 18.0 ± 1.0 µm (N=75). This data was obtained by image analysis of traditional erythrocyte particle exclusion assays (PEA) (Figure 4.1b) of cells after incubation with exogenous aggrecan for two hours (40). We performed time-dependent studies of the swelling of the PCM (c_{ACAN}=333 µg/mL) to confirm that two hours is sufficient to reach equilibrium (Figure 4.3b). This is consistent with Knudson *et al*, who waited 30 mins and 2 hrs respectively to reconstitute cell coats on hyaluronidase-treated chondrocytes (113)

and other cells types (30) using much higher concentrations of aggrecan (2 mg/mL) together with exogenous HA (c_{HA}=1 mg/mL).

It is unlikely that the PCM swelling is due to increased HA synthesis or elongation of HA synthase (HAS)-bound HA strands. HA synthesis is regulated through transcriptional activation of HASes by growth factors and cytokines or regulated by post-transcriptional events like phosphorylation (79). Furthermore, in their reconstituted PCM assays, Knudson *et al*. performed controls comparing the final thickness of the PCM on living and fixed cells, demonstrating the same outcome (30, 113). Instead, we infer that the PCM swells as aggrecan binds to free sites on the HA, further stretching out of the polymer in an aggrecan concentration dependent manner (117, 118). Swelling might also be partly driven by the formation of a polymer brush type scenario, since overlap of the grafted HA strands might increase with exogenous aggrecan binding (119, 120).

The significant increase in PCM thickness provides the somewhat surprising insight that many of the bottlebrush binding sites in the PCM remain available despite the already naturally swollen coats of RCJ-P and MSC cells (~7 μm). Further, for the PCM to expand to such large sizes, particularly on the RCJ-P cells which we have shown has no measurable crosslinking in the PCM (97), the HA strands must be at least 18 microns in length (~7.5 MDa, 1 disaccharide~1nm ~400 Da (121)) or it requires that the PCM is comprised in part by free HA strands entangled with surface bound strands (122). This is unlikely, however, as several studies of biomimetic HA-aggrecan systems suggest that such uncrosslinked multi-layers do not occur (123, 124). Lastly, we infer differences between the MSC and RCJ-P cell PCMs by comparing the difference in exogenous aggrecan concentration to reach maximal PCM. While the final size is similar, higher aggrecan concentration is needed for the MSC, suggesting more free HA binding sites than in the RCP-P cell coat. In the next sections, we present data on the distribution of the

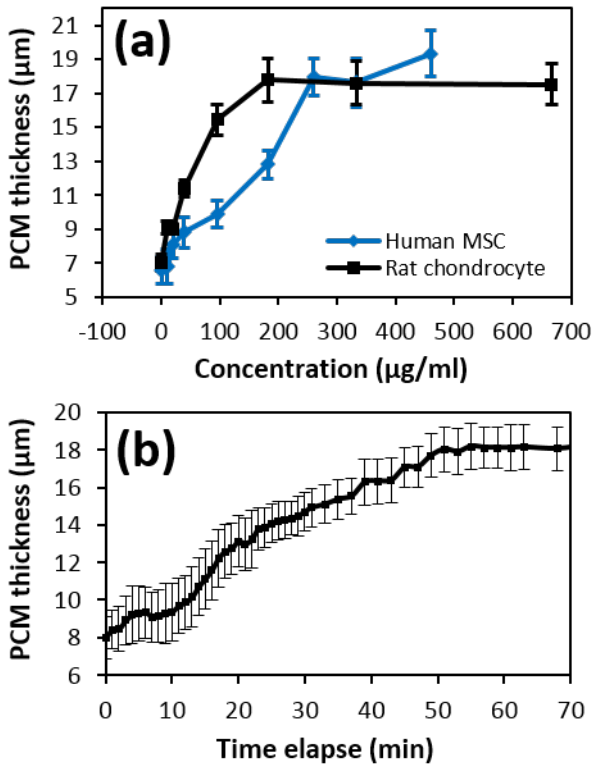

Figure 4.3: (a) PCM thickness measured perpendicular to the cell surface on human bone marrow derived mesenchymal stem cells (MSC) and rat chondrocytes (RCJ-P) versus exogenous aggrecan concentration. (b) Time-dependent swelling of the PCM after addition of aggrecan shows that reaching equilibrium extension requires one hour (c_{ACAN}=333 µg/mL). Data is an average for N=10 cells with 2 standard error reported.

available binding sites in the PCM of RCJ-P cells, and explore how tuning aggrecan concentration can affect cell interactions with the surroundings.

4.3.2 PCM maximal extension occurs before bottlebrush saturation

The spatial distribution of PCM-tethered bottlebrush molecules likely dominates access to the cell surface by molecules, nanoparticles, exosomes, and the protrusions/surfaces of other cells. Yet, few quantitative data supporting this hypothesis (78). For example, there is no accurate spatial map of the endogenous aggregating proteoglycans in the PCM on single living cells. In

most studies, the natural PCM structure is destroyed by fixation before labeling for bottlebrush proteoglycans (122, 125). Indeed, despite our own efforts, we have been unable to reliably label endogenous aggrecan on living RCJ-P cells using standard methods.

In an alternative approach, we use fluorescently labeled exogenous aggrecan to study the spatial distribution of aggrecan in the PCM. Figures 4.1a and 4.4a present typical examples of a cell coat enriched with aggrecan (333 and 39 μg/mL, 2 hrs). Profiles of the variation of aggrecan fluorescence versus distance to the cell surfaces were extracted from the same position of the PCM as used for PEA thickness. Confocal images of the PCM taken at a fixed height (3 μm) above the coverslip show that at all solution concentrations, the bound aggrecan intensity peaks close to the cell surface and then decays rapidly (Figure 4.4b). The curves in Figure 4.4b show the average intensity distribution at different concentrations (c_{ACAN}=39, 260, 333, 460 μg/mL, N~20 for each). Fits to the averaged data reveal an exponentially decaying curve for all aggrecan concentrations. At higher concentrations, the intensity decreases less rapidly, possibly due to the stretched out HA and its more uniform coverage by aggrecan. At distances beyond the edge of the PCM detected by PEA, there is a non-negligible background fluorescence.

The results indicate that the many of the available binding sites in the PCM are located within a few microns of the cell surface. The majority of the incorporated exogenous aggrecan appears within 6 μm of the plasma membrane (67, 70, 50, 56, 50, 55% for concentrations c_{ACAN}=39/ 95/ 180/ 260/ 333/ 460 μg/mL).

For concentrations of 180 μg/mL and above, more than 50% of the aggrecan are incorporated within the inner 35% of the PCM. This is due to a higher density of HA strands in this range, whereas a lower number of long HA strands are available to stretch from the cell (103). This is visible, for example in Figure 4.1a. The PCM of these cells extends to an average of ~18 μm under these conditions according to PEAs and is visible out to ~12 μm using fluorescent aggrecan profiles. Speckles representing fluorescent aggrecan are apparent in the region beyond

about ~10 μm. In a related work, we use this observation to study the motion of individually bound aggrecan molecules as a function of distance to the cell surface.

Little difference is apparent between the fluorescent profiles of cells treated with c_{ACAN}=333 versus c_{ACAN}=460 μg/mL aggrecan. This indicates that the free binding sites saturate at values above 333 μg/mL. Interestingly, the saturation value is much higher than the solution concentration needed to fully stretch out the PCM (c_{ACAN}=180 μg/mL). This data provides evidence that the HA strands stretch to near full extension and then the remaining binding sites along the HA are filled by additional bottlebrush molecules.

4.3.3 Fluorescent aggrecan assay reveals free binding sites in PCM

The equilibrium distribution of exogenous aggrecan shown in Figure 4.4b depends in part on the binding affinity of the endogenous aggrecan. Previous studies suggest that *in vitro* and *in vivo* endogenous aggrecan is very strongly bound to HA due to its reinforcement by link protein, which simultaneously binds both to the aggrecan and HA (111). Knudson *et al* state that the link protein stabilized binding of aggrecan is non-dissociating and non-displaceable under physiological conditions (126). Our data is consistent with the endogenous aggrecan stability in the PCM of RCJ-P cells. For example, exchange of media does not significantly alter the PCM size suggesting that the majority of endogenous aggrecan are stably bound and unaffected by shifts in aggrecan solution concentration (Figure 4.5). We therefore estimate that the majority of endogenous aggrecan in the cell coats remains localized during the treatments for our studies.

Thus, the profiles of exogenous aggrecan at saturation (>260 μg/mL) provide a rough map of the available binding sites in the PCM. This distribution should not be confused, however with

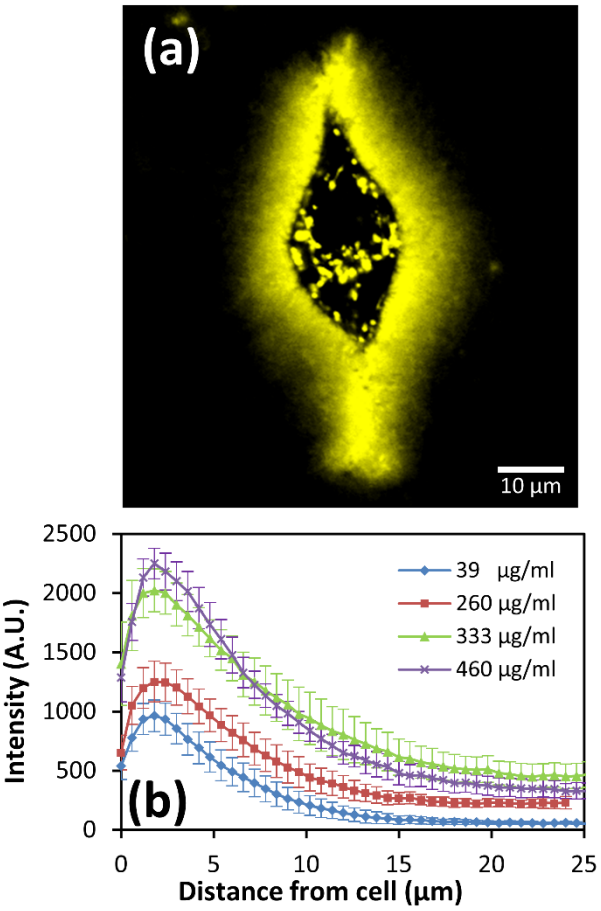

Figure 4.4: (a) Fluorescently-labeled exogenous aggrecan at low concentration (39 µg/mL) swells the PCM. (b) Profiles of the aggrecan distribution versus distance to the cell surface at four concentrations.

the availability of binding sites along a single HA strand, since the data is weighted by the natural density variation of HA in the PCM. Fluorescent labeling of the HA shows that the RCJ-P cell coat has a higher density of HA near the cell surface which decays exponentially in the absence of exogenous aggrecan (103). Such spatial concentration variation arises in part from the physics of adsorbed HA strands (127), but also is likely due to HA polydispersity. As expected, when aggrecan-saturated PCMs are labeled for HA, the aggrecan and hyaluronan have nearly identical profiles (Figure 4.6).

	% change in thickness	% 2 Standard Error	Number of cells
Positive change	5.49	2.95	27
Negative change	-7.26	1.72	46

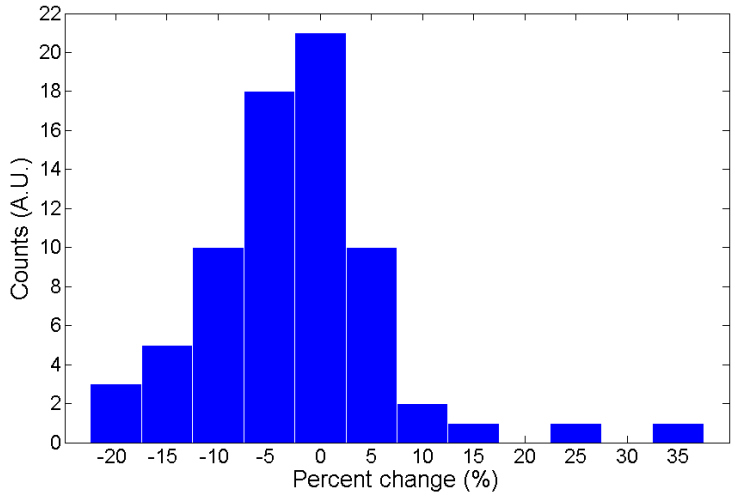

Figure 4.5: The PCM is slightly perturbed by gentle exchange of the media. Measured using particle exclusion assays (PEA), we found that PCMs change less than 10% in width (increase or decrease). This is approximately the resolution of the erythrocyte PEA. This change may result from the loss of endogenous ACAN, whose binding is necessary for swollen PCM; or it could be due to loss of HA strands due to the perturbation, or some combination of the two processes. Given the small change in thickness, we surmise that most of the endo-ACAN is tightly bound to the HA by the reinforcement garnered by link protein.

The remarkable implication from these observations is that RCJ-P cells have access to a sizable parameter space, c_{ACAN}=180 to 333 μg/mL, over which they can maintain a maximized PCM thickness, while leaving the possibility to tune the aggrecan concentration and hence the binding sites for molecular sequestration (specific and non-specific sites on the bottlebrushes) and the PCM permeability to nanoparticles, extracellular matrix and cell protrusions.

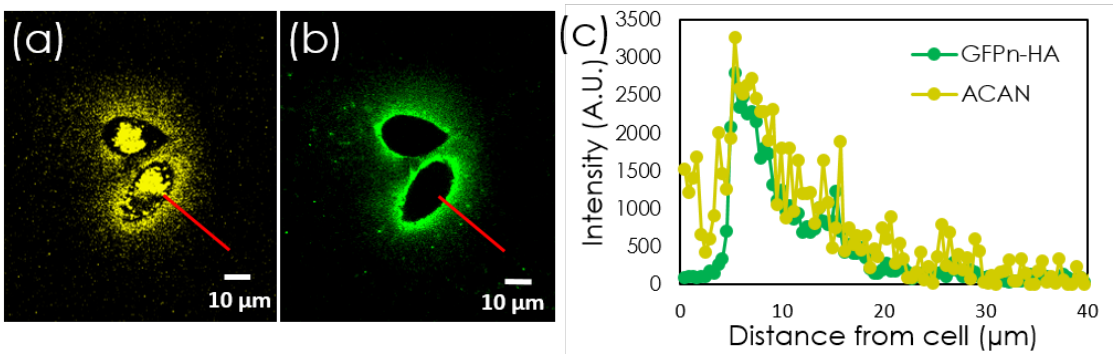

Figure 4.6: Aggrecan co-localizes with hyaluronan in the cell coat. Cells were incubated with fluorescent aggrecan (333 µg/mL, 594 nm) for two hours, followed by incubation with GFPn (0.15 µM, 488 nm) for 10 minutes. (a) Fluorescent image of aggrecan distribution in the PCM. (b) Fluorescent image of HA labeled with GFPn. (c) Profiles of HA and ACAN taken perpendicular to the cell surface.

4.3.4 Bottlebrush-enriched PCM has reduced mesh size and permeability to nanoparticles

The transport of molecules and nanoparticles to the cell surface is broadly relevant for understanding cell-cell communications, drug delivery and tissue homeostasis. The local physicochemical environment associated with the PCM is an additional layer worth investigating independently from the ECM that will impact these processes. Previous work has examined the permeability of the cell coat to nanoparticles (64, 78, 97, 103, 128, 129), the free diffusion of particles in the PCM (64, 103, 128, 129), and quantified the 'mesh size' variation in the PCM using quantitative particle exclusion assays (qPEA) and optical force probe microscopy (78, 97). Here we use qPEAs to characterize changes in PCM permeability and mesh size after it has been saturated with exogenous aggrecan (c_{ag}=333 µg/mL).

In earlier work, we showed that inert nanoparticles, unlike erythrocytes, are able to penetrate into the RCJ-P cell coat in a size-dependent fashion (Figure 4.7a). For particles small enough to penetrate, gradients in the particle concentration are established in the PCM, where

the spatial distribution depends on the particle size (Figure 4.7b). We estimate that the local 'mesh size' roughly equals a given particle size at the location, d_{eff}, where the particle distribution plateaus (97). Thus, we can generate a map of the mesh size versus distance to the cell surface. The mesh size decreases in a roughly linear fashion towards the RCJ-P cell surface (Figure 4.8). Particles with diameters 500 nm or larger rarely pass into the PCM of RCJ-P and MSC cells. This is consistent with our observation that the PCM prevents bacteria from reaching the cell surface (Figure 4.8a), raising the question of what role the PCM may play in controlling bacterial and viral infections (130).

The PCM microstructure is dramatically altered by increasing the aggrecan content (c_{ACAN}=333 μg/mL). Particles 300 nm and larger are unable to enter the PCM (500 nm was the previous cutoff), a result consistent with characterization of mesothelial cells by Heldin and coworkers (43). The position where 100 nm particles achieve uniform access, e.g. d_{eff}, more than doubles from 3.5 to 8 μm. The sharp gradient of particles in the PCM demonstrates that few particles (>=100 nm) reach the surface (Figure 4.7b). The percentage of 40 nm particles that reach the cell surface appears unaffected by the aggrecan increase (73.2 ± 10.8% vs 70.3 ± 15.4% relative intensity N=20 (27) and N=11(18), where the second number is the number of total measurements made on N cells). However, the percentage of 100 nm particles that reach the surface decreases from 38.8 ± 7.8% to 25.7 ± 6.2% (N=32 (44) and N=14 (24)). Meanwhile, 200 nm diameter particles do not reach the cell surface in native nor aggrecan-treated cells. Their average distance from the cell surface is 3.7 μm in both cases (N=24 (33), N=15 (19)), with low relative intensities of 12.2 ± 1.8% and 17.2 ± 2.6% (N=24(32) and N=12(18)). This blockage may represent the limit to approach the cell surface due to microvilli on the RCJ-P surface, which we estimate extend about ~1-3 μm (103). As with the native cells, the mesh size in the aggrecan-enriched PCM decreases linearly toward the cell surface, but more slowly due to the limited dynamic range in mesh size (Figure 4.8b).

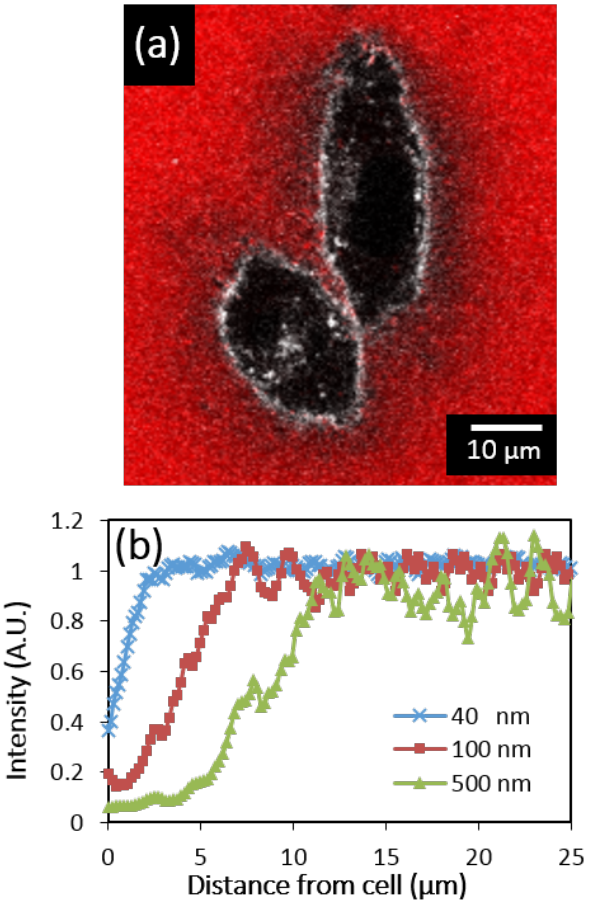

Figure 4.7: (a) Quantitative particle exclusion assay (qPEA) on RCJ-P cells using 100 nm fluorescent beads incubated for 2 hrs with 333 µg/mL aggrecan. The visible gradient in red intensity shows how the average local concentration of beads decreases towards the cell surface. (b) Typical profiles of nanoparticle distributions in RCJ-P cells swollen with 333 µg/mL aggrecan.

From these studies, we conclude that cells apparently have the possibility to control their very local environment and the accessibility of the cell surface by tuning the bottlebrush content in the surface anchored polymer matrix. Although the mesh size of the PCM is large compared to molecules, it may be small enough to affect the transport of exosomes (131–133) and supermolecular assemblies, including bottlebrush molecules themselves. For example, aggrecan is ~300 nm x 80 nm (134)). Increasing bottlebrush density also likely controls interactions with other cells (135) or adhesion to the surrounding extracellular matrix (76, 88, 136).

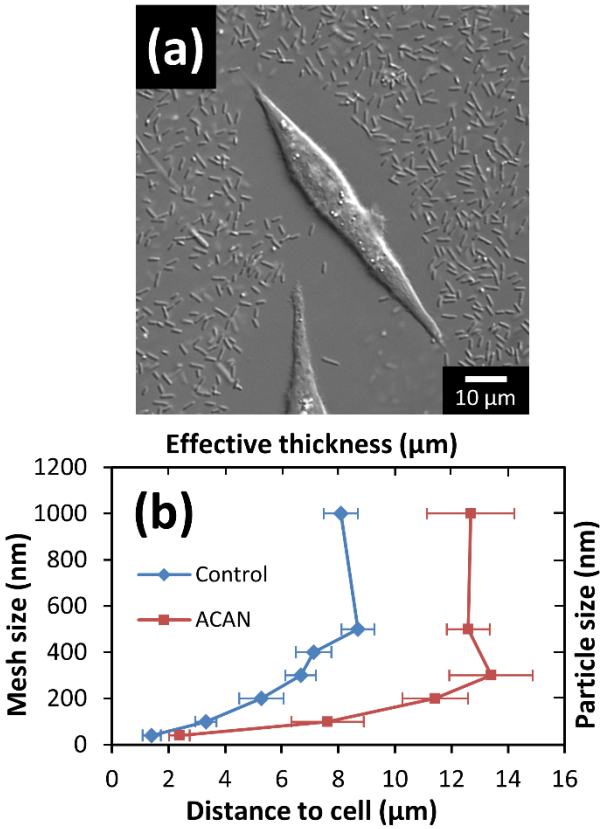

Figure 4.8: (a) Bacteria grown with samples of RCJ-P cells show slowed infection due to the PCM, which acts as a barrier. The size of the bacteria is larger than the threshold mesh size found for native RCJ-P cells using qPEAs (500 nm). (b) Mesh size versus distance to the cell surface: the mesh size decreases towards the surface. For swollen PCMs (c_{ACAN}=333 µg/mL), red curve, the porosity is reduced and it changes more slowly throughout the PCM. Maximum mesh size for native and exogenous aggrecan RCJ-P swollen coats: 500 nm, 300 nm.

Furthermore, the high negative charge densities established by chondroitin sulfate side chains provide another venue for cells to control passage of positively charged molecules to the cell surface, such as growth factors (35). This possibility is explored below.

4.3.5 Increasing bottlebrush concentration drives PCM microstucture toward spatial uniformity

Another way to estimate the mesh size in the PCM is via optical tweezer based measurement (97, 137). These mechanical measurements relate the equilibrium force, $F_{eq}(z)$, in the PCM to an estimate of mesh size ξ (more precisely, correlation length in the polymer matrix), using the relationship, $\xi(z) \propto \left(F_{eq}\right)^{1/3}$, where z is perpendicular distance to the cell surface. This prediction is based on a several assumptions discussed and controlled for in an earlier publication where we developed optical force probe assays for PCM measurements on RCJ-P cells (97).

In this study, we measured the equilibrium force at multiple positions throughout the PCM of RCJ-P cells with and without incubation with aggrecan. The two force curves in Figure 4.9a show little statistical difference in the regions closest to the cell surface (error bars are two standard errors), however at further distances the two are distinct, and even more so when the mesh size is extracted using the theory (Figure 4.9b). We measured the equilibrium force at four different aggrecan concentrations (0, 39, 95, 333 μg/mL). The results show little difference between 0 and 39 μg/mL, but a significant change at 95 μg/mL. At 333 μg/mL, a value where both PEA and exogenous aggrecan experiments show evidence of PCM saturation, the mesh size is nearly constant throughout the PCM, barely changing from ~100 nm to 200 nm (between 3-8 μm). The data is qualitatively consistent with qPEA data, which also shows a linear decrease in mesh size towards the cell surface. Both assays indicate that as the PCM becomes saturated with aggrecan, the openings in the PCM become much smaller, reduced to values below 200 nm. Further, the variation in mesh size decreases, becoming more uniform.

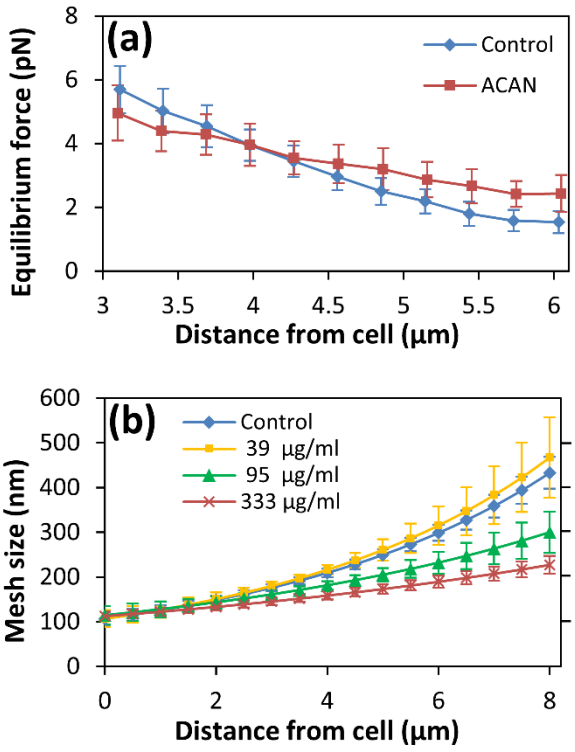

Figure 4.9: (a) Optical tweezer measured equilibrium force in PCM on native and aggrecan-saturated RCJ-P cells (c_{ACAN}=333 µg/mL, 2 hrs). (b) Estimate of PCM porosity (mesh size) using polymer theory and equilibrium force measurement at four different aggrecan concentrations. The mesh size decreases with increasing aggrecan and becomes more uniform. All error bars are 2 standard errors.

4.3.6 Unbound aggrecan diffuses swiftly through the PCM

Next we begin to address the question of how molecular diffusion is affected by the presence of the PCM. Both steric hindrance and electrostatic effects are expected to be relevant, depending on the size and charge of the diffusing molecules. Yet the openings in the aggrecan saturated cell coat are still quite large relative to molecular scales. Indeed, BSA (Figure 4.10) uniformly penetrates the PCM of RCJ-P cells.

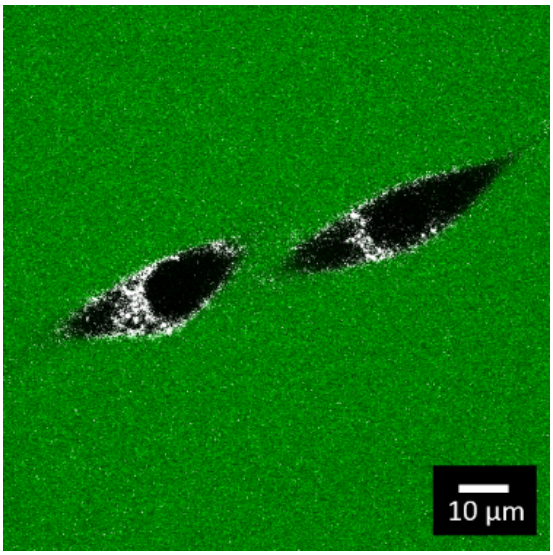

Figure 4.10: Fluorescent BSA (66 kDa, AP-4510-60; SeraCare Life Sciences, Milford, MA) penetrates the PCM and reaches to the cell plasma membrane, which is fluorescently labeled by WGA.

We focus on two classes of physically and biologically relevant molecules, bottlebrush proteoglycans and positively-charged analogs for growth factors. First we examine the diffusion of aggrecan, whose large size is similar to the 200 nm cutoff for penetration into the PCM. Studying how aggrecan diffuses into the PCM is of great interest both in the context of PCM synthesis, as well as PCM and ECM transformation in processes like development (138, 139), wound healing (5), central nervous system injury and repair (140), brain plasticity (141), and disease (142).

We monitor the diffusion of label-free aggrecan into the PCM by quantifying the time-dependent turnover of fluorescently-labeled aggrecan. As in the assays reported in Figure 4.4, RCJ-P cells were incubated for two hours with fluorescent exogenous aggrecan (333 µg/mL). Then the media was gently exchanged with solution containing the same concentration of 'dark' aggrecan, e.g. molecules with no fluorescent labeling. The local average intensity dropped precipitously within the first minute (Figure 4.11a-c) after the exchange. Plotting the integrated

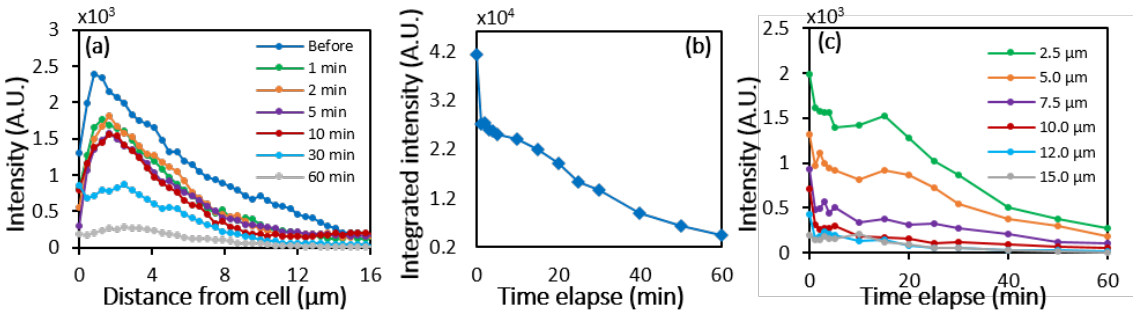

Figure 4.11: Time dependent replacement of PCM bound fluorescent aggrecan with unlabeled aggrecan. (a) Fluorescent profiles of the aggrecan distribution versus time. The first curve marked 'Before' is taken after the fluorescent-aggrecan is removed and replaced with media (no aggrecan). Then the buffer is exchanged with a media containing the same concentration of aggrecan but with no fluorescent label (c_{ACAN}=333 μg/mL). (b) Integrated aggrecan intensity (over entire PCM) versus time. A reproducible drop occurs in the first step and then the aggrecan turnover proceeds linearly. (c) Monitoring aggrecan change at fixed positions in the PCM reveals that after the first time step, only locations 7.5 μm and closer to the cell continue to significantly change.

intensity at each time step shows an initial rapid decrease in intensity of ~23% (N=17, 3 experiments), that is followed by a slower, linear decrease in intensity (Figure 4.11b). Controls involving the exchange of the media with aggrecan-free media showed no significant drop in the aggrecan intensity within the first minute (N=15, 3 experiments), while the sharp drop was reproducible.

In the first minute, the aggrecan turnover occurs uniformly at distances from 2-12 μm (Figure 4.11a, c). Thereafter, at distances 7.5 μm and greater, little apparent change occurs. The majority of the remaining dynamics takes place at the inner, tighter portion of the cell coat, where according to the qPEA assays, the average mesh size is less than 100 nm. Hence we observe that the initial replacement and diffusion of dark-aggrecan into the PCM is rapid and penetrating to the cell surface. However complete replacement of the aggrecan requires more than one hour.

In these experiments, the dark-aggrecan molecules competitively bind with the fluorescently labeled aggrecan. In the presence of high concentrations of dark-aggrecan, the turnover of the fluorescent population is expected to be quite fast. The dissociation constant and off rate of the G1-module of aggrecan is k_d=20 nM (25) and k_{off}= 2.5E-3 s^{-1} (143). The slower turnover in the inner regions of the PCM likely arises from a combination of factors that impact the kinetics. First, in these tighter spaces where the average opening is less than the average dimension of the aggrecan, diffusion inward will be slowed. Like the 100 nm particles that have a reduced concentration in the inner regions, the aggrecan accessibility may also be reduced. Secondly when the fluorescent aggrecan is released, in regions where there is a high concentration of possible binding sites, there is a higher probability that it will rebind, slowing the loss of fluorescence.

The fact that aggrecan is able to diffuse quickly into the aggrecan-enriched PCM is significant, considering its reported extended size is on the order of ~300 x 80nm or larger. In solution, aggrecan forms a globule, which according to dynamic light scattering has a hydrodynamic radius of ~200 nm (144). Yet, we have shown that 200nm particles are mostly localized to the edge of the PCM at ~11.5 μm from the cell surface in aggrecan-treated cells (333 μg/mL) and significantly hindered from entering the PCM of the native RCJ-P cells at distances closer than 6 μm to the cell surface. It is possible that the asymmetry of aggrecan as well as its flexible, globular properties enables freer passage through the cell coat.

4.3.7 Electrostatic sequestration of positively charged ~20 kDa molecules in the PCM

In this final section, we study the interaction of small positively charged molecules with the high-negatively charged landscape generated by the chondroitin sulfate-rich PCM. Looking for visual evidence of spatial localization of the positive molecules in the PCM is directly relevant to

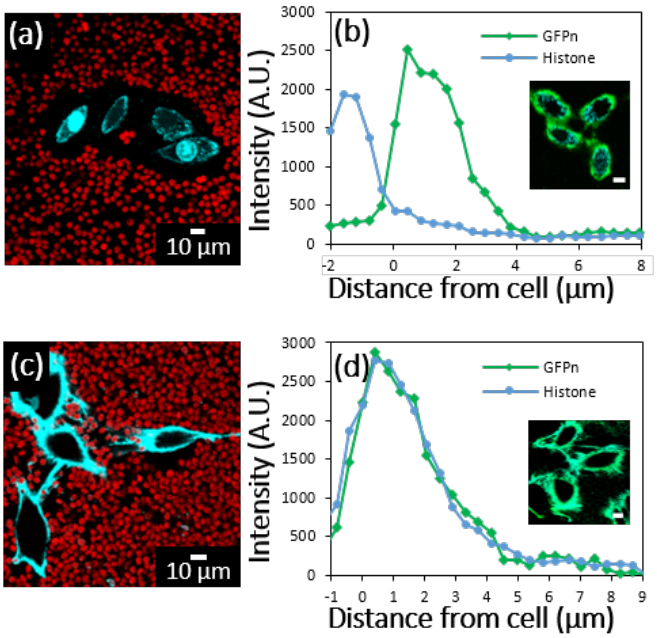

Figure 4.12: (a) Fluorescent histones (cyan) are barely detectable within the PCM of native RCJ-P cells (c_H=232 µg/mL for 20 mins). (b) The majority of histones bind very close to the surface and are largely injested by the cells. Labeling of the HA in the PCM with GFPn confirms as expected the PCM extends beyond the region where histones bind. (c) In aggrecan-enriched PCMs (c_{ACAN}=333 µg/mL), the histones bind strongly to the PCM, whose presence is confirmed by PEA (c_H=232 µg/mL for 20 mins). The PCM is thinner than histone-free measurements, indicating a collapse driven by crosslinking (see Figures 4.13, 4.14). (d) GFP and histones co-localize in the aggrecan-enriched PCM.

questions regarding the passage of growth factors, cytokines and chemokines through hyaluronan-aggregate rich PCM and ECM (35). Small molecules should not be sterically hindered by the PCM since it still maintains >100nm openings even during bottlebrush saturation. Yet, there is evidence that PCM can sequester molecules via non-specific and specific binding to the sulfated chains in bottlebrush (35). Here we focus on the possible role of electrostatic interactions.

For this exploratory study, we use an inexpensive surrogate for growth factors, histone proteins, which have similar charge and size to growth factors (145). Figure 8a shows an image of RCJ-P cells incubated with fluorescently labeled histones (c_H=232 µg/mL, 20 mins). Very little of the fluorescent histone (Figure 4.12a) is visible outside of the cell. For most cells, no labeling

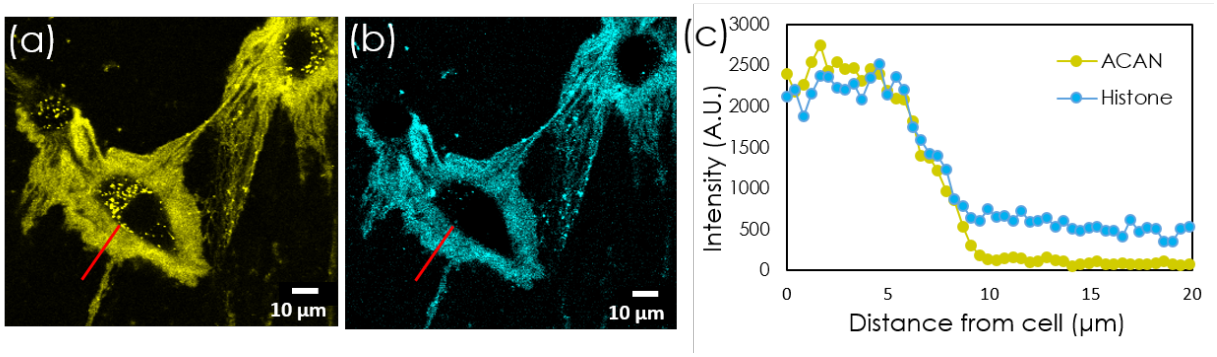

Figure 4.13: Histones bind to exogenous aggrecan in the cell coat of RCJ-P cells. Measurement of the fluorescently labeled aggrecan and histones shows co-localization of the molecules. (a) Fluorescent image of aggrecan-swollen PCM (333 µg/mL, 2 hours, yellow) with (b) histones added (232 µg/mL for one hour, light blue). (c) Profiles of exog-ACAN and histones in the PCM. The zero is arbitrary and does not indicate the cell surface. Histones were left in solution when taking image, hence the slightly higher background. The binding of the histones reduces the usually extensive PCM via histone-mediated crosslinking of the aggrecans.

outside the cell was visible, while uptake onto the plasma membrane and nucleus was significant. To distinguish histones, which are bound close to the cell surface versus those taken inside of the cell, we fluorescently labeled the PCM's hyaluronan using GFPn (Figure 4.12b). The majority of the histone appears inside of the cell or close to cell surface. A very small signal appears in the PCM region from approximately ~2-6 µm.

We repeated the same experiment in aggrecan-enhanced PCMs (333 µg/mL, 2 hrs) followed by exposure to histones (c_H=232 µg/mL, 20 mins). Strong binding between the exogenous aggrecan and histone is reflected by the brightly labeled PCM (Figure 4.12c). Far less of the histones are taken up by the cells, showing that an aggrecan-rich PCM sequesters positively charged molecules and reduces their uptake by the cell.

There is a direct correlation between the fluorescent aggrecan, the HA (Figure 4.12d), and the histone distributions (Figure 4.13) in aggrecan-enriched samples (333 µg/mL). Most samples showed evidence of HA crosslinking and resultant PCM shrinkage in the presence of histones (Figure 4.12c, Figure 4.13). Analysis of aggrecan fluorescence versus distance to the cell

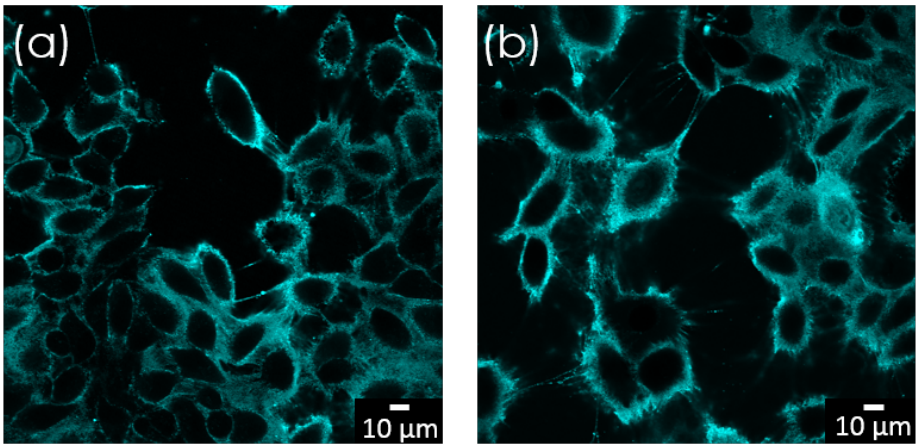

Figure 4.14: Evidence for PCM crosslinking by histone proteins, whose multiple positive charges could simultaneously bind multiple aggrecan molecules, crosslinking the PCM. This leads to the formation of fibers and bundles around and between the cells. In both images, the samples where incubated with aggrecan (333 µg/mL) for two hours, followed by replacing with media containing fluorescent histones (232 µg/mL).

(Figure 4.4b vs Figure 4.12d and Figure 4.13) suggests that the PCM is collapsed from an average is reduced from ~12 µm to ~6 µm. Evidently the positively charged histones can act as crosslinkers between the aggrecan molecules (Figure 4.14). Similar effects have been shown by crosslinkers in a PCM model systems (146–148).

Interestingly, in control experiments to further demonstrate that the histones localize to the chondroitin sulfate side chains on aggrecan, we attempted to remove the histones by their degradation with chondroitinase ABC (ChABC). Instead, we found that histone-enriched PCMs could no longer be fully digested (see Figure 4.15). This result confirms that the histones bind to the chondroitin sulfate chains so strongly that they block the enzymatic activity of ChABC. Repeating these experiments on the native RCJ-P cells incubated with histones showed similar results: the PCM remained intact despite minimal visual evidence of histone sequestration (Figure 4.16).

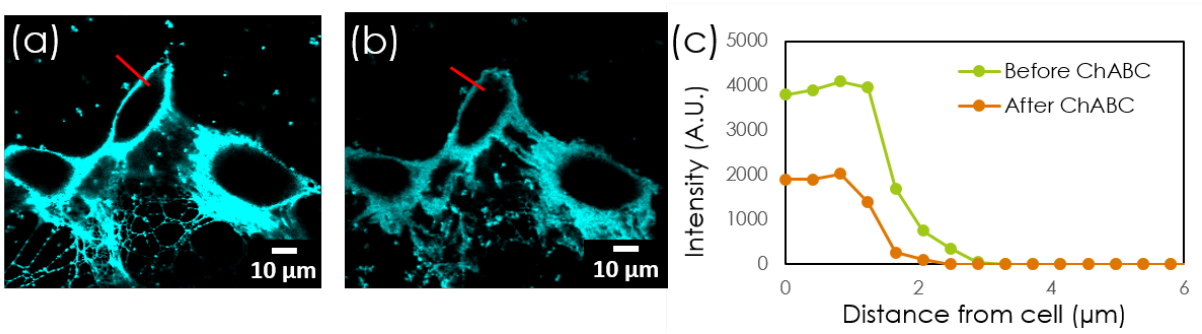

Figure 4.15: (a) Fluorescent histone treatment of aggrecan-incubated RCJ-P cells shows significant visible labeling of the PCM. (c_{ACAN}=333 µg/mL, 2 hours; c_H=232 µg/mL, 20 minutes) (b) The histones partially block digestion of the PCM by the enzyme ChABC (0.27 unit/mL) for at least 30 minutes. Without histones, the PCM is removed in less than five minutes. (c) Profile of the histone distribution perpendicular to the cell surface before and after ChABC treatment. There is a decrease in the histone intensity and slight degradation of the cross-linked fibers between the cells.

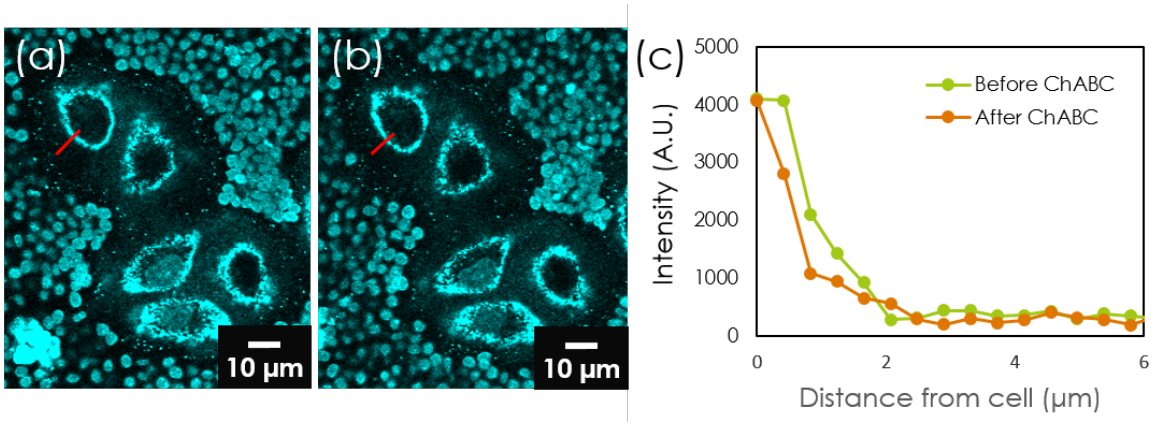

Figure 4.16: (a) Fluorescent histone treatment of RCJ-P cells does not show significant visible labeling of the PCM; however the PCM remains, as shown by PEA. (232 ŧ g/mL, 20 minutes) (b) Digestion of the PCM by the enzyme ChABC (0.27 unit/mL, 20 minutes) is blocked by the presence of the histones. (c) Profile of the histone distribution perpendicular to the cell surface before and after ChABC treatment. There is little change in the intensity.

This is compelling evidence that the chondroitin sulfates on native endogenous aggrecan and exogenous aggrecan in the PCM sequester positively charged histones, and at high bottlebrush concentrations, significant reduction in histone uptake is a consequence.

4.4 Conclusions and Outlook

These studies provide quantitative illustrations of how changes in bottlebrush proteoglycan concentration in the PCM can affect the transport of nanoparticles to the cell surface as well as the sequestration of positively charged molecules. Diffusion of the bottlebrushes themselves still occurs through saturated pericellular matrix despite the dimensions of the molecule and its negative charge. Further, several experiments independently imply that the native PCM of RCJ-P and MSC cells *in vitro* are sparsely populated by endogenous bottlebrushes.

The sparse population of bottlebrushes points to the possibility for cells to use surface-tethered proteoglycans to monitor native cell surface accessibility or to concentrate and sequester biomolecules like growth factors. Mechanics could be altered this way as well. For the cell types studied here, a special regime exists where the PCM appears fully stretched, but where the porosity and molecular interactions can be tuned significantly by varying the solution concentration between 180-333 μg/mL.

Although these studies do not recapitulate *in vivo* conditions, where the PCM is likely compressed by surrounding tissue, they provide compelling data that modulation of bottlebrush proteoglycan distribution in the PCM and indeed in the ECM can affect tissues physical properties dramatically.

There are many important directions to pursue in future work. Immediately relevant are follow up studies examining growth factor sequestration to the PCM, investigation of its release,

and its possible effects on cell. For example, looking at whether BMP-2 is sequestered and concentrated to high enough concentrations to drive differentiation of stem cells would be an excellent example of how PCM can be utilized by cells as a molecular reservoir. Further, given the observation that PCM can significantly reduce the molecular uptake of histone proteins suggests the need to investigate possible filtration effects that might eliminate harmful molecules and/or interfere with proper cell function by removing necessary molecules. More generally, our studies demonstrate how important it is for researchers to be cognizant of possible PCM effects in studies of drug delivery vehicles, exosomes or any study looking at size-dependent endocytosis or phagocytosis. In the longer term, the ability of the PCM to dynamically transform is relevant for understanding cell-cell and cell-ECM interactions, for example in migration and proliferation. Finally, interesting strategies for the bioengineering of scaffolds or tissues could be taken from the studies here. For example, generic seeder cells that produce PCM could be planted in matrices and utilized to control local production and concentration of growth factors. To conclude, the pericellular matrix is often broadly neglected; yet its presence adds another dimension of control and tunability for cells that likely plays an elegant role in cell control and integration.

Chapter 5

Hyaluronan Mediated Cell Adhesion

5.1 Overview

Hyaluronan polymer has been studied in its connection with cell adhesion events more and more in recent years. It has been shown to impact the migration and proliferation of the cells, impede cell connections in synaptogenesis, impact cancer cell malignancy, and play a critical role in cell rearrangements during embryogenesis. Moreover, many cancer-focused studies have focused on the signaling role that HA plays (mostly in oligosaccharide form) via the transmembrane receptor CD44, which transmits a chemical signal to the cell interior. However, inspired by the unusual HA distribution on migrating cells, a more mechanical view of the HA's potential impact on adhesion events also pervades the literature. It has been speculated that the accumulation of HA matrix at the trailing edge of a migrating cell reduces the adhesion strength at that end so the cell can detach from the substrate easier. At the same time, less HA matrix at the leading front of the cell entails a stronger adhesion to the substrate and anchor that part of the cell stronger than the rear of the cell. Cell utilizes this gradient of adhesion strength to migrate. It is also speculated that HA modifies the adhesion between cells during proliferation since proliferating cells have been documented to have more HA production than during other cell cycles. During the dividing stage, the cell might produce a significant amount of HA that again might weaken the adhesion between parent and daughter cell, and thus separate them apart. With all these speculations, we incorporate various techniques to elucidate the effect of HA in cell adhesion.

This chapter summarizes our investigation of the role that cell-surface anchored HA plays in the mechanics of cell adhesion. The approach is to combine the results from a detailed analysis

of cell adhesion strength measurements using a hydrodynamic assay, the state of focal adhesions, hyaluronan patches under the cell, and their spatial correlation and impact on the contact area of the plasma membrane with the substrate. A series of self-consistency checks and controls were performed to check that the HA impact is directly mechanical rather than indirectly impacting the state of the focal adhesions or that the enzymatic treatments used adversely change adhesion strength. Integrating the outcome of these experiments, we provide the most thorough study and compelling evidence to support the hypothesis that hyaluronan mechanically mediate cell adhesion through mechanical repulsion.

5.2 Materials and Methods

5.2.1 Cell culture and sample preparation

See section 3.2.1

5.2.2 Glass coverslip coating

During spinning disk assay, round cover glass (Neuvitro, Vancouver, WA: GG-25-1.5) is used, and 25x25 mm #1.5 glass coverslip (VWR: 48366-249) is used for all other experiments.

All glass coverslips are first cleaned by sonicating the coverslips first with water for 5 minutes and then with 100% ethanol for another 5 minutes. They are then washed with PBS (VWR: 97062-732) twice to get rid of residual ethanol. The coverslips are put on top of 100 µl of protein solutions on a piece of parafilm inside biosafety cabinets for 1 hour to absorb proteins onto the coverslips. Fibronectin (Human, Life Technology: 33016015) is diluted with PBS to the concentration of 50 µg/ml and collagen (Type I, Rat, Life Technology: A1048301) is diluted in 20 mM acetic acid to the concentration of 33 µg/ml. The collagen incubation is kept in the dark. After protein incubation, coverslips are washed by dipping into PBS slowly and then incubated with 1

mg/ml BSA for 30 minutes by the same method. The coverslips are ready to use after washing again with PBS. The protein-coated coverslips can be kept in 4°C fridge with PBS for 3 days if not used immediately.

5.2.3 GFPn production and use

See section 3.2.3

5.2.4 Transfection of fluorescent paxillin

The mCherry-paxillin plasmid is a gift from T. Barker (Georgia Tech, Atlanta, US) and GPF-paxillin plasmid is a gift from K. Salaita (Emory University, Atlanta, US).

The cell density of 80% confluency is optimal for transfection in 24 wells plate (Corning: 3524). The optimal seeding numbers are $1.5x10^4$ cells for RCJ-P and Hs578T, and $4\ x10^4$ cells for PC3 in the 1.9 cm^2 cell growth area in the plate for 16-18 hours.

Lipofectamine LTX DNA transfection reagent (ThermoFisher: A12621) is used for fluorescent paxillin transfection following the product protocol. First dissolve 0.5-1 μg of DNA into 100 μl Opti-MEM® Medium with 0.5-1 μl of PLUS™ Reagent for 5 minutes. Afterwards, 1-1.5 μl of Lipofectamine® LTX Reagent is added to the solution for 25 minutes before adding the solution into the cell media in wells. To seed the cells into Teflon rings for imaging, the DNA reagent solution is sucked out and temporary put away after DNA incubation of 18-20 hours. Incubation with 500 μl of trypsin is used to detach the cells from the 24 wells plate. After counting, the normal density of cells is plated into the Teflon rings and the DNA reagent solution is added back to the cells. The cells are seeded for another 18-20 hours before imaging.

5.2.5 Reflection Interference Contrast Microscopy

The ventral topography of cells is monitored by Reflection Interference Contrast Microscopy (RICM). Polarized light from epi-illumination is used to image the cells. Constructive and destructive interference between light reflected off the cell and the cover glass results in light and dark fringes. The shade of the fringes depends on the distance between the cell and the substrate (149). Although the RICM image is complicated by the presence of additional interfaces and the use of incoherent light, the quantitative trends remain the same. Under RICM, locations where cell made direct contact with the substrate appear as dark patches on an otherwise grey background.

Cells seeded in Teflon rings are first imaged with RICM, the same cells are then repeatedly imaged every 5 minutes for over an hour when incubated with bacterial hyaluronidase. Ventral topographies are compare on the same cell for the first 30 minutes of enzyme incubation.

For a quantitative analysis of the RICM images, pixel intensity under the cell are gathered and binned into histogram using ImageJ. Freehand selection tool is first used to highlight the outline of the cell, and the histogram function in the analysis section analyzes the pixel intensity and displays the statistics. The standard deviation and average intensity of the intensity histogram distribution are used to compare the states of the cells' ventral topography.

5.2.6 Spinning disk apparatus

The spinning disk apparatus is used to measure cell adhesion strength. The setup consists of a fluid-filled cylinder in which a disk containing the sample spins. When high enough hydrodynamic shear applied to the cells, they detach from the substrate. The system applies a linear range of forces, correlated with the distance to center of rotation, to the cells while maintaining a constant and uniform chemical environment at the surface (150).

The glass slide with cells is attached to the spinning disk device by creating vacuum on it by design. Submerging the apparatus into chamber filled by PBS with 2 mM of Dexrose (Sigma G7021), the sample is spun for 5 minutes at room temperature. After the spin, the cells are fixed with 4% ethanol free formaldehyde. The samples are ready for imaging after mounting the cover glasses onto microscope slides with ProLong Diamond with DAPI dye at room temperature for more than 6 hours.

5.2.7 Adhesion strength measurement

On the slides, 61 fields (60-100 cells/field before spinning) with various radial distance to the center are imaged using a Nikon TE300 equipped with a Ludl motorized stage, Spot-RT camera, and Image-Pro analysis system. Comparison of the adhered cells left on surface to the population at the center produces the fraction of adherent cell at different positions. The radial distance of the locations can be converted to the shear stress on the cells with the equation $\tau = 0.8r * \sqrt{\rho * \mu * \omega^3}$, where ρ, μ, ω are the fluid density, fluid viscosity and angular velocity of the disk respectively. The fraction of cells remain on the surface after spinning is then fit to a sigmoidal curve $f = \frac{f_0}{1+\exp\left[b(\tau-\tau_{50})\right]}$, where f and τ are the experimental adherent cell fraction and disk surface shear stress and f_0, b, and τ_{50} are the fitting zero-stress cell fraction, decay slope and inflection point (150, 151). The adhesion strength of the cell is defined to be the shear stress for 50% detachment.

For comparison of different state of HA matrix, the percent change of adhesion strength is the fraction of the change in adhesion strength to the control cells. The N reported for spinning disk experiments is of the number of individual samples done, which contains more than thousands of cells. Due to the adhesion strength of control cells drifting as discussed in section

5.4.5, all the conditions of HA matrix state are only compared with the control cell samples done on the same day.

5.2.8 Enzyme treatment digesting PCM

There are various classes of hyaluronidase (HAdase), or Hyals, based on their mechanism of action (24). Two different classes of HAdase, from bacteria and bovine, were used on the cells in this experiment. Both of the enzymes degrade HA predominantly. They also have limited ability to digest Chondroitin (Ch) or Chondroitin Sulfate (CS) but at a much lower rate (24). There is a common misconception that bacterial HAdase only targets HA, but it has been proven not that case. It still degrades Ch and CS but at an even lower rate than the other HAdase type (152). The structures and action modes of the two Hyal types are different. The vertebrate Hyals degrade HA through a non-processive endolytic process, which generates a range of HA oligomers with a wide spectrum of size-dependent biological activities. On the other hand, many bacterial Hyals appear to degrade HA through initial non-processive endolytic bites for high molecular weight HA followed by exolytic processive degradation on the smaller chains. For the degradation of Ch and ChS, only the non-processive endolytic method is employed. The process produces the same size unsaturated Ch/ChS-disaccharides (24).

The enzymes are dissolved in PBS and then directly added to cell sample to achieve final concentration of 0.08 mg/ml for bovine HAdase (type I-S, Sigma: H3506) and 7.5 un/ml for bacterial HAdase (Hyaluronate lyase from Streptomyces hyal, Sigma: H1136). Enzyme is left in the cell culture media for 30 minutes to digest the PCM around cells. Interfacial HA matrix labeled with GFPn showed a decrease of more than 80% in intensity after HAdase incubation showing depletion of the HA matrix.

5.2.9 Myosin II inhibition

Blebbistatin (Sigma: B0560) is reconstituted in DMSO following the manufacturer's instruction. It binds to ADP-Pi on myosin and locks myosin in ADP-Pi phase and stops motor activity. Cells are seeded onto cover glasses for 18-20 hours before 20 μM of blebbistatin is added into cell media for 30 minutes according to protocols for myosin II inhibition (153–155).

RCJ-P cells' phenotype changed within 30 mins of incubation with blebbistatin, and began to reduce contact area to the substrate. During the comparison experiment, blebbistatin was added in with bacterial HAdase to the cells for 30 minutes, and the adhesion strength was compared with that of the cells just incubated with blebbistatin for 30 minutes.

5.2.10 HA synthase suppression

4-methylumbelliferone (4-MU) blocks HA biosynthesis by its ability to sequester cytosolic UDP-glucuronic acid (UDP-GlcUA) (156). Additionally, 4-MU effects a pronounced reduction of HA synthase 2 (HAS2) transcription but by mechanisms that are currently unknown (79, 156, 157).

After suspension of the cells by trypsin, the cells were incubated with 2 mM of 4-MU for 4 hours. The cells attached to the substrate during that time. They were not as spread out as control cells but formed tethers at the cell edges (still look healthy). Use GFPn and see no significant amount of HA are around nor under the cells in 6 hours of incubation

For the comparison experiment, both sets of samples have their 4-MU containing media aspirated out, washed with 2 mL of sterile PBS, and replaced with fresh complete culturing media with and without 2 mM of 4-MU. GFPn was used to visualize and found HA around and under the cells within 1 hour in the samples without 4-MU and none in samples with 4-MU. Adhesion strength measurements were done on the cells 2 hours after media replacement.

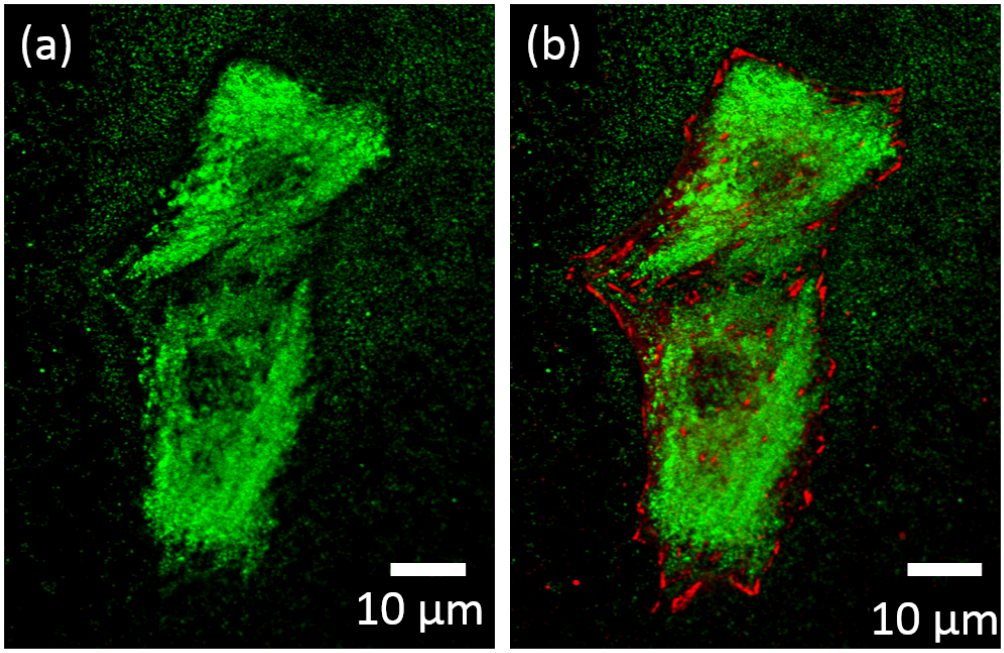

Fig. 5.1: (a) HA matrix under fixed RCJ-P (green). (b) Spatial anti-correlation between HA matrix (green) and vinculin FA (red) under fixed RCJ-P cells.

5.3 Results

5.3.1 Hyaluronan is organized in patches at the cell-substrate interface

We previously demonstrated that neurocan-link-protein attached to GFP (GFPn) specifically labels hyaluronan on living cells, and used it to characterize the pericellular matrix (see Ch. 3 and 4). Above the glass substrate and surrounding the cells, there is a continuous distribution of HA that comprises the PCM on several cell types including chondrocytes (RCJ-P), prostate cancer cells (PC3), and breast cancer cells (Hs578T). At the interface of the cell and the substrate, not surprisingly, the structure is different because it coexists with adhesive plaques. Confocal microscopy reveals a patch-like HA distribution for all three cell lines (see Figures 5.1, 5.4, 5.5). After adding bacterial or bovine hyaluronidase (HAdase) into the cell culture solution, the HA patches under the cells consistently disappear within 15 minutes. Control experiments

verified that the loss of fluorescence does not arise from photo-bleaching of the GFP, e.g. the GFPn labeled cells were imaged at the same frame rate in the same conditions without exposure to HAdase and the fluorescence signal remained with minimal bleaching.

5.3.2 Spatial anti-correlation of focal adhesions and HA patches

Previous studies have demonstrated the spatial segregation of FAs and chondroitin sulfate, where it was implied the CS is that found on the chondroitin sulfate rich bottlebrush proteoglycans (CSPG) associated with HA (36). Immunofluorescence studies also showed that HA and HA receptors co-localize with versican, a member in the CSPG family (37), and the HA receptors have a negative correlation with one of the focal adhesion proteins, paxillin, at the cell-substrate interface (39). These results hinted the ventral HA patches could be separated by FAs. In preparation to consider how the HA patches might coordinate with focal adhesions in mediating the mechanics of cell adhesion, the spatial localization of HA versus FA was investigated on the cell lines studied in our lab. The results are summarized below.

We start with RCJ-P cells because they are the model cell line that the Curtis lab has optimized all of its biophysical assays on and it is a system we know well. The other two cell types reported here are both cancer cell lines, chosen in part because HA expression and presence is correlated with the onset on many types of cancer. Furthermore, the prostrate PC3 cells were selected because of the classic papers by Ricciardelli reporting PCM-dependent cell migration (41). The breast cancer cell line, Hs578T, was chosen because it is a highly malignant, highly migratory phenotype that produces very large amounts of hyaluronan (80). It is also a cell line studied by one of our collaborators, Dr. Paraskevi Heldin, who ultimately will work with us to modify HA synthase and CD44 expression to explore how adhesion depends on surface-bound HA.

5.3.2.1 RCJ-P cells

RCJ-P cell binding to untreated glass produces elongated, distinct FAs (see Figure 5.2a). We were able to visualize these FAs on living RCJP cells by transfecting them with GFP paxillin, which localizes at the focal adhesion complex and is widely used as a FA marker. After transfection, the efficiency was about 20% of the cells expressing the GFP-paxillin, which was typical according to our collaborator Prof. Salaita from Emory University, who graciously provided the GFP-paxillin vector for transfection. There was no change in phenotype of the cells that expressed GFP-paxillin. Both the fluorescent paxillin transfection and vinculin immunostaining showed, similar to fibroblasts and other cells bound to glass, the majority of the FAs are located at the edge of the cells, while the ones in the middle of the cell are smaller and less elongated (N>30 from various methods).

In order to simultaneously visualize HA and FAs, we originally tried to label FAs with a non-green fluorescent label via transfection, e.g. mCherry paxillin (gift of Dr. Tom Barker's lab). Unfortunately, despite efforts at optimization, the mCherry paxillin transfection protocol did not label the FA well on the RCJ-P cells. The transfection success rate of mCherry paxillin was lower than the 20% transfection rate with the GPF paxillin. Even in the few cells expressing mCherry paxillin, the FA labeling was dim and difficult to discern because the background fluorescence in the cell was high (see Figure 5.2b).

Ultimately, we resorted to immunofluorescent staining of fixed RCJ-P cells using a red vinculin antibody. This is less optimal because it is known that fixation often removes the PCM

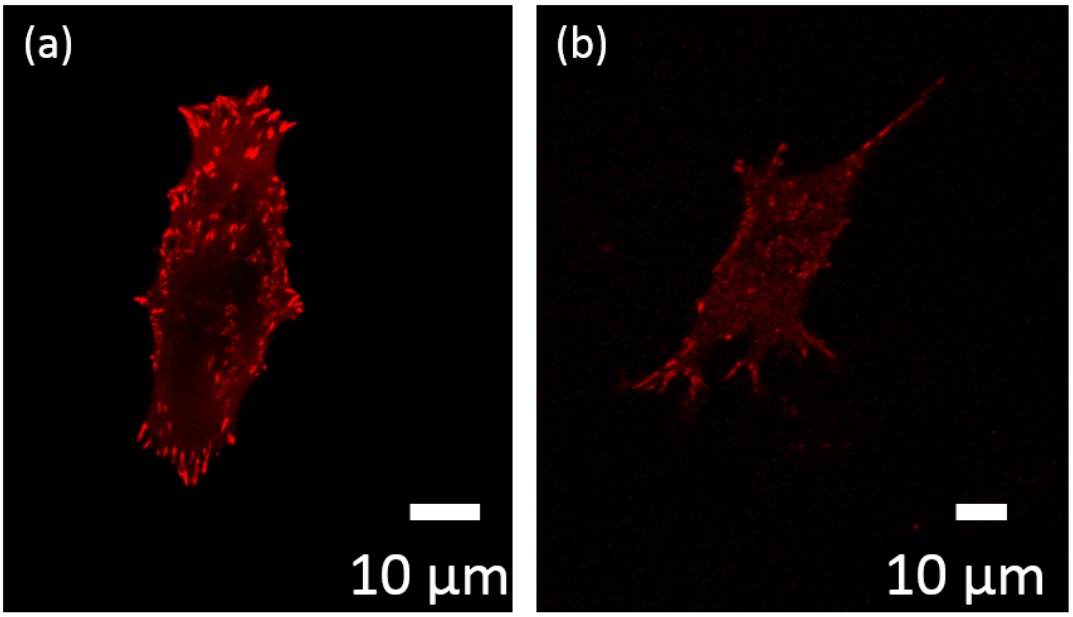

Figure 5.2: Live RCJ-P cells (a) GFP-paxillin shows elongated FA concentrated at edge of cell. (b) mCherry-paxiilin also label FA but not as clear as GFP-paxillin.

due to hydration issues. However, we found that the HA at the interface remained (to what extent is less clear, although it appears to be similar in structure as on living cells as shown by comparing directly – data not shown). Figure 5.1 shows a typical image of the outcome of this fixation procedure. The interfacial hyaluronan and the FAs are in distinct regions, separated for the most part, especially when the FAs are large as on the edges of the cell. In their related Nature paper in 2014, (mostly not focused on hyaluronan however), Paszek and Weaver (88) showed strikingly similar images in their supplementary material.

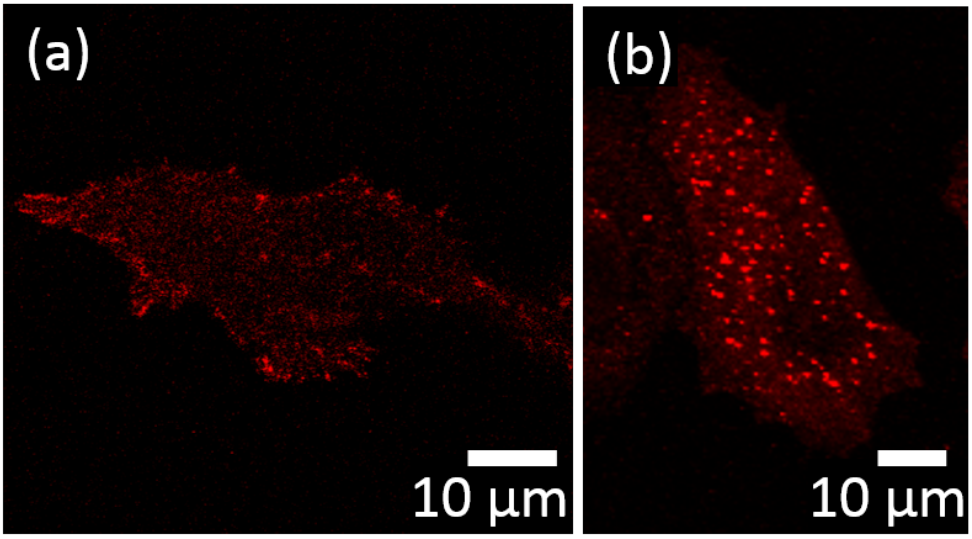

Figure 5.3: (a) GFP-paxillin on live PC3 cells shows FA more punctate than RCJ-P. (b) The vinculin antibody labels FA on fixed PC3 cells, also revealing showing punctate FAs (N>30).

5.3.2.2 PC3 prostate cancer cells

Our studies show that the PC3 prostate cancer cell line produces far less distinctive adhesive plaques than the RCJ-P cells. Indeed, labeling via transfection with GFP-paxillin (Figure 5.3a) or alternatively, immunofluorescence with vinculin antibody (Figure 5.3b) revealed punctate focal complexes rather than the mature FAs displayed by RCJP cells. Also, comparing the HA patches under cell, labeled by GFPn, on PC3 (Figure 5.4) and on RCJ-P (Figure 5.1) showed the separating spaces between the HA patches on the PC3 cells are not as elongated as the ones under RCJ-P cells. Also there are more HA excluded zones under PC3 than RCJ-P cells. (N=20)

Although only shown one image here, fluorescent vinculin was imaged on more than 30 fixed PC3 cells. However, the transfection of fluorescent paxillin, GFP or mCherry, did not yield too much success, so the imaging of transfected paxillin on PC3 was done on about 10 cells.

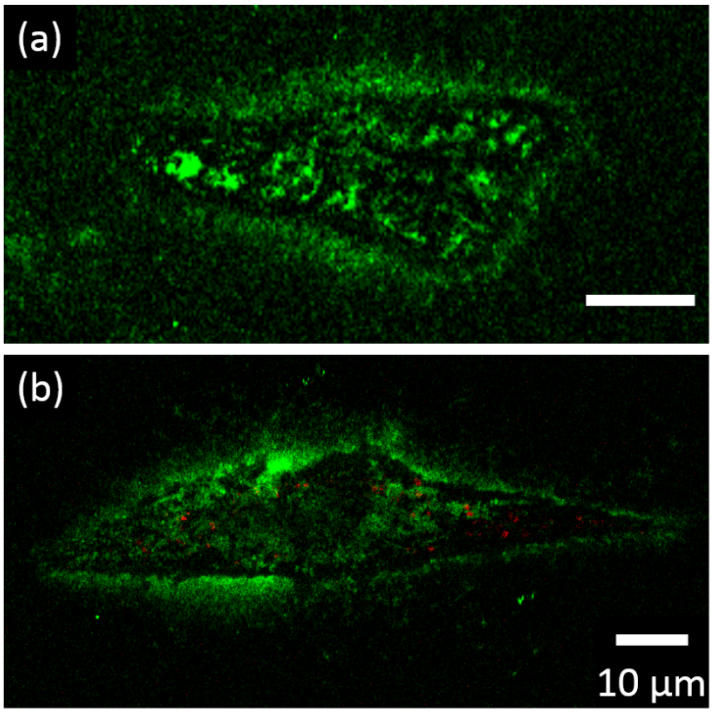

Figure 5.4: Confocal image under live PC3 cells (a) GFPn labeling HA matrix. (b) GFPn labeling HA matrix (green) and mCherry paxillin showing FA (red).

5.3.2.3 Hs578T breast cancer cells

The breast cancer cell line Hs578T was transfected with mCherry paxillin so that FAs and hyaluronan could be visualized simultaneously. The results were impressive, with a typical image shown in Figure 5.5. The same spatial separation apparent in the RCJ-P cells is seen for the Hs578T cells as well. Clear anti-correlation of the green interfacial HA and the extended FAs is apparent. Different from the other cell lines, the HA appears to gather closer to the edges of the cell rather than uniformly throughout it (N=30).

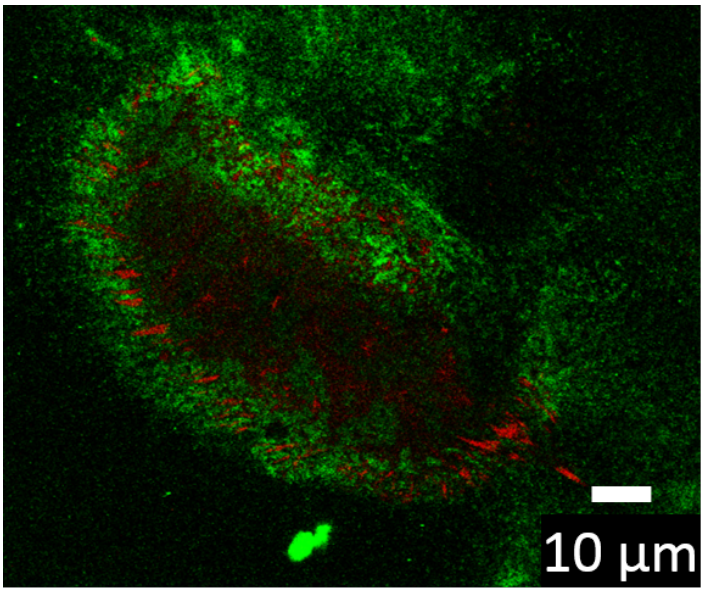

Figure 5.5: mCherry-paxillin (red) and GFPn (green) shows spatial anti-correlation between FA and HA patches under cells. Imaged on live Hs578T breast cancer cell.

5.3.3 Topographical variations at the cell-interface decrease after hyaluronan removal

To examine the impact of HA on the topography of the cell-substrate interface, we employed reflection interference contrast microscopy (RICM) (149, 158), also sometimes called interferometric reflection microscopy (IRM) (159). This interferometric technique provides qualitative (and quantitative if desired) information regarding variations in height between the cell and the substrate. Variations in intensity correspond to variations in topography, where typically darker shades of grey reflect a portion of the cell close to the substrate and brighter regions indicate a portion of the cell further. For example, FAs tend to appear as black strips in RICM, and comparison of RICM with immunofluorescent labeling of the FAs shows overlap (Figure 5.6). The inherent interferometric nature of the technique means that the scale repeats itself in shades of grey for distances greater than $\lambda/4$, or ~135 nm. For this reason and other technical difficulties,

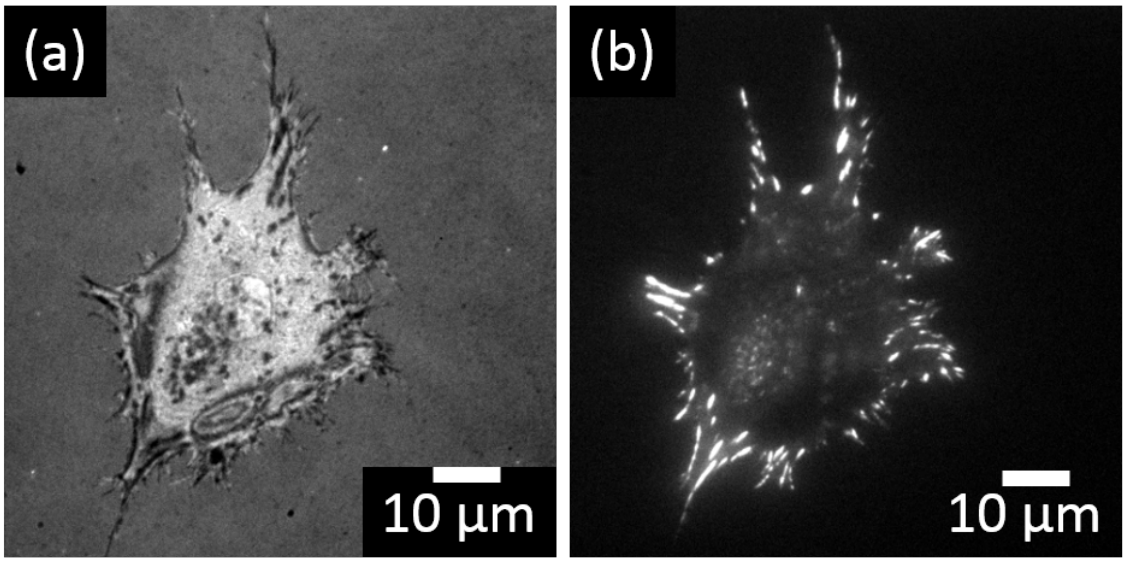

Figure 5.6: (a) RICM image on live RCJ-P cell and (b) GFP-paxillin labelling of the FA on the same cell. The dark patches in the RICM corresponds to the FAs.

we do not provide absolute information regarding cell topography at the interface but just relative changes.

5.3.3.1 Topography of RCJ-P cell plasma membrane

This interferometric approach was used in our studies to compare the cell membrane roughness at the interface (amount of variation in topography, e.g. intensity) before and after enzyme degradation of hyaluronan. The different shades of grey in the RICM images reflects various distances of the cell membrane to the substrate. When imaging the RCJ-P cells with RICM, a high degree of variation in intensity was visible, for example in Figures 5.6 and 5.7a. A given configuration remained relatively stable for two plus hours during imaging (e.g. the average intensity variations).

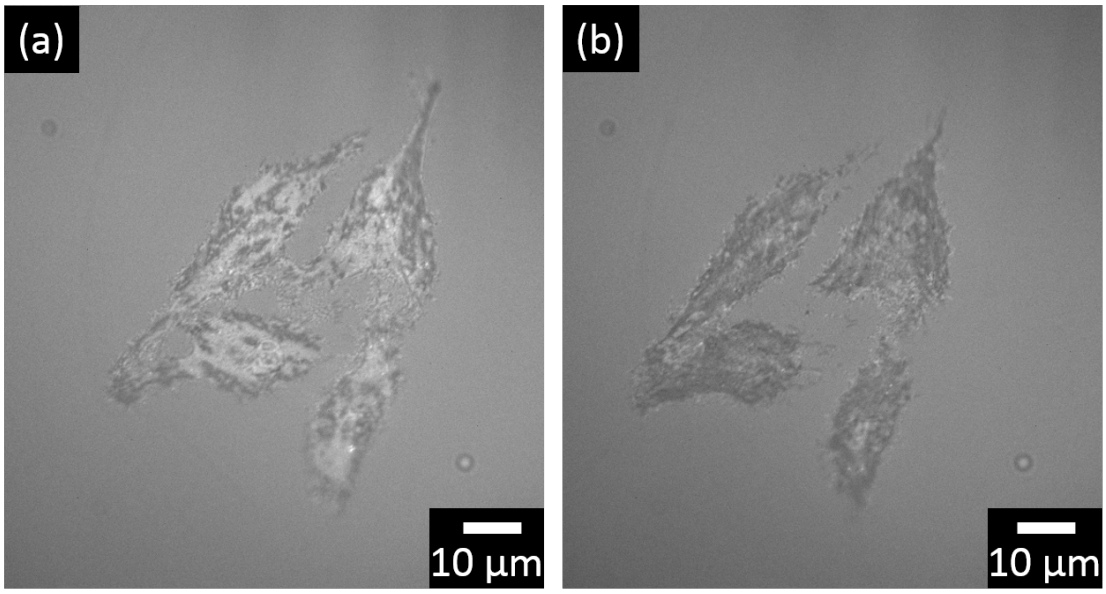

Figure 5.7: RICM images of live RCJ-P cells showing the distance between cell and substrate (a) before and (b) after 20 minutes bovine HAdase treatment.

Next, the same cells were exposed to bovine HAdase (30 min) while monitoring with RICM. Movies of RCJP cells showed the intensity variations reducing over that time period and becoming nearly uniform (see Figure 5.7) and much darker, indicating that the cell membrane approached the substrate and became significantly less ruffled. Repeating the experiment and just analyzing before and after images of the same cells in RICM, it was estimated that the intensity variations diminished significantly in 95/100 cells examined. To quantify the change in the ventral topography of the cells after enzyme treatment, the pixel intensities under one cell are sorted and analyzed by the image process program, imageJ. The standard deviation of the pixel intensity under one cell shows the roughness of the topography. When there are more rises and falls under the cell, there will be a wider range of bright and dark fringes in the RICM images, and therefore yield a larger standard deviation of the pixel distribution (Figure 5.8). Quantitative analysis of the RICM images of the standard deviation of the pixel intensity for each cell before and after bovine

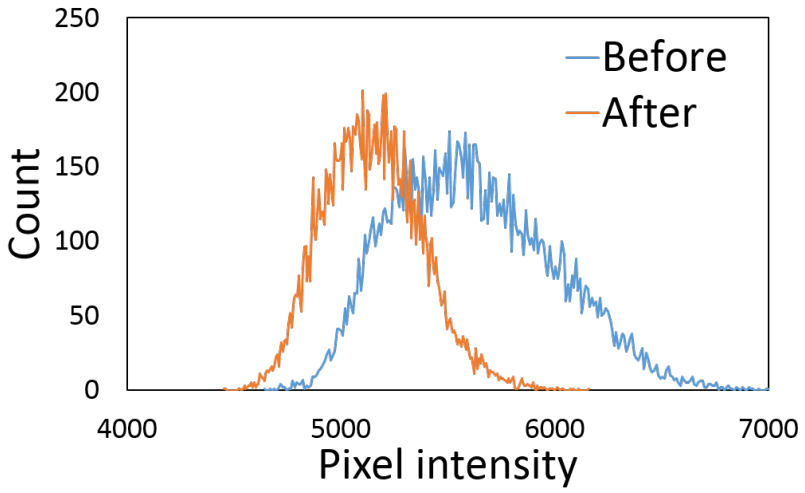

Figure 5.8 Pixel intensity histogram under single cell before and after bovine HAdase treatment show the cell's ventral topography flatten and distance shorten.

HAdase treatment showed that the variation decreased by an average 114.13 from 610.82 ± 9.52 to 496.69 ± 14.26 (see Figure 5.9). And the average mean of the pixel intensity decreased by 402 units, from 13008 to 12606, demonstrating the cells became closer to the substrate. For reference, Figure 5.8 shows the pixel intensity histogram of the top right cells in Figure 5.7 before and after enzyme treatment. The mean intensity decreased by 145.81 unites and the standard deviation of the distribution decreased by 473.57 units.

Our interpretation of this data is that HA patches at the cell-substrate interface deform the cell membrane, pushing it up and away from the substrate through steric and possibly electrostatic repulsion, making it difficult to form adhesive bonds and also placing a strain on the bonds that exist. The gaps generated by the interfacial hyaluronan are eliminated when HAdase digests the polymer, as reflected by the uniform intensity which reflects reduction of the rippling at the interface; and by the darkening on the intensity which reflects the approach of the cell surface towards the substrate.

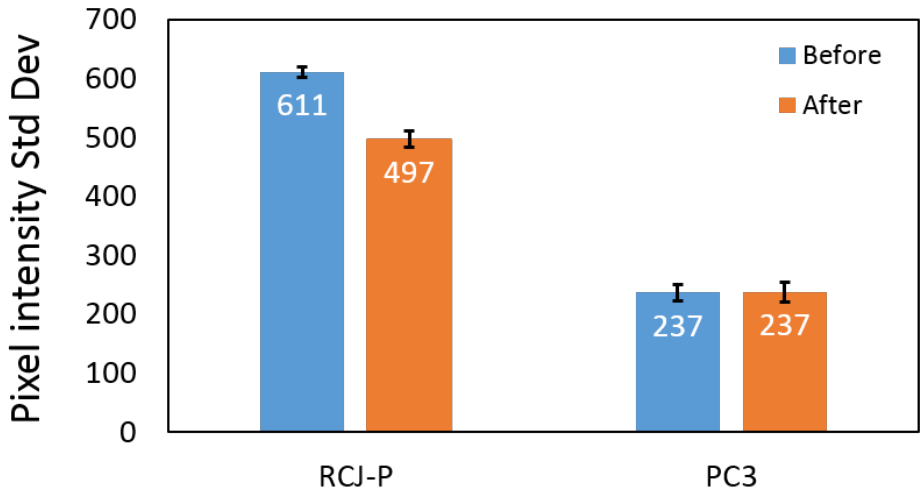

Figure 5.9: The average pixel intensity standard deviation before and after bovine HAdase treatment for 20 minutes. N=44 for RCJ-P and N=31 for PC3.

5.3.3.2 Topography of PC3 cells

A similar strategy to examine topography of the cell membrane of PC3 cells was pursued. RICM images for the PC3 cells revealed that the gap was not as rough as the RCJ-P cells. The quantitative analysis of the RICM images showed the standard deviation of the pixel intensity histogram before and after bovine HAdase treatment for 20 minutes does not change significantly. The average changed from 236.86 ± 13.87 to 237.45 ± 16.71 (see Figure 5.9). And the average intensity decreased by only 21 units, from 7449 to 7428, which is 5% of the average intensity change on RCJ-P cells of 402 units. So comparing to RCJ-P cells, the topography under PC3 cells did not change significantly after HAdase treatment.

5.3.4 HA matrix decreases the adhesion strength

The key experiment to look at how hyaluronan physically mediates adhesion is to quantify whether HA polymers at the cell interface change cell adhesion strength via a mechanical means

(rather than via signaling or some other indirect mechanism). The first quantitative measurements of cell adhesion strength versus hyaluronan were made for this thesis work. The key measurement technique is the hydrodynamic spinning disk apparatus (150, 151). With this technique, the average adhesion strength of cells can be determined by identifying the hydrodynamic shear force required to detach 50% fraction of the cells from the substrate (see Materials and Methods for a full review of this technique).

In this study, measurements of the cell adhesion strength of two HA-rich cell types, RCJP and PC3 are compared with measurements of the same cell's adhesion strength after the pericellular matrix has been altered (e.g. removed) by HAdase enzyme treatment. Two different types of HAdase were compared (bacterial and bovine HAdase – see Materials and Methods). Further, two different exposure times to the enzyme were used for comparison: short time exposure, 15-30 minutes and longtime exposure, 2 hours. The outcome of the experiments is summarized in Figure 5.9 & 5.10 and Table 5.1. For each condition, at minimum triplicates were acquired, where each component of the triplicate often is comprised of several measurements. The total number of individual measurements included in the reported outcome is reported as N, where each N is comprised of an experiment involving 1000s of cells.

In every experiment, the adhesion strength of the given cell type was measured as a control. As discussed at the end of this chapter, this is important because the adhesion strength of the control cells appeared to drift over time, while the comparative results remained relatively (qualitatively) consistent. As reported below, we find that the adhesion strength of the RCJ-P cells (on glass substrate) was consistently higher than the adhesion strength of the PC3 cells adherent on collagen coated surfaces. The average value for RCJP cells was 276.06 ± 11.56 dyne/cm^2

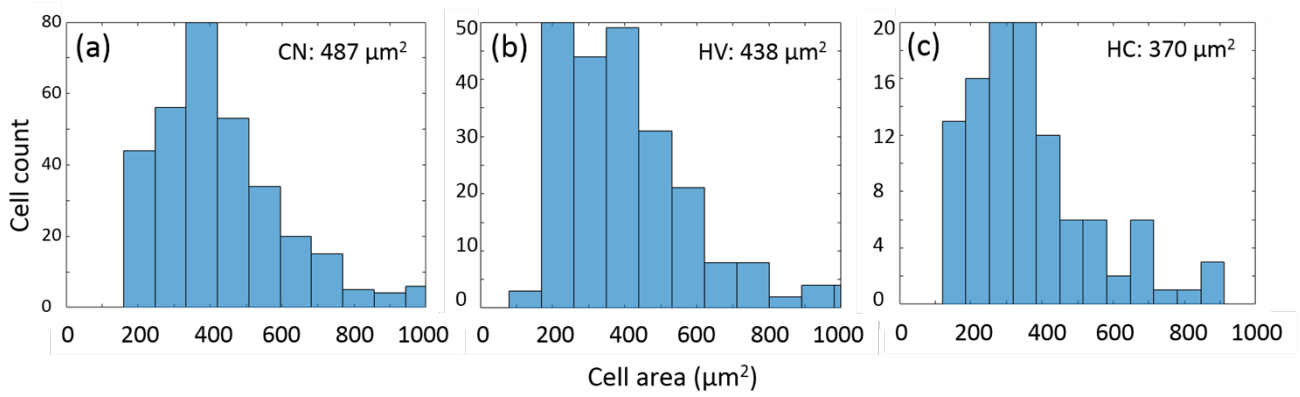

Figure 5.10: Histogram of projected cell area (a) control cells (CN), (b) after bovine HAdase (HV), and (c) after bacterial HAdase treatment (HC) of 15 minutes on RCJ-P cells.

(N=43) while for PC3, the value was typically 70% lower, with an average of 82.94 ± 4.78 dyne/cm^2 (N=27). The weaker adhesion is consistent with smaller adhesive plaques of the PC3 cells and their more rounded, less extended phenotype. How hyaluronan changes the state of these adhesion strengths is the subject of the rest of this section.

5.3.4.1 Evaluation of cell area as a criterion to apply spinning disk

Since the hydrodynamic shear stress depends on cell shape and area, we rely on the premise that for a given cell type and condition, the cells are consistently similar in area and shape (both in the same sample as well as between different conditions). To justify the relative comparison of the cells before and after HAdase enzyme treatment, we performed controls to look at the average cell shape and area before and after enzyme exposure.

Before reviewing the results, it is worth considering how a decrease versus increase in cell area might impact the apparent adhesion strength. Assuming approximately constant volume over the time of the experiments (30 minutes), a decrease in cell area would imply an increase in

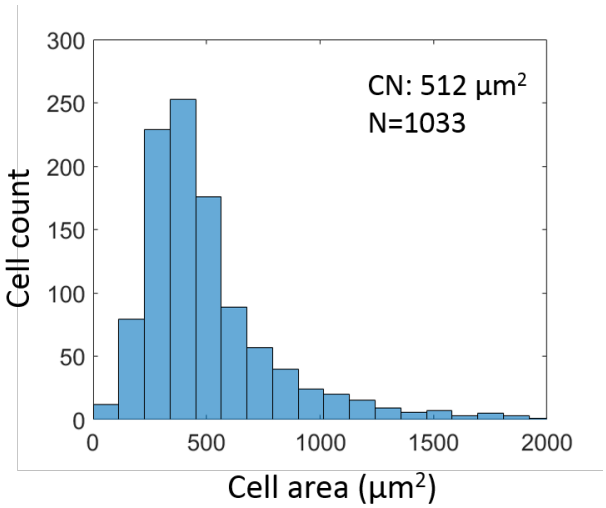

Figure 5.11: PC3 cell area distribution showing it is suitable for spinning disk apparatus.

the material extended from the surface. In that case, if the cell adhesion strength due to binding at interface is constant, it would make it appear as if the adhesion strength decreased. The opposite would be true for an increase in cell area. An increase in cell area would result in a fictitious apparent increase in adhesion strength. For the work here, our hypothesis is that removing HA will decrease mechanical repulsion and therefore increase the cell adhesion strength; all things left the same in shape, we would therefore expect a higher hydrodynamic shear force to remove the cells. Therefore, an increase in area would interfere with interpretation; a decrease in cell area would obscure the results slightly by reducing the effect, but it would not be responsible for increased adhesion.

Calcein AM was used to label the area of the live cells. From images of more than 600 RCJ-P cells, the area *did not increase* significantly after incubation with bovine HAdase nor bacterial HAdase, but it was not quite constant either. The cell area decreased from an average

Table 5.1 Summary of the measured adhesion strengths (and standard error) of HA-rich cells, RCJ-P and PC3, before and after enzymatic degradation of HA.

RCJ-P	Bovine HAdase	RCJ-P	Bovine HAdase
Control	265.08 ± 7.75 dyne/cm^2 (N=12)	Control	212.03 ± 17.70 dyne/cm^2 (N=7)
Short incubation	353.23 ± 11.69 dyne/cm^2 (N=18)	Long incubation	278.41 ± 15.41 dyne/cm^2 (N=9)
RCJ-P	**Bacterial HAdase**		
Control	300.23 ± 17.87 dyne/cm^2 (N=24)		
Short incubation	336.95 ± 22.26 dyne/cm^2 (N=14)		

PC3	Bovine HAdase	PC3	Bovine HAdase
Control	71.39 ± 4.5 dyne/cm^2 (N=8)	Control	68.30 ± 3.80 dyne/cm^2 (N=10)
Short incubation	102.42 ± 14.24 dyne/cm^2 (N=6)	Long incubation	111.61 ± 6.51 dyne/cm^2 (N=10)
PC3	**Bacterial HAdase**	**PC3**	**Bacterial HAdase**
Control	71.39 ± 4.50 dyne/cm^2 (N=8)	Control	73.31 ± 2.67 dyne/cm^2 (N=4)
Short incubation	91.75 ± 7.52 dyne/cm^2 (N=8)	Long incubation	101.24 ± 4.66 dyne/cm^2 (N=4)

area of 487.05 ± 15.66 μm^2 (N=339) for control RCJP cells to 437.97 ± 16.93 μm^2 (N=230) for bovine HAdase treated cells and 369.92 ± 16.90 μm^2 (N=106) for bacterial HAdase treated cells (see Figure 5.10). Since the projected area did not increase, any measured adhesion strength *increase* cannot result from an artefact arising from the cell area change.

The data presented in Figure 5.10a and Figure 5.11 shows that before HAdase treatment, RCP-J and PC3 cells have a relatively narrow distribution of areas, sufficient (if not perfect) for using spinning disk apparatus, that is the standard error of the cell area is less than 5% of the average. Another cell type, Hs578T breast cancer cell line, on the other hand was found to have too much variation in shape and size and therefore was not a good candidate for these measurements even under one condition.

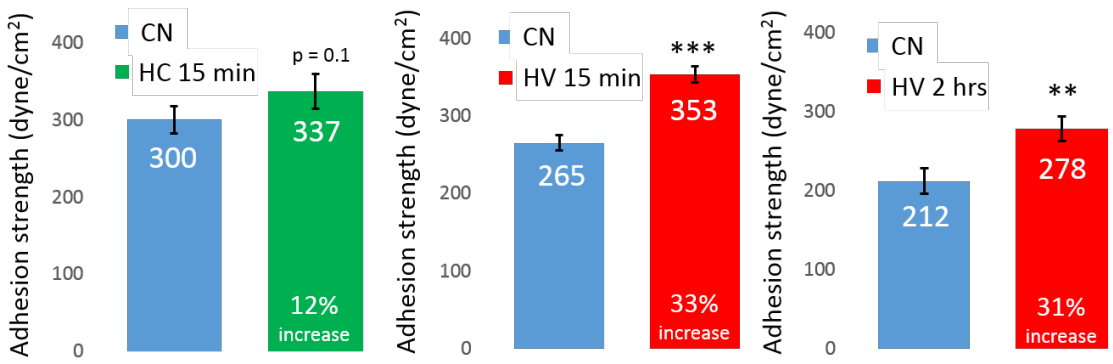

Figure 5.12: Comparison of adhesion strength of RCJ-P cells for control (CN), bovine HAdase (HV) and bacterial HAdase (HC) treatments. Left and middle are short time (15-30min) exposure, right is long time (2hr) exposure to HAdase. * $p<0.05$, ** $p<0.01$, *** $p<0.001$.

5.3.4.2 Spinning disk results consistently show that interfacial HA weakens cell adhesion

The adhesion strength values reported above for the cells under standard conditions, can then be compared to the same cell types' adhesion strengths after HAdase treatment. For short 15-30 incubation periods with bovine HAdase, the adhesion strengths of both the RCJP cells and PC3 cells increased: RCJP by 33% and PC3 by 44%. The results are summarized in Figure 5.12 and 5.13. In more detail, the adhesion strength of control cells for RCJ-P and PC3 were 265.08 ± 7.75 dyne/cm^2 (N=12) and 71.39 ± 4.50 dyne/cm^2 (N=8) respectively. The experiments with two different HAdase on PC3 cells were done at the same time, so the adhesion strength on the control cells is the same for both comparison conditions. The adhesion strength after bovine HAdase treatment were 353.23 ± 11.69 dyne/cm^2 (N=18) and 102.42 ± 14.24 dyne/cm^2 (N=6).

Students t-test shows that the differences are statistically significant where $p<0.001$ for RCJP and $p<0.05$ for PC3.Similar measurements were made using bacterial HAdase at short incubation times. RCJ-P adhesion strength increased more than 12% after HA was depleted while the adhesion strength of PC3 was increased by more than 29%. As summarized in Figure

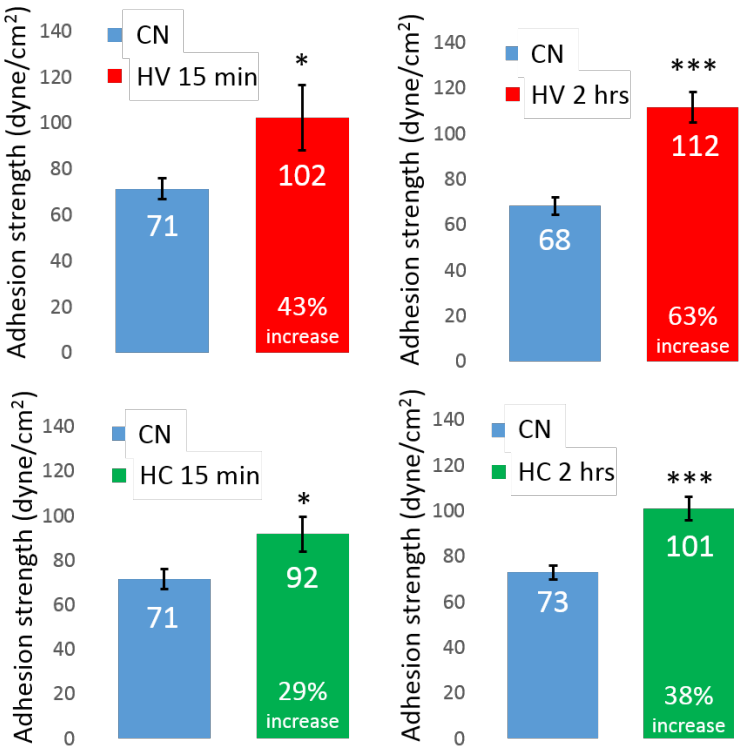

Fig 5.13: Comparison of adhesion strength of PC3 cells for control (CN), bovine HAdase (HV) and bacterial HAdase (HC) treatments (short and long term enzyme treatments); * $p<0.05$, ** $p<0.01$, *** $p<0.001$.

5.9 and 5.10, the absolute numbers of the adhesion strength for each condition/cell type were as follows: for the control cells for RCJ-P and PC3 were 300.23 ± 17.87 dyne/cm^2 (N=24) and 71.39 ± 4.50 dyne/cm^2 (N=8) respectively. The adhesion strength after bacterial HAdase treatment were 336.95 ± 22.26 dyne/cm^2 (N=14) and 91.75 ± 7.52 dyne/cm^2 (N=8). Students t-test shows the p-values were $p<0.1$ for RCJP and $p<0.05$ for PC3.

Measurement of adhesion strength after a longer exposure to bovine HAdase (2 hours) also led to a similar outcome to that of shorter incubation times: the chondrocyte RCJ-P adhesion strength increased by 31%, similar to the 33% increase reported above for the shorter incubation time. The adhesion strength of PC3 rose 65%, slightly more than the 44% increase associated with the shorter incubation time. Results are summarized in Figure 5.12 and 5.13. The adhesion

strength of control cells for RCJ-P and PC3 were 212.03 ± 17.70 dyne/cm^2 (N=7) and 68.30 ± 3.80 dyne/cm^2 (N=10) respectively. The average adhesion strength after bovine HAdase treatment is 278.41 ± 15.41 dyne/cm^2 (N=9) for RCJ-P and 111.61 ± 6.51 dyne/cm^2 (N=10) for PC3 cells. Students t-test shows that the differences are statistically significant where $p<0.01$ for RCJP and $p<0.001$ for PC3.

Before we realized that bacterial HAdase is less specific, digesting chondroitin sulfates as well, we also studied the change in adhesion strength of PC3 cells after 2 hours treatment with bacterial HAdase. The PC3 adhesion strength increased by ~38%, slightly larger than the 29% increase seen after short time treatment with bacterial HAdase, shown in Figure 5.10. This experiment was only done once. The adhesion strength of control cells for PC3 was 73.31 ± 2.67 dyne/cm^2 (N=4). The adhesion strength after bacterial HAdase treatment was 101.24 ± 4.66 dyne/cm^2 (N=4). The p-value is $p<0.001$.

5.4 Discussion

The goal of the spinning disk measurements and accompanying experimental data is to quantitatively test the hypothesis that the presence of HA at the cell-substrate interface reduces external force needed for cell detachment by mechanical repulsion. More specifically, we hypothesized that the presence of HA polymer at interface will exert a repulsive force and in some yet to be determined way, reduces the total cell adhesion strength to the substrate.

Here we compare the data with the hypothesis, and discuss the outcome and interpretation. We find for all conditions used (cell type, type of HAdase, exposure time*),* the cell adhesion strength of the cells qualitatively increases when hyaluronan is removed*.* The results are summarized in Table 5.2. The simplest mechanical interpretation of the increase of adhesion

Table 5.2: Adhesion strength increase (% of control value) of various conditions for RCJ-P and PC3 cells.

Adhesion strength increase	RCJ-P	PC3
Bacterial HAdase short incubation	12%	29%
Bacterial HAdase long incubation	X	38%
Bovine HAdase short incubation	33%	43%
Bovine HAdase long incubation	31%	63%
ChABC short incubation	38%	28%
ChABC long incubation	35%	45%

strength is depicted in Figure 5.14. The model assumes that the total adhesion strength of the cell adhered to the surface is due to the sum of the adhesive forces of the focal adhesions minus the repulsive force of the pericellular matrix/HA patches. If these two separate forces can be superimposed, they partially cancel, reducing the total adhesion strength of the cell to the surface in the presence of HA. The hydrodynamic spinning assay identifies the hydrodynamic shear stress necessary to overcome this net adhesive force. When the hyaluronan repulsion is reduced by the removal of the HA, we assume that the average focal adhesion does not immediately respond but remains constant. Hence, the net adhesion strength is greater in the absence of HA and a larger hydrodynamic force is necessary to remove the cells.

Applying the proposed model, as depicted in Figure 5.14, to the analysis of the results presented in Tables 5.1 and 5.2, we find that it explains the results (e.g. increased adhesion strength due to HA removal) and supports the hypothesis that HA exerts a mechanical repulsive force at the interface that weakens the cell adhesion strength under the cell. The assumptions

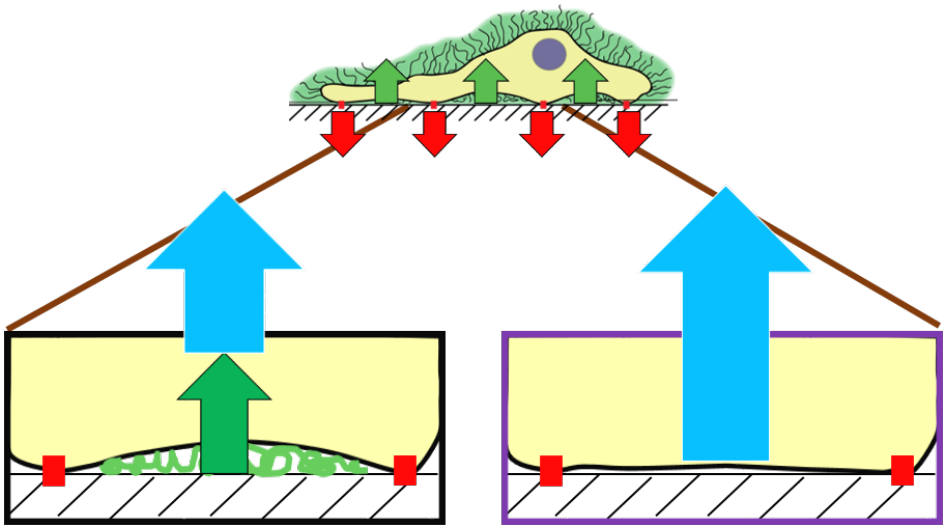

Figure 5.14: Simple mechanical interpretation of the increase of adhesion strength. Left (black box) is on control cells with HA matrix under cell and the right (purple box) is when HA matrix degraded. Red is the FA. Green arrow represents the repulsive force from HA matrix. Blue arrow represents the extra hydrodynamic force required to break FA bonds.

made in order to apply the model are carefully explored below and justified with the support of additional control experiments.

The assumptions include the following: on the time scale of the experiment, the focal adhesion strength (red arrow) does not significantly change in response to the HAdase treatment. The second is that HA exerts a repulsive force (green arrow). The third is that the HA force and adhesion force can be superimposed such that we effectively treat the cell like a 'point particle'. The fourth is that the non-specific adhesion energy between the cell and the substrate is minimal compared to the total adhesion energy.

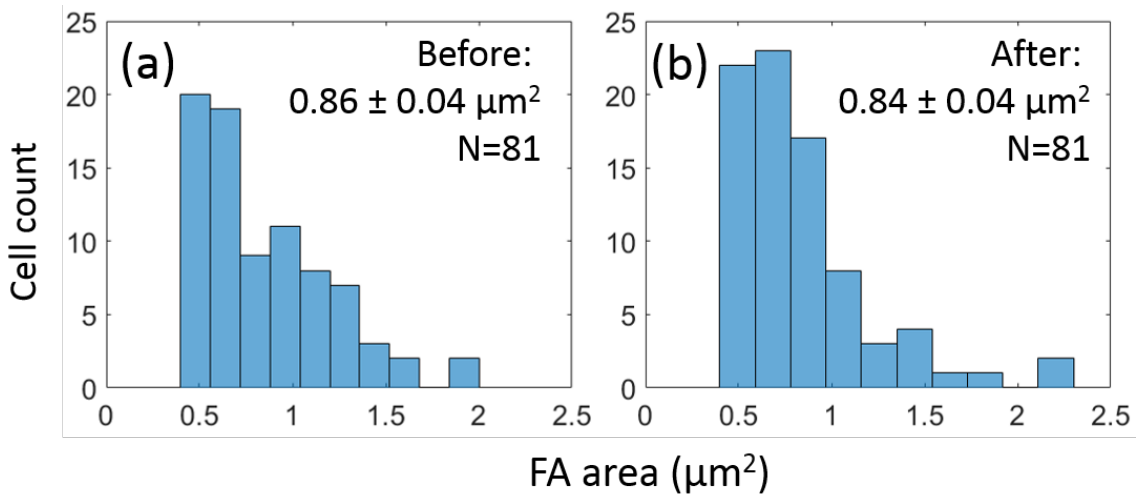

Figure 5.15: FA size distribution of RCJ-P (a) before and (b) after bovine HAdase treatment.

5.4.1 Assumption I: Focal adhesion strength does not significantly change in response to the HAdase treatment

5.4.1.1 FA area remains constant during and after HAdase treatment

Focal adhesions are renown as complex, mechanosensitive elements of the cell. At the beginning of this work, we had no idea whether change in the state of the PCM/HA patches would alter the FA size, composition, and adhesion strength in some way. We therefore sought to characterize directly the apparent response of the FAs, and control for any possible change in adhesion strength (increase) resulting from FA dynamics rather than a depleted repulsive polymer force.

We sought to characterize whether the total focal adhesion force could increase in response to an effect from the enzyme treatment affecting the integrin or other components of the cell; we also aimed to characterize whether the size and/or average number of FAs changed in response, perhaps a mechanosensitive response, to the removal of the HA and the decrease in

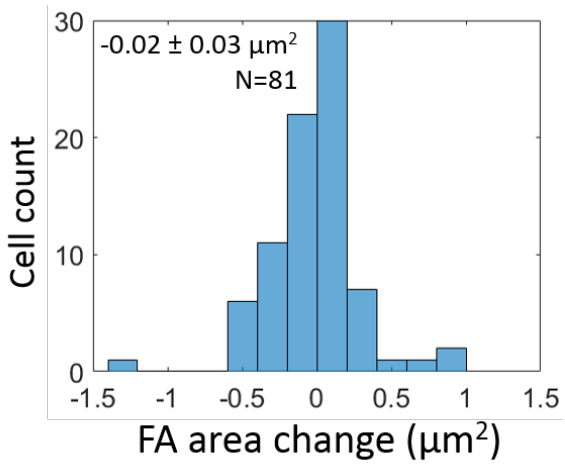

Figure 5.16: Change in FA area after bovine HAdase treatment is small.

the gap between portions of the plasma membrane and the substrate. Focal adhesions were monitored on living RCJ-P cells expressing fluorescent paxillin. After 15-30 minutes of incubation with bovine HAdase (the HA-specific enzyme), the FA area showed minimal change. The average FA area before and after HAdase treatments are 0.86 ± 0.04 μm^2 and 0.84 ± 0.04 μm^2 (N= 3 cells) respectively. Figure 5.15 shows the FA size distribution before and after. We found that on average most FAs remained the same size or if anything, tended on average to slightly decrease in size (see Fig 5.16). Figure 5.17 shows a few blown up images of a particular FA and a comparison of their shape before and after HAdase.

A similar tactic was tried on the PC3 cells. However again the weak intensity of the FAs in transfected PC3 cells (fluorescent paxillin) made analysis tricky. We therefore assume that a similar result is likely given that the FA area remains constant during PC3 exposure to HAdase.

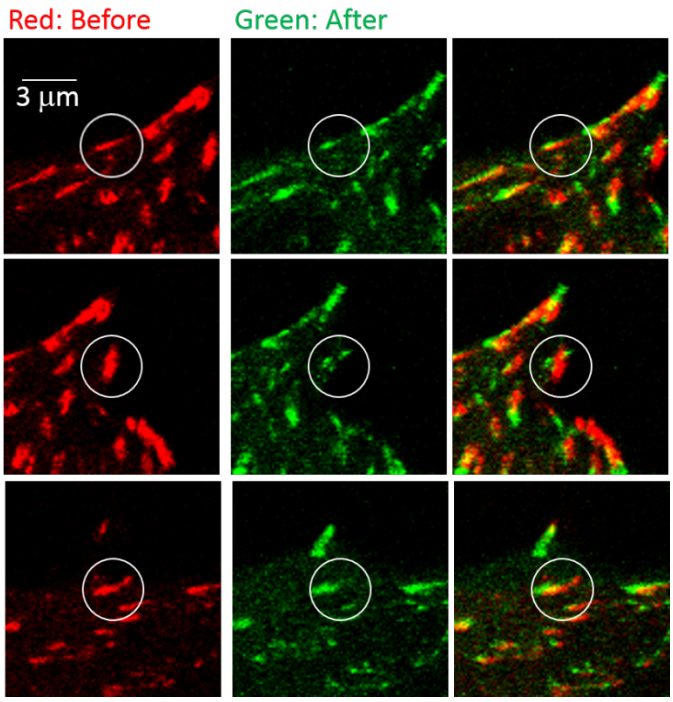

Figure 5.17: FA labeled by GFP-paxillin before (red) and after (green) bovine HAdase treatment on RCJ-P. The third column is the superposition of the two images.

5.4.1.2 Adhesion strength is not increased due to myosin II contractile activity

As discussed in the background, FA size does not necessarily correspond to adhesion strength in mature focal adhesions. Therefore, we performed a second control to interfere with the contraction controlled adhesion strength. Myosin-mediated tension within the lamellar actin cytoskeleton drives changes in FA composition and helps the FA reach maturation (72, 89, 160) and it also is involved in mechanosensitive responses of the cell. We therefore blocked myosin II activity with the drug, blebbistatin, and looked at the adhesion strength of the RCJP cells before and after treatment in the presence and absence of HAdase.

We hypothesize that if no large response of the FA driven by myosin activity takes place, the adhesion strength difference after HAdase treatment with and without blebbistatin should be

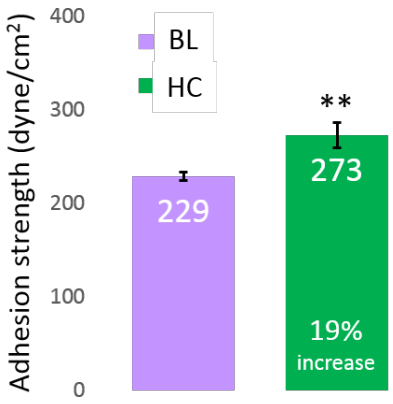

Figure 5.18: Adhesion strength change on RCJ-P with blebbistatin treatments (BL) and after bacterial HAdase treatment of 30 minutes (HC). $p<0.01$.

similar. Although the RCJ-P cells' myosin activity was suppressed by blebbistatin myosin II inhibitor, the adhesion strength increased by 19% after removing HA matrices with bacterial HAdase treatment for 30 minutes. The adhesion strength of the blebbistatin-treated cells was 229.39 ± 4.48 dyne/cm^2 (N=10) and after treating with bacterial HAdase, the adhesion strength of those blebbistatin-treated cells was 273.18 ± 13.58 dyne/cm^2 (N=10). We could only do a relative comparison because blebbistatin treated cells have a smaller area and hence changed (decreased) adhesion strength, as indicated by the absolute numbers. However, the percentage change between the control and the HAdase treated cells (with and without myosin II blocking) is within a few percent. Figure 5.18 and summarizes the outcome. The relative percentage change was near identical, consistent with the interpretation that the increased adhesion to the substrate after HAdase treatment is not driven by contractile activity.

5.4.1.3 Adhesion strength remains constant after enzyme treatment of cells not expressing HA

To better test the assumption that incubation with the HAdase enzyme does not alter cell adhesion, another route was taken. The same adhesion strength experiments were done on a

cell type lacking HA expression and surface associated HA. The rationale is that if treatment with HAdase in this scenario increases the adhesion strength, then it means the adhesion strength increase does not require HA matrix and our hypothesis is wrong.

Chinese Hamster Ovary (CHO) cells do not have a significant amount of HA (161). After treating the CHO cells with bacterial HAdase for 15-30 minutes, the adhesion strength decreased by 0.9%, which was negligible. The adhesion strength of the control cells was 285.08 ± 8.37 dyne/cm^2 (N=13) and after treating with bacterial HAdase for about 30 mins, the adhesion strength was 282.62 ± 13.57 dyne/cm^2 (N=8).

5.4.1.4 Signaling through HA cell surface receptors is under investigation

HA receptors on the cell membrane were shown to be able to transfer biochemical signals via binding HA oligosaccharides (24). The shorter HA polymers or monomers degraded by the enzymes might bind to the receptors and activate a signaling pathway to alter the adhesion behavior. In order to downplay that possibility, the shorter enzyme incubation time (15-30 minutes) was designed to measure the adhesion strength before cell could react to the signaling and concentrate the source of adhesion strength change to the mechanical interference.

To further investigate the possible signaling from the HA oligosaccharides generated by the HAdase, we also planned to compare the adhesion strength of cells with and without exogenous HA oligosaccharides added to the solution. Work towards this experiment, e.g. controls, were performed but the final hydrodynamic assays have not been completed. The controls included adding HA oligosaccharides (at 1 mg/mL concentration) to RCJ-P cells to see

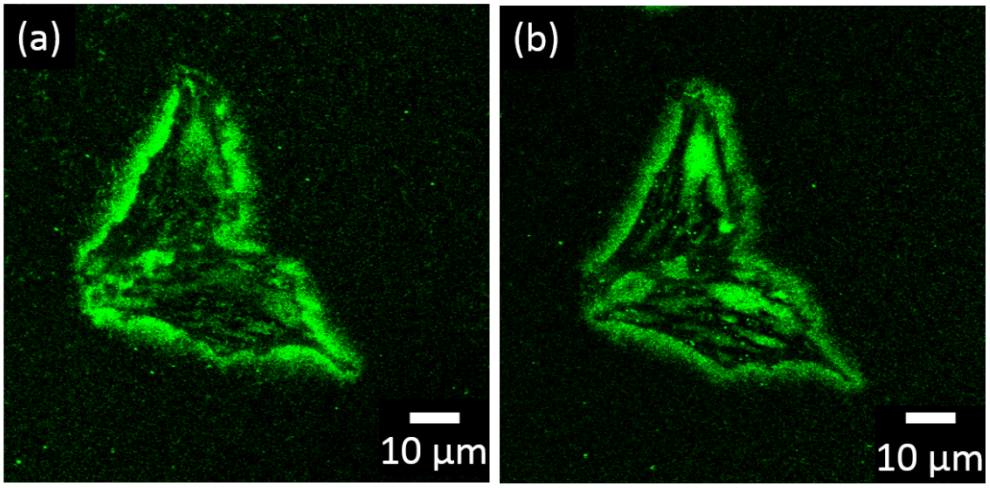

Figure 5.19: Interfacial HA (a) before and (b) after oligo-HA treatment for two hours on RCJ-P cells.

how it impacted the PCM and interfacial HA since oligo-HA is known to competitively bind to CD44 and displace polymeric HA. The experiments showed that the PCM and the interfacial HA labeled with GFPn remained after 2 hours of incubation, and the concentration of interfacial HA increased slightly (Figure 5.19).

For the prostate cancer cells, adding HA oligosaccharides dissipates the PCM around the cells and HA patches under the cells in about 3.5 hours. Reducing the incubation time to two hours led to similar results as the RCJ-P cells; the interfacial HA remained intact (Figure 5.20). It's possible that oligo-HA generated by HAdase at the cell interface could act differently because it may be that they cannot diffuse under the cell to competitively bind in the control experiment. This seems unlikely though, since BSA can diffuse under the RCJP cells (size 66 kDa) while the oligo-HA is only 200 Daltons. It's also possible that the binding kinetics is very different in the confined space where the polymeric HA is far more compressed and confined in mobility. Whatever the case, if we assume that exogenous oligo-HA acts similar to that produced by

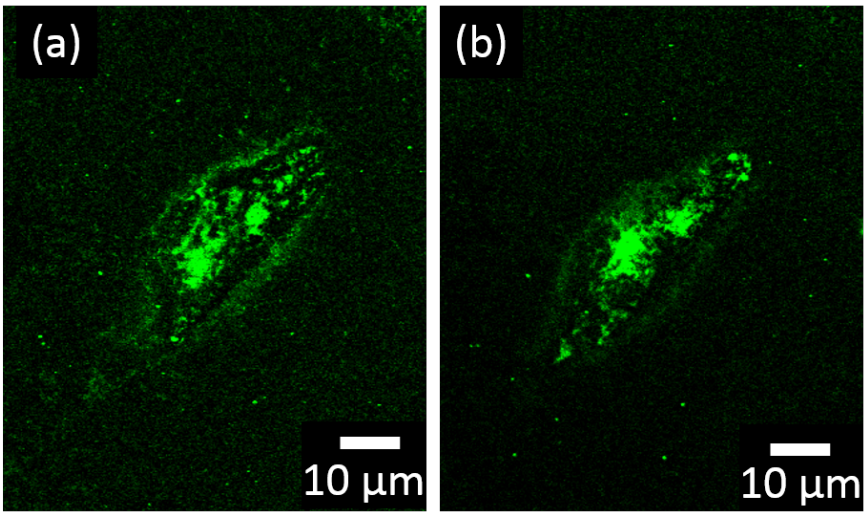

Figure 5.20: Interfacial HA (a) before and (b) after oligo-HA treatment for two hours on PC3 cells.

HAdase, we have shown that it does not significantly impact the interfacial HA and more importantly, it doesn't appear to bind to the CD44 receptors, through which signaling could occur.

However incomplete this approach may be for the reasons identified above; it is still valuable to look at how adhesion strength changes before and after addition of oligosaccharides. So if the oligosaccharides do not cause changes to the focal adhesion, the adhesion strength should remain after 30 minutes of incubation with them. The experiment is not done in time for this writing.

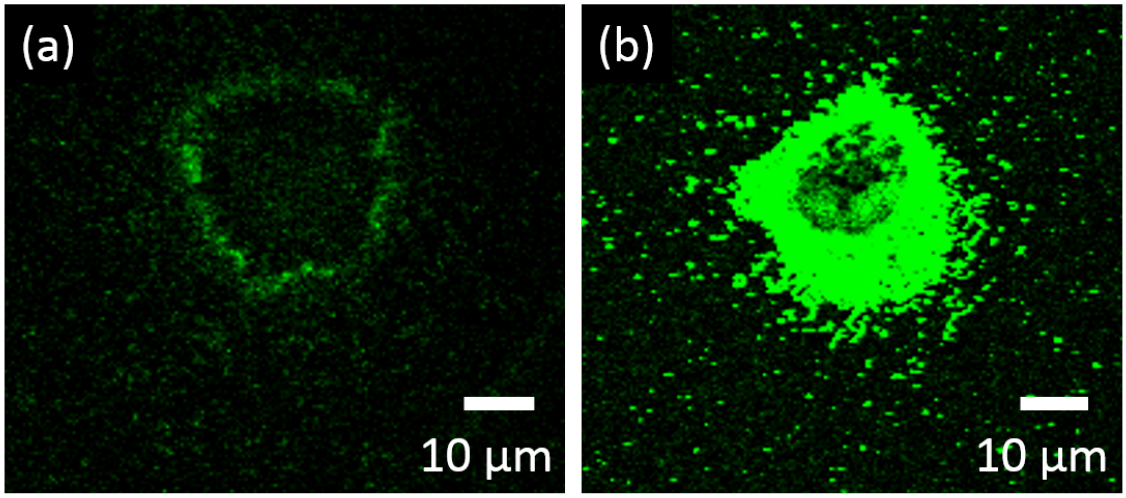

Figure 5.21: HA labeled by GFPn under (a) 4-MU treated cells and (b) 2 hours after 4-MU washed off showing HA patches grown back under cells. Images are on the same RCJ-P cell using the same settings (which is why the figure on the right is saturated).

5.4.2 Assumption II: HA can exert a repulsive force at the cell-substrate interface

Studies show that polymer brushes and in particular, end-grafted hyaluronan films are well-described as elastic polymer brushes (123). Compression of the end-grafted polymer brush by a flat surface leads to an exponential increase in force dependent on the compression distance (123). Based on polymer physics and the electrostatics from the negatively charged HA, the compressed HA matrix under the cells is predicted to thus exert a repulsive force between the cell and substrate, which will be removed when the HA is digested.

To test this assumption of HA repulsive force, we attempted to compare the adhesion strength of cells with no HA due to a drug-induced suppression in HA synthesis versus cells where the HA synthesis was increased by removing the drug. 4-methylumbelliferone (4-MU) has been used as a low toxicity, high potency inhibitor of HA biosynthesis (162). 4-MU sequesters one of the main sugar monomers of HA to inhibit HA synthesis. Unfortunately, it also impacts the synthesis of other glycans as well, so it can have unwanted side effects.

After trypsinization, which removes the PCM, RCJ-P cells were plated in the presence of 4-MU. Therefore, the entire adhesion process occurred in the absence of HA at the interface. (Separate controls show that the PCM is detectable with RBC PEAs after about 3 hrs). Imaging with GFPn showed the absence of ventral HA patches throughout exposure to 4-MU both at the interface and around the cell body (i.e. no PCM). After washing and replacing with fresh culture media, RCJ-P cells grew back a partial HA matrix in 2 hours.

We compared the adhesion strength of RCJ-P cells exposed to 4-MU in this fashion for 4+2 hours with RCJ-P cells exposed to 4-MU for 4 hours and then allowed to grow with no 4-MU for two more hours. The outcome was surprising. Against our hypothesis that the cells with fresh HA at the interface should produce a weaker adhesion strength, instead the 4-MU free cells had a 15% stronger adhesion. The adhesion strength of 4-MU cells was 230.17 ± 13.73 dyne/cm^2 (N=18) while the adhesion strength for the cells with HA was 264.64 ± 12.46 dyne/cm^2 (N=23).

This result was inconsistent with our hypothesis that HA matrix repels the cells from the substrate. The experimental setting with the 4-MU was new to our lab, so more control studies of the 4-MU effect on cells still need to be done. The following are two control experiments that was done and more to do. The adhesion strength measurements were done 6 hours after seeding, and the HA regrowth process was initiated at 4 hours after seeding. The time points were chosen because the sequestration of HA monomer sugar need to be minimized since the sugar is essential for other functions of the cell but at the same time, the cell adhesion strength should be in a stable state so that the HA effect can be isolated. Control experiments showed seeding RCJ-P with 4-MU for 4 hours and 6 hours had similar adhesion strength. The adhesion strength at 4 hours was 185.25 ± 30.15 dyne/cm^2 (N=2) and at 6 hours was 184.91 ± 25.68 dyne/cm^2 (N=3) showing the adhesion strength reached stable before 4 hours seeding time. However, this control

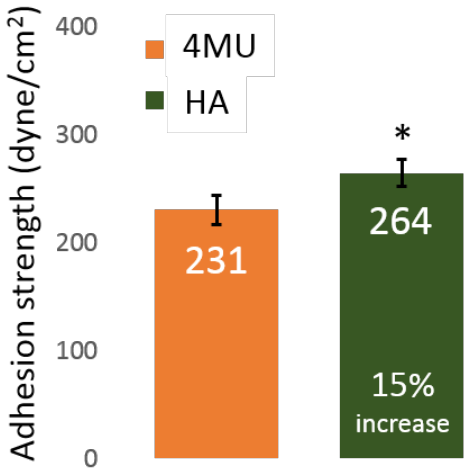

Figure 5.22: Adhesion strength change on RCJ-P with 4-MU treatment (4MU) and after HA growth (HA); $p<0.05$

experiment was only done once due to time constraint and needed to be repeated for confirmation. No conclusion should be made before the confirmation of the time required for adhesion strength stabilization.

Comparing the with control cells, the 4-MU treated cells seeding for 4 hours did not spread out well on the substrate. The morphology of the 4-MU cells was more round, which was usually associated with cells of weaker adhesion. However, 4 hours after seeding, the adhesion strength of the control cells and cells seeding with 4-MU were similar. The adhesion strength of the control cells and 4-MU treated cells were 149.83 ± 12.18 dyne/cm^2 (N=5) and 143.41 ± 26.41 dyne/cm^2 (N=3) respectively (Figure 5.22). This control was also only done once so further confirmation is needed before a conclusion can be made. If one assumes that in fact the rounder cells have a higher shear stress acting on them, then the same results in adhesion strength would be consistent with the 4-MU cells being more tightly bound to the surface. This actually would be consistent with the idea that cells with HA present (control cells) should have a weaker adhesion strength versus those with no HA. It is also interesting because at least naively, one might expect

the ‘sicker’ cells which are possibly experiencing side effects from the drug, should have a weaker adhesion not stronger.

More studies of the change on FA in the presence of 4-MU are required. Fluorescent paxillin in the transfected cells can be used to compare the state of FA with and without 4-MU present. The size, shape and location of the FA can be monitored at different time points of the adhesion as well.

5.4.3 Assumption III: The HA force and adhesion force can be superimposed

The transmembrane FA anchors the cytoskeleton to the substrate by binding to both structures. The anchoring force is transmitted to the whole cell body through the cytoskeleton system. The repulsive force from the HA matrix push on the cell membrane it’s in contact with. Both forces act on the whole cell so they can be superimposed.

5.4.4 Assumption IV: The non-specific adhesion energy between the cell and the substrate is minimal compared to the total adhesion energy

PC3 cells have the same adhesion strength on collagen surfaces with and without BSA, which blocks the non-specific binding between cell and the substrate. It indicates that the difference in adhesion strength does not arise from the variations in non-specific interactions. Repeating the same control for RCJP on glass seemed poorly defined, since the entire surface would be blocked.

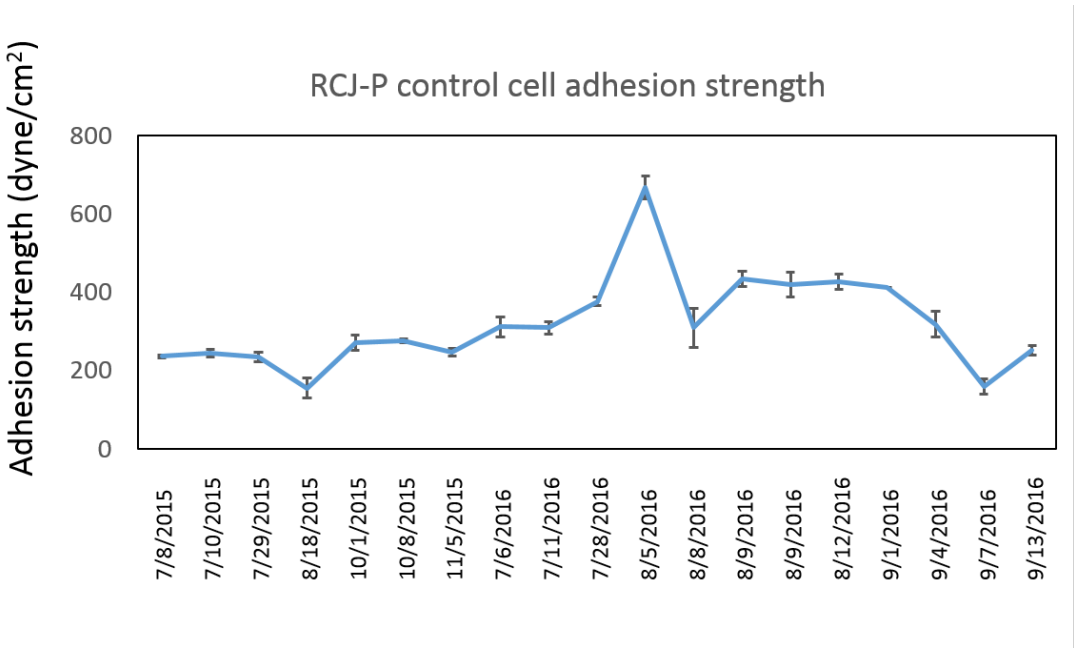

Figure 5.23: Adhesion strength of RCJ-P control cells drift over time.

5.4.5 Full disclosure: Other possible issues in approach and the analysis used to study HA-mediated cell adhesion

5.4.5.1 Drift of adhesion strength over time and issues with reproducibility

During the experiments, the adhesion strength of the control cells was not constant, but there was no particular trend for the shift. Cell culture conditions were kept at constant to the best of our ability but there might still be some variations in the cells' condition that caused this inconsistency. However, with the changing adhesion strength on the control cells, the majority of the experiments showed an increase of adhesion strength after the HA matrix depletion. During the summer of 2016, both cell lines' adhesion strength for control cells are abnormally higher and during that period, depleting HA matrix did not increase the adhesion strength. After an overhaul of everything in the experiment including warming up new vial of cells, using new bottles of culture

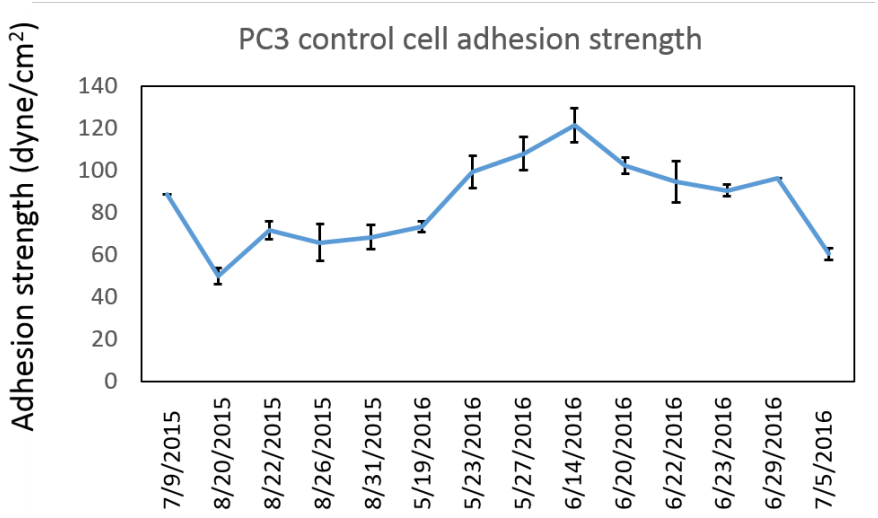

Figure 5.24: Adhesion strength of PC3 control cells drift over time.

media and reagents, switching to a new box of round cover glasses, the adhesion strength of the both cell lines decreased, although it did not go to the previous level, the adhesion strength increased again after the enzyme treatment. We speculated that it could be that the high adhesion strength reached the regime that it is so high comparing to the repulsive force the HA matrix can exert so that taking away the repulsive force did not pose a significant increase in the adhesion strength.

5.4.5.2 HAdase calibration not done quantitatively

The enzyme activity was not quantified so some of the discrepancies in the adhesion strength change might come from the different enzyme activity caused by different batch production or the decay of enzyme itself. However, the enzyme activity was checked qualitatively

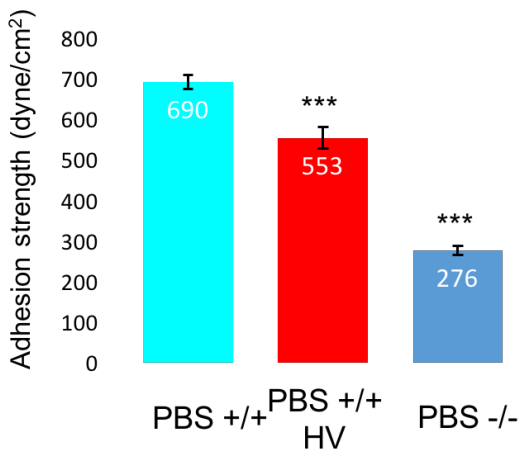

Figure 5.25: Adhesion strength of control and bovine HAdase treated cells RCJ-P in PBS (+/+) with divalent ions, and control cells in PBS (-/-) without ions; *** $p<0.001$.

by making sure the HA matrix labeled with GFPn disappeared after 15 minutes of enzyme incubation and there's no drastic change in the cell phenotype, such as cell shape, size or viability.

5.4.5.3 PBS lacking ions impacts FA response

The 5 minutes in which shear stress of the spinning disk was applied to the cells, they were in a PBS solution without the divalent ions, Ca^{2+} and Mg^{2+}, for FAs. When the cells were spun in the PBS with those ions, PBS (+/+), the adhesion strength of RCJ-P appeared much higher than the cells spun in the PBS without Ca^{2+} and Mg^{2+}, PBS (-/-) (Figure 5.25). The adhesion strength of the control cells in PBS (+/+) was 2.5 times higher than that in PBS (-/-) and they are 690.05 ± 16.82 dyne/cm^2 (N=10) and 276.06 ± 11.56 dyne/cm^2 (N=43) respectively. And the bovine HAdase treatment of 15 minutes decreased the adhesion strength by about 20% to 553.38 ± 25.82 dyne/cm^2 (N=7). However, those experiments were done during the time with especially higher control adhesion strength and the enzyme treatment didn't change the adhesion strength. This experiment hasn't been repeated after the cells went back to normal and the HAdase

treatments increased the adhesion strength. More experiments are to be performed to make sure the reproducibility of this result. Also, future spinning disk experiments should be done in the PBS (+/+) providing FA the necessary condition for proper functions.

5.4.5.4 Role of extracellular matrix proteins in hyaluronan mediated adhesion

Although all the experiments on PC3 cells were performed on collagen coated surface, experiments on RCJ-P cells were done on untreated glass surfaces. RCJ-P cells adhere and spread well when seeded onto glass so we have continued seeding them on glass for the adhesion experiments. However, for a more well-defined adhesion experiment, the cells should be seeded on surfaces covered with extracellular matrix proteins. Preliminary studies of RCJ-P cells on fibronectin surfaces began at a time in our lab when reproducibility of previous results was very difficult. Hence we were unable to systematically pursue the somewhat shocking results of this experiment.

Comparing the adhesion strength of RCJ-P cells on glass, collagen coated and fibronectin-coated surfaces, adhesion strength on fibronectin was 86% higher than on glass or collagen, on which the adhesion strength was similar to on glass. The adhesion strength of control cells on glass, collagen and fibronectin coated surfaces are 312.228 ± 25.23 dyne/cm^2 (N=3), 288.37 ± 9.55 dyne/cm^2 (N=3) and 579.57 ± 5.60 dyne/cm^2 (N=3). Students t-test shows the p-values were $p=0.43$ for collagen surface and $p<0.001$ for fibronectin surface when comparing to glass surface (Figure 5.26). Repeated experiments are needed to confirm this result.

Treating the RCJ-P cells seeded on fibronectin with bovine HAdase and bacterial HAdase, the adhesion strength *decreased* rather than increased. The adhesion strength of control cells for RCJ-P on the fibronectin treated surface were 554.97 ± 12.54 dyne/cm^2 (N=7). The average

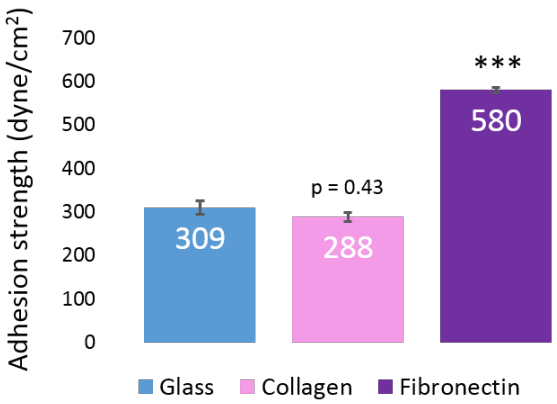

Figure 5.26: Adhesion strength of RCJ-P on various surfaces; *** p<0.001.

adhesion strength after bovine HAdase treatment is 458.01 ± 19.17 dyne/cm^2 (N=7) and after bacterial HAdase treatment is 453.80 ± 20.77 dyne/cm^2 (N=6). Students t-test shows that the differences are statistically significant where p<0.01 for RCJP and p<0.001 for PC3 (Figure 5.27). This is the exact opposite of the results reported for RCJ-P cells on glass. Searching for a self-consistent explanation of these results, the one possible scenario that we could identify involves adhesive interaction between the interfacial HA and the fibronectin. If adhesion takes place, this could help further anchor the cell to the surface. Indeed, in studies of early onset of cell adhesion before focal adhesion formation, Geiger et al proposed that HA is useful for anchoring cells to surface (163). To our knowledge, HA does not bind directly to fibronectin. Various HA-binding proteins are known to interact with fibronectin, the most likely candidate of which is the bottlebrush CSPG, aggrecan (on these cells). It has been shown that aggrecan CSPG can bind to fibronectin (164). It might be that with the higher concentration of fibronectin on the substrate, the binding between the HA matrix and fibronectin increased the overall adhesion strength. When the HA matrix was digested, the binding force from the matrix also disappeared. So although HA digestion increased the adhesion strength by taking away the repulsive force of the HA matrix, losing the

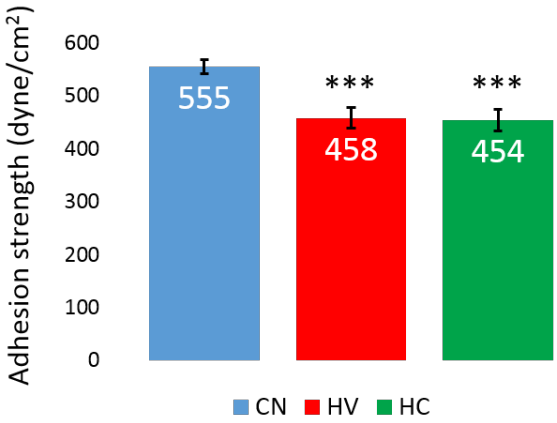

Figure 5.27: Adhesion strength of RCJ-P cells decreased after bovine HAdase (HV) and bacterial HAdase (HC) treatments of 15 minutes on fibronectin coated surface; * $p<0.05$, ** $p<0.01$, *** $p<0.001$.

extra binding force with the fibronectin over-powered the gain, and the overall adhesion strength decreased.

5.4.5.5 Cell shape and size control

The heterogeneity of the cells in their sizes and shapes results in less accurate and consistent adhesion strength measurements. It would be best to control the cell-substrate contact area and cell shape (151) using micropatterened surfaces. Efforts were made to devise micropatterning on the substrate in the Curtis, but it is still in progress. Nevertheless, the results presented here are quite good evidence that HA repulsion changes cell adhesion strength, and provide at least a qualitative evidence that the mechanics is likely to alter the adhesion strength somewhere between 10-50% of the total adhesion strength generated by the focal adhesions.

5.5 Conclusion and Outlook

In the work presented in this chapter, we have illustrated the presence of HA patches under cells and a spatial anti-correlation between the FA and those HA patches. The anti-correlation was shown on three different cell types, rat's chondrocyte cells RCJ-P, human prostate cancer cell PC3, and human breast cancer cell Hs578T. This spatial anti-correlation of FA and HA is robust for it is observed not only in these different cell types but also in mammary epithelial cells (88). With the RICM images showing the space under the cells disappear after the HA patches are digested, we have demonstrated the HA matrix under the cells created gaps between cell and substrate. The gap created by HA might decrease the possibility of integrin binding forming because the comparison to the place where cells in contact with the substrate coincide with FA. Also, the fact that the space between the cell and the substrate can be removed by depleting HA matrix suggests that HA exerts a force on the cells that push the cell off the substrate.

Quantitative measurement of the adhesion strength showed the cell adheres stronger after the HA matrix was removed. This fits our hypothesis that the HA matrix exerts a repulsive force under the cell to orchestrate the complex adhesion event along with the anchoring force by the FA. It brings us back to the inspirational model of the adhesion. We provide evidence that at the part of the cells lacking HA matrix under cell has stronger adhesion strength than the other areas with average or more amount of HA accumulation. So that when the actomyosin system contracts during cell migration, the weaker end of the cell will detach from the substrate while the other end will stay attached. Continuous contraction of the cell will pull the cell toward the stronger adhere end and move the whole cell in that direction. However, the mechanism of which HA matrix facilitate the weaker cell adhesion still need to be fleshed out. Our analysis is based on several assumptions that we tried to address in this documents, but the repulsive force hypothesis still

needs to be tested further. Also that the integration and mechanosensing of the FA to the HA matrix state should be looked at more carefully.

In this present studies, uncertainty has raised because of the enzyme activity. The unquantified enzyme activity, the possible effect of the enzyme to the cell, and the degraded HA matrix adding an extra layer of signaling molecules have all introduce more noise in our study. Future investigation should utilize tools to genetically modify the expression of HA synthase, HA receptors or the CSPG for a more elegant experiment.

Another area to pursue is the interactions between HA patches and the underlying ECM. We had some intriguing but complicated result that RCJ-P cells adhere stronger on surfaces coated with fibronectin than on collagen-coated surfaces. The adhesion strength on the fibronectin is 86% larger than that on the collagen-coated surface or undefined glass surfaces. While the adhesion strength increases after HA degradation on collagen surfaces and glass surfaces, the adhesion strength decreases significantly after HA removal on the fibronectin surfaces. Our first thought was that there are bindings happen between the HA matrix under cell and fibronectin, which add an additional anchorage to the cells which over-powered the effect of HA presence. So degrading the HA, in the end, decreases the overall adhesion strength. Future adhesion experiments should be done on well-defined surfaces.

Surface ligand density was shown to affect the adhesion strength (165). A possible experiment is to decrease the ligand density and decrease the adhesion strength. After depleting the HA matrix with enzyme, compare the adhesion strength change. If HA patches around cell exert repulsive force, then the change between the two surfaces should be the same. Controls need to be done to make sure cells produce the same amount of HA on both surfaces.

Chapter 6

Chondroitin Sulfate Mediated Cell Adhesion

6.1 Overview

Previous studies have suggested that bottlebrush CSPGs (also known as lecticans or hyalectans) are relevant at the cell-substrate interface (37, 166). Further, it is known that lecticans are a major component in the pericellular matrix and interact strongly with hyaluronan via the HA binding domain, the link module and reinforcement by link protein. In many scenarios, it has been demonstrated that lectican's large size and high negative charge make them strongly repulsive both sterically and electrostatically; for example, neural crest cell migration (142), cancer malignancy (167) and synaptogenesis (15). These observations combined with our novel technique to look at HA-mediated cell adhesion prompted the investigation reported in this chapter: to begin to quantify if and how lectican impacts cell adhesion strength. Indeed, our general strategy was to look for straightforward approaches to modify the PCM and quantify changes in adhesion strength. After HA modification, lectican was the next most straightforward candidate. Given the constraints of this PhD period, the enzymatic degradation of chondroitin sulfate (CS) via ChABC and aggrecan via aggrecanase was the most practical approach. Ultimately, however, we intend to use the gentler, non-enzymatic approach of genetic modification of the expression of HAS, CD44 (or relevant HA receptor) and lectican.

As will become clear, the outcome of this study proved to be surprising in multiple ways. On one hand, the preliminary data looking at how enzymatic degradation with ChABC impacts cell adhesion strength, suggested a robust and reproducible effect of increased adhesion, even larger than that found when removing hyaluronan. We originally interpreted this result as consistent with what was expected. We hypothesized that lecticans play a dominant role in the

repulsive force. Their digestion could significantly reduce that force, and led to an increased cell adhesion strength (see model Ch. 5). The increased adhesion strength when compared to hyaluronan digestion was hypothesized to be reasonable since HAdase would only remove HA, not the bottlebrushes. If lectican remained trapped at the interface after HA digestion, they could still have a significant impact. On the other hand, HA without bottlebrushes is expected to have a far of an impact, as exemplified by the shrinkage of RCJ-P PCM from 7microns to ~1um after ChABC digestion of the cell coat.

Yet, to provide further complementary evidence for the proposed interpretation that bottlebrush removal significantly increases the adhesion strength, we arrived at null results despite our multipronged efforts to demonstrate concretely that lectican exists at the cell–substrate interface continuously yielded null results. For quite some time, however, this did not detract us because similar efforts failed in labelling the lectican in PCM where we are 100% confident it is present (see Ch.4). Finally, as the rationale and modeling of the system evolved, we concluded that confinement of the large bottlebrush proteoglycans at the cell interface will require big ruffles and gaps, with tremendous topographical variations (at least ~100-200 nm for just one lectican). Therefore, we turned to RICM to look at the impact of enzymes including both HAdase and ChABC. We were quite surprised to find, as reported below, that HAdase consistently reduces the topography and creates a uniform interface, while ChABC performs intermittently, reducing the topography of only a sub-fraction of the cells. Hence, the results presented in this chapter do not integrate as nicely as the similar study of HA-dependent adhesion. Instead, we provide evidence that lectican may not exist at the cell-substrate interface (in cell culture) at all, at least on RCJ-P cells.

In light of this, it is very surprising that ChABC enzymatic degradation has a serious impact on cell adhesion strength, increasing it by more than 30%. This chapter reports the data as it stands, and discusses possible mechanisms for the impact of CS on cell adhesion.

6.2 Materials and Methods

6.2.1 Cell culture and sample preparation

See section 3.2.1

6.2.2 Enzyme treatment

Chondroitinase ABC (ChABC) from Proteus vulgaris (Sigma: C2905) was used to digest the chondroitin sulfate side chains of aggrecan. ChABC was dissolved in PBS and then directly added to cell sample to achieve a final concentration of 0.27 unit/mL.

Aggrecanase, ADAMTS-4 recombinant, was purchased from EMD Millipore. It was diluted into 20 mM Tris-HCl at pH 7.5 with 10 mM of $CaCl_2$ and 0.05% Brij detergent. Concentrations of 0.1 µg/ml to 10 µg/ml were tested but no change in the PCM thickness was observed by PEA.

6.2.3 Spinning disk adhesion assay

See sections 5.2.6 and 5.2.7

6.2.4 Immunocytochemistry with antibody CS56

Cells were fixed for 15 minutes in 4% formaldehyde, washed and blocked with 10% donkey serum for 60 minutes. Anti-CS primary antibody (CS-56, Abcam: ab11570) with 10% serum was incubated overnight at room temperature. After washing, secondary antibody, donkey anti-mouse IgG Alexa 405 (Abcam: ab175658), was added for 60 minutes, and then mounted in fluorosave, ProLong Gold, for image.

6.2.5 Fluorescently labeled histone

Histone type II-A (H9250; ~20kDa, Sigma Aldrich, St. Louis, MO) was dissolve in PBS to reach 1 mg/mL. Fluorescent-labeling was achieved by incubating the protein with ATTO NHS ester dye at 2 mg/mL for one hour followed by a Zeba desalting column (89882; Thermo Scientific, Waltham, MA) to remove excess dye.

6.3 Results

6.3.1 Cell adhesion strength increases after chondroitin sulfate enzymatic degradation

Inspired by the other reports on the effect of various lectican on the adhesion process, we found the cell adhesion strength increased after ChABC treatment, consistent with the naive expectation that removal of lecticans would remove a large repulsive force and increase measured adhesion strength. For RCJ-P cells, incubating the cells with ChABC for 15 minutes increased the adhesion strength by 38%, where the control cells had absolute strengths of 265.08 ± 7.75 dyne/cm^2 (N=12) to 366.93 ± 21.25 dyne/cm^2 (N=6). After incubating the cells with ChABC for 2 hours, the adhesion strength increased by 35% and went from control cells 212.03 ± 17.70 dyne/cm^2 (N=7) to 285.67 ± 9.56 dyne/cm^2 (N=6). The changes are statistically significant with p-value being $p<0.001$ and $p<0.01$ respectively.

Just as the experimental design in Ch.5, the adhesion strength measurements were executed using two different enzyme incubation times, a shorter incubation time of 15 minutes and a longer incubation time of 2 hours. The 2 hours incubation time was chosen because that time was required during the PCM manipulation experiments reported in Ch.4. However, to focus on the physical mechanics of the CS affecting cell adhesion and avoid cell adjusting its adhesion in response to the PCM change or signaling from enzyme residues, a shorter 15 minutes incubation time was chosen. Incubating cells with ChABC for 15 minutes has been shown in

Table 6.1: Adhesion strength percent change (comparing to control adhesion strength) of various enzyme treatment on RCJ-P and PC3 cells

Adhesion strength increase	RCJ-P	PC3
Bacterial HAdase short incubation	12%	29%
Bacterial HAdase long incubation	X	38%
Bovine HAdase short incubation	33%	43%
Bovine HAdase long incubation	31%	63%
ChABC short incubation	38%	28%
ChABC long incubation	35%	45%

control experiment to fully degrade and collapse the PCM around the cells above the surface.

For PC3 cells, incubating the cells with ChABC for 15 minutes increased the adhesion strength by 28%, from control cells 109.47 ± 7.51 dyne/cm^2 (N=9) to 140.20 ± 9.73 dyne/cm^2 (N=6). After incubating the cells with ChABC for 2 hours the adhesion strength increased by 45%, went from control cells 68.30 ± 3.80 dyne/cm^2 (N=10) to 99.37 ± 3.83 dyne/cm^2 (N=13). The changes are also statistically significant with the p-value being $p<0.05$ and $p<0.001$ respectively.

Same as in section 5.3.4, control to test if the cell projected area increase after ChABC treatment was done because increase in cell projected area will give a false illusion of adhesion strength increase. Images of more than 300 calcein-AM-labeled RCJ-P cells showed the area did not increase after 15 minutes incubation with ChABC. The average area of the cells decreased from 544.48 ± 28.58 μm^2 (N=181) on control cells to 441.22 ± 27.04 μm^2 (N=164) on ChABC treated cells. Therefore, the adhesion strength increase was not an artefact from cell area change (If anything, one might expect the adhesion strength will decrease). However, the FA area change before and after ChABC treatment was not done by the time of this writing and should be completed.

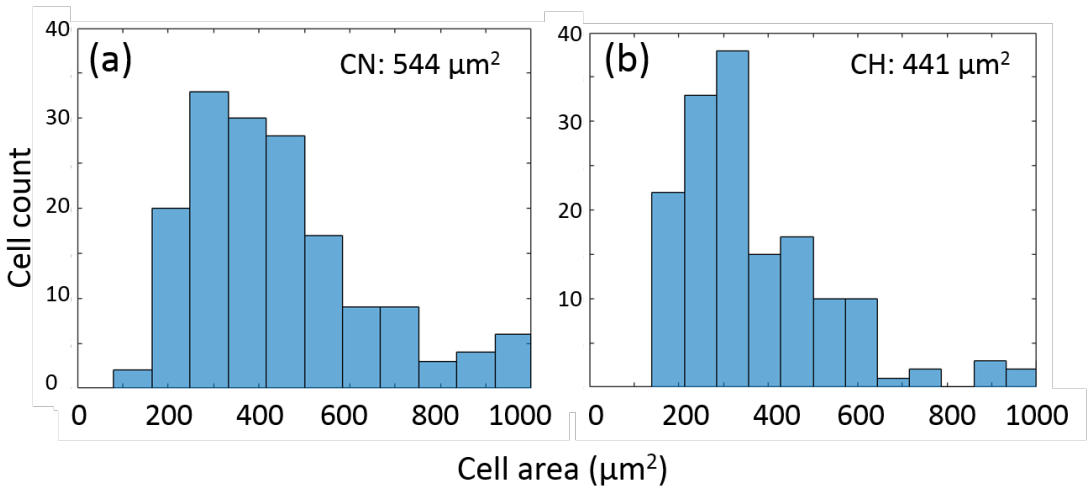

Figure 6.1: Histogram of projected cell area (a) before and (b) after ChABC treatment of 15 minutes on RCJ-P cells.

6.3.2 Exogenous aggrecan does not alter cell adhesion strength

In chapter 4, exogenous aggrecan was shown to increase the PCM thickness around the cells and reduce the pore size of the cell coat. Here we investigate whether exogenous aggrecan diffuses under the cell and impacts adhesion strength. Although the experiment was only done once, the adhesion strength of RCJ-P treated with exogenous aggrecan, 363.79 ± 40.25 dyne/cm^2 (N=3), was similar to the control cells, 370.33 ± 37.89 dyne/cm^2 (N=12). The same experiment was repeated on another type of cell, the breast cancer cell line MDA-MB-231, which yielded similar results. The experiment on the breast cancer cell was also done only one time, and the adhesion strength of the control and exogenous aggrecan treated cells were 240.00 ± 7.88 dyne/cm^2 (N=8) and 243.62 dyne/cm^2 (N=1) respectively. Complementary fluorescence studies to check if fluorescently-labeled exogenous ACAN permeated below the cell surface of RCJ-P cells suggested that it does not.

As a side note, these experiments are an interesting control of the impact of swollen PCM on the shear stress on the cells. It is possible that enhanced PCM, which effectively increases the

extent of the cell, could impact that hydrodynamic forces on the cells. Yet, as one might expect, this extremely soft, deformable matrix has little impact even when it is more than doubled in its extent in these experiments (97).

6.3.3 Efforts to confirm that lectican exists at the cell-substrate interface

The increased adhesion strength after digestion of CS inspired us to confirm our standing assumption, based on the literature, that lecticans are present at the cell-substrate interface in PCM-rich cells (37). Originally we were convinced that since the PCM is extended on our model cell lines, there must be lectican like aggrecan on the RCJ-P and versican on the prostate cancer cells at the interface as well. Lectican is one of the main components of the pericellular matrix, and the large size of lectican (average 80 x 300 nm with a hydrodynamic radius of ~150 nm (168)) can generate the gap under the cells and exert the repulsive force between cell and substrate. Various efforts were made to investigate/confirm the presence of lecticans, but no conclusive evidence was found for the presence of lecticans under cells. The various strategies employed are summarized here:

6.3.3.1 Antibody labeling of CS with CS-56

The anti-chondroitin sulfate antibody, CS-56, was used on fixed RCJ-P and PC3 cells. But there was no significant fluorescent signal visible at the cell-substrate interface. The antibodies were also tested to living cells. The antibodies seemed to be internalized by the cells so the aggregation of the CS-56 outside of cell membrane could not be distinguished from the ones inside the cells. To test our labeling process, PC3 cells were first treated with exogenous ACAN, fixed with formaldehyde, and then incubated with antibodies. Since the fixation process collapsed

the PCM with ACAN, all the CS-56 labeling appeared to be on the glass surface. Still, no fluorescence was visible under the cells.

6.3.3.2 Electrostatic labeling with fluorescently-labeled positive proteins (histones)

In Ch. 4, evidence of fluorescent histone binding to the GAG side chains of the lectican was reported. Histone is a small molecule with a size less than 20 kDa. Fluorescent BSA can access to space under the cells (data not shown) with its size larger than 60 kDa so histone should be able to get under the cell with its small size. However, after incubating RCJ-P cells with fluorescent histone, the aggregation of histone could be seen inside the PCM around the cells but with no sign of histone concentration could be found anywhere under the cells. In hindsight, this result that histone is in the extended PCM but not under the cell, could arise from the surrounding PCM capturing the majority of the histone and leaving little left to diffuse under the cell. A similar effect could occur for the antibodies as well. This should be further investigated.

6.3.3.3 RICM shows topography not flatten after CS digestion

In the RICM microscope used in this work, the range of the interference pattern from dark to bright is about 135 nm. The interference pattern's shade will go from dark, when the cell membrane is in contact with the substrate, to the brightest, when the distance between cell and substrate is about 135 nm, and then go back down to dark again. The average size of a fully extended lectican is about ~80 x 300 nm (or ~200 nm diameter as a globule), which is large in our RICM setting. Even the change of distance on the short side of a single cylindrical CSPG will drastically alter the interference fringes in the RICM images.

In chapter 5, we reported that the ventral topography of cells flattens after HA digestion, and the cell membrane moves further towards the substrate. Comparing to the 94% rate of flattening after HA degradation, degradation of chondroitin sulfate by ChABC flattened the

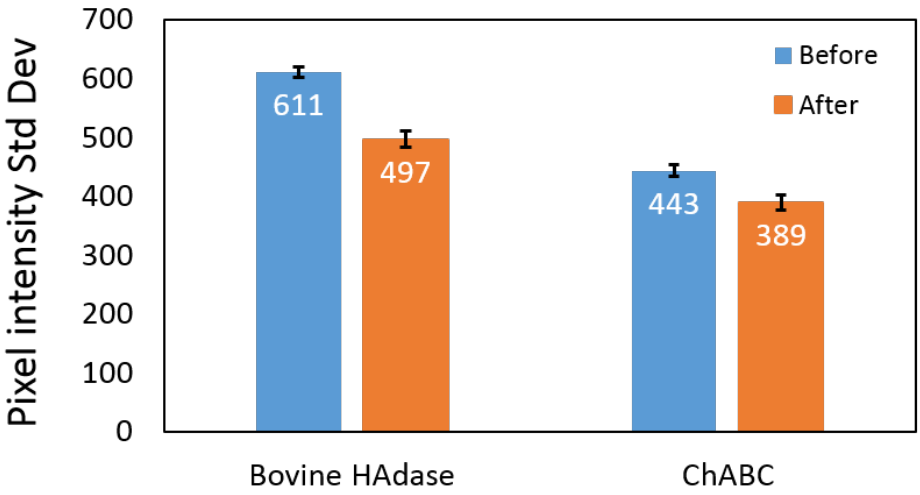

Figure 6.2: The average pixel intensity standard deviation before and after enzyme treatment for 20 minutes on RCJ-P cells. N=44 for HAdase and N=35 for ChABC.

topography only on 1/3 of the 87 RCJ-P cells imaged. The quantitative analysis (method described in section 5.3.3) of the RICM images showed the standard deviation of the pixel intensity histogram before and after ChABC treatment for 20 minutes decreased an average 53.30 from 442.66 ± 9.89 to 389.36 ± 13.31. This is half of the standard deviation decrease from the bovine HAdase treatment, which was 114.13 (see Figure 6.2). It shows that ChABC did smooth out the topography under the cell, but it is not as effectively as the bacterial HAdase. This experiment was performed only on the RCJ-P cell line. These null results of locating lectican under the cells combined with the observation that the majority of cells maintained a similar ventral gap after ChABC treatment, suggests that lectican may not be present under the cells. This is further supported by the observation that the ventral gap decreases rapidly after HA digestion with HAdase; yet if bottlebrushes are present, it would require that the lecticans either rapidly diffuse out from under the cell or else be immediately endocytosed or degraded by the cell. The short time scale makes these prospects unlikely.

6.3.3.4 Indirect evidence: Aggrecanase

To investigate if lectican is under the cells and its effect on cell adhesion, we planned to measure the adhesion strength of cells treated with aggrecanase, ADAM-TS4, which targets and cleaves the protein backbone of the lectican, aggrecan. Although ChABC digesting the side chains of the lectican collapses the PCM around it, it may also impact other non-PCM aspects of the cell, since CS is a common GAG appended during glycosylation of numerous proteins, including for example, CD44.

Digesting the protein backbone with aggrecanase was hence an alternative route to measure the effect of lectican on cell adhesion. However, the functionality of the aggrecanase was not realized despites numerous trials on living cells including RCJ-P and PC3. The thickness of the PCM was not altered after incubation with aggrecanase, an indication of its failure. One possible explanation is that since the cells secret lectican into the media, there might be just too high a lectican concentration around the cells that the aggrecanase could not reach the PCM. However, replacing with fresh media before adding aggrecanase still presented null result. The next thing to do after would be putting the enzyme into exogenous aggrecan solution. A size measurement before and after the enzyme should reveal if the aggrecanase work or not.

6.4 Discussion

6.4.1 CS effect on adhesion also shown in HAdase results

The effect of CS on the adhesion strength might also be reflected in the HAdase experiments. Bovine HAdase, which degrades CS at a higher rate than bacterial HAdase (24), causes a higher adhesion strength increase than the bacterial counterpart. The additional adhesion strength increase might stem from the superior CS degradation rate of the bovine

HAdase because GFPn labeling of the interfacial HA matrix decreased by similar amount (~80% of original intensity) after both HAdase treatments.

6.4.2 PCM composition differences between cell types shown in adhesion change

Now, let's compare the adhesion strength increase between the two cell types, RCJ-P and PC3. On RCJ-P, ChABC increased the adhesion strength more than both bacterial and bovine HAdase for both incubation durations (see table 6.1). The increase by ChABC is close to that of bovine HAdase, within 5% of control adhesion value, but more than three times higher than that of bacterial HAdase. However, on PC3 cells, the adhesion strength increase by ChABC is larger than bacterial HAdase but smaller than bovine HAdase. The trend is consistent in both enzyme incubation durations. The differences between the two cell types could stem from different PCM compositions. RCJ-P has a substantial amount of lectican in the PCM (113), so when the cells are treated with ChABC and bovine HAdase, which both degrade CS more efficiently than bacterial HAdase, the adhesion strength increases more. On the other hand, the lack of lecticans on PC3 cells shown by Ricciardelli and et al. in 2007 provides a possible explanation for the adhesion strength increase by bovine HAdase being higher than that by ChABC (41).

6.4.3 Possible source of interfacial CS on HA receptor

Chondroitin sulfate binds to the HA receptor, CD44 (169). CS side chain modifying invariant chain, which is a non-polymorphic glycoprotein, is also shown to bind directly to CD44, and enhance signaling or adhesion of the cells (170). CD44 is shown to affect cell adhesion by not only binding to the extracellular matrix through HA and ligands, it also mediates signaling of receptors tyrosine kinases. Connected to actin cytoskeleton, signaling from CD44 can propagate through the cell and change its behavior (171). Therefore, the CS digestion facilitated by ChABC

might not be on the interfacial lecticans but on the HA receptors and it altered the cell adhesion via signaling, or some combination of those two effects.

6.5 Conclusion and Outlook

These studies provide quantitative illustration of the adhesion strength change by ChABC enzyme. The cell adhesion strength increases significantly after ChABC enzyme treatment. The source of the adhesion change was speculated to be the presence of large, negatively charged lecticans at the cell-substrate interface and pose a repulsive force to the cells. Various efforts to visualize the presence of lecticans under the cell are documented here, including antibody staining, electrostatic binding with fluorescent histone, investigation of space at the cell-substrate interface, and digestion by aggrecanase, a lectican protein backbone specific enzyme. But no evidence of the lectican presence was confirmed. This suggests that the change in adhesion strength results from digestion of CS elsewhere at the cell interface, likely that on a cell receptor which leads to signaling and change in adhesion. The most likely receptor, identified at this point – based on our limited knowledge so far, is CD44. CD44 is glycosylated with CS and is involved in both HA adhesion as well as actin regulation. Further work is needed to understand the results presented.

Chapter 7

PCM Characterization on Migrating Cell

7.1 Overview

The uneven accumulation of the PCM around cells during migration affecting the cell adhesion has long been an inspiration for our work on quantifying the physical effect on adhesion by the HA polymer matrix. The proposed model of the HA effect on migrating cells is intriguing (42). It hypothesizes that more HA at the trailing edge of the migrating cell reduces the adhesion comparing to the leading edge, which has less HA presence and creates a gradient of adhesion strength to enable the cell to detach at the trailing end, pull itself toward the leading edge and move forward.

As we have made progress on analyzing the simplified scenario of hyaluronan-mediated adhesion, we also began to invest in the preliminary assays for future studies focused on HA mechanics during cell migration. Most notably, we need a system where cell migration can be reproducibly induced under similar conditions such that the PCM around and under the cell can be characterized. To date, only crude particle exclusion assays with red blood cells have been used to depict the asymmetric PCM on migrating cells; hence the data produced using any of the methods introduced here and in the previous work of Louis McLane to characterize the migratory-PCM would incredibly insightful (97).

Two methods were pursued. The first is the classic wound healing assay, which was used to successfully reproduce asymmetric PCM on migratory cells and to, for the first time, label the asymmetric PCM fluorescently. A wound healing assay was used to ensure a directional migration of the cells. Otherwise it is hard to distinguish a migrating cell and it may not have a persistent migration direction. With the tools we have in our lab, we can monitor the PCM location and state

on live cells. Reported here is just our preliminary attempt to study the PCM during cell migration. The next step would be to have a better control on the cell migration, as for example, is the goal of the second approach. The second approach, still under construction and in collaboration with an undergraduate, is to generate reproducible protein gradients on surfaces to induce cell migration (not presented here but listed for completeness).

7.2 Wound healing assay to generate directional cell migration

The wound healing assay is one of the earliest developed methods to study directional cell migration *in vitro* (172). This method mimics the cell migration to close the wound *in vivo* by creating an artificial wound in cell layers. RCJ-P cells were first grown for about 48 hours to confluency on cover glass to form a monolayer of cells. A gap was then scratched by the tip of a pipette tip. Different sizes of pipette tip can be used to create different sizes of gaps. The cells were then incubated with the complete culture media in the stage-top incubator controlling the temperature at 37°C and CO_2 level at 5% and imaged for the next 12 – 24 hours around the gap. Automated stage was used to image multiple locations at a fixed rate over the period. Lamp was turned off when camera was idle to minimize the phototoxicity damage of the cells.

The cells migrated collectively. At the edge of the gap, whole lines of cells migrated toward the center of the gap together. Although there were some cells moved faster and protrude out of the pack, the majority of the cell closed the gap at similar rate. The migration was prominent for the first 12 hours, and then the cells were more or less rocking around the same position. The progression of the cell front stopped. It wasn't until more culture media was added in, the cells began to migrate toward the gap center again. The second round of migration stopped after about 10 hours of movement. It could be that the confluent cells, which is double the confluency in my

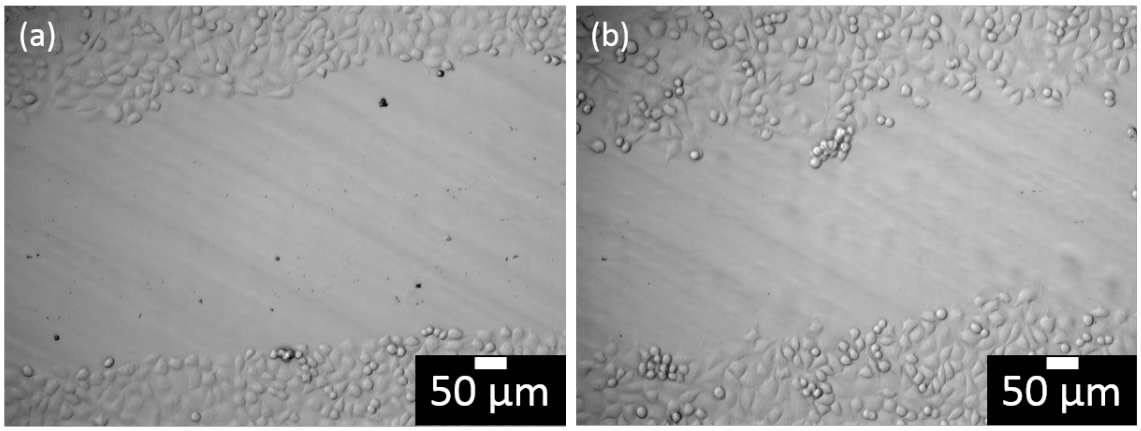

Figure 7.1: (a) RCJ-P wound healing assay at 0 hours (b) RCJ-P wound healing assay at 24 hours.

usual experiments, used up all the nutrients in the solution and stopped migration. After the fresh media and more nutrient were in the surrounding, cells continued to migrate again.

From past experience, phototoxicity prevents cells from proliferating. However, in our setting that turns off the lamp between imaging and images total of 12 positions every 20 minutes for about 2.5 seconds at a time, the cells were healthy and dividing. Not only the cells divided at the edge of the gap, where there was more room, they also divided among the tightly packed region. From the regions imaged, similar proliferation rates were observed at the edge of the gap or in the confluent areas.

7.3 Asymmetric PCM on migrating cells

GFPn was used to visualize the PCM around cells. 22 hours after the creation of the wound, GFPn was then added to the culture media for imaging on confocal microscope with on-stage incubator monitoring the condition to be kept at 37°C and 5% CO_2.

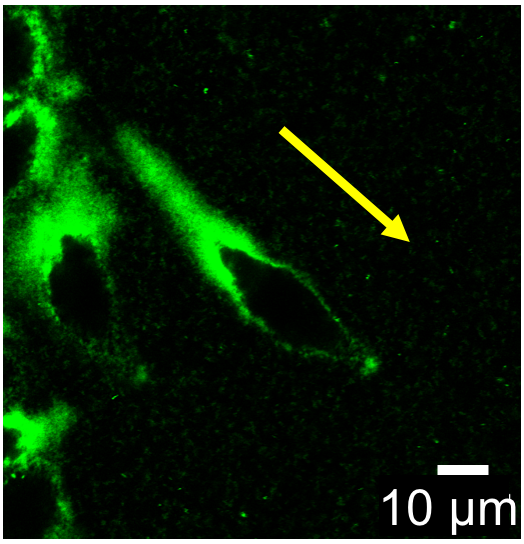

Figure 7.2: GFPn labeled asymmetric HA on migrating RCJ-P, 3 µm above glass. Cell migrating towards lower right corner, as indicated with yellow arrow, showing more HA accumulation at the trailing edge of cell.

On the individual cells that broke out of the collective cell formation, the PCM can be imaged without interference from other cells. For those cells, we were able to confirm for the first time in the Curtis lab that the PCM distribution on migrating cells is asymmetric. Knowing the direction of the cell migration with wound healing assay, we can point out that more HA accumulation appears at the rear end of the cells and less HA at the leading edge of the migrating cell, which is comparable to the finding reported by Evanko, et al (42) and a few other (not many) reports (173, 174)(Figure 7.2). In Ch.5, we reported that there is a spatial correlation of focal adhesions with the gaps between HA patches under the cell. In Figure 7.3b, there were more gaps between HA patches at the leading edge of the migrating cells than the rear end. The indirect evidence showed more and larger FA appear at the direction of migration under the cells, consistent with established measurements.

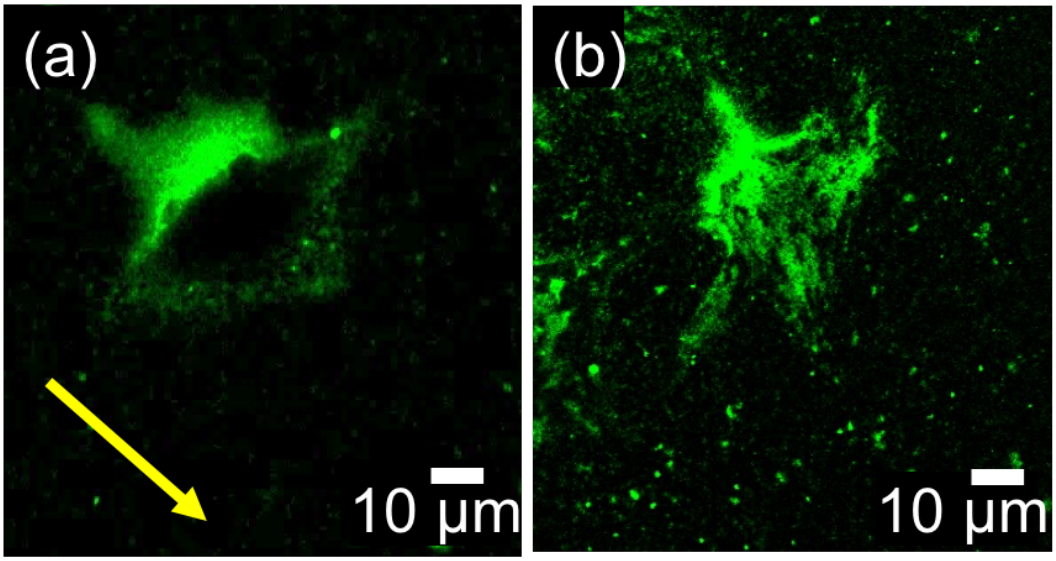

Figure 7.3: (a) GFPn labeled asymmetric HA on migrating RCJ-P cell, 3 μm above glass. Cell migrating towards lower right corner, as indicated with yellow arrow. (b) GFPn labeled HA under the same migrating cell showing more gaps between HA patches at the leading edge of cell.

7.4 Conclusion and Outlook

We have used wound healing assay to initiate and loosely control the direction of cell migration. This enabled us to examine the distribution of HA on the cell surface for the first time using a fluorescent label. Combining the two observations, accumulation of PCM at the trailing edge while more FA presence at the leading edge of the migration cells, we have provided visual evidence for the hypothesis that cells utilize various amount of HA to facilitate a gradient of adhesion strength to the substrate during cell migration.

Developing methods to better control the cell migration are currently being investigated, and will help provide a cleaner experiment and a higher result throughput. Our belief is that the above results combined with our studies on the impact of HA matrix on adhesion will bring about a better understanding of the ways HA is responsible as a partner in the cell migration process.

Chapter 8

Conclusion and Outlook

Pericellular matrix (PCM) has been neglected despite its apparently crucial role in many physiological processes. In this work, we developed novel biophysical tools to improve the examination of the PCM microstructure. The nondestructive technique, qPEA, provides the first quantitative evidence of the pore size in the PCM varies with the distance to cell surface. The passivated fluorescent microspheres of the qPEA demonstrates that even without the electrostatic repulsion or chemical interactions that are expected to occur in the highly negatively charged matrix due to bottlebrush CSPGs, access to the cell surface is affected by the cell coat microstructure. This has direct implications for cell defense against viral and bacterial infections, exosome biology, and drug delivery applications.

We demonstrated that the accessibility of the cell can be modified with exogenous bottlebrush CSPGs. Studies shown in chapter 4 provide quantitative illustrations of how changes in bottlebrush proteoglycan concentration in the PCM can affect the transport of nanoparticles to the cell surface as well as the sequestration of positively charged molecules. Fluorescent labeling of the bottlebrush proteoglycans shows that diffusion of the bottlebrushes themselves still occurs through saturated pericellular matrix despite the sizable dimensions of the molecule and its negative charge. Evidence for the sparse population of native bottlebrushes points to the possibility for cells to use surface-tethered proteoglycans to control native cell surface accessibility or to concentrate and sequester biomolecules like growth factors. Mechanics could be altered this way as well. For the cell types studied in this research, a special regime exists where the PCM appears fully stretched, but the porosity and molecular interactions can be tuned significantly by varying the exogenous aggrecan solution concentration between 180-333 μg/mL.

In Chapters 5 and 6, we tested the hypothesis that HA-rich pericellular matrix plays an mechanical role in orchestrating the cell adhesion, which is crucial in many physiological processes including cell migration and proliferation. Although there are many other areas of study in cell adhesion, such as signaling pathway and focal adhesion (FA) structure, the role of the long sugar polymer matrix at the interface of cell and adhesion substrate can be not ignored (88). In this work we provide evidence of the spatial anti-correlation of FA and the interfacial HA matrix and show those HA matrix creates uneven topography under cells. Previous studies showed that the distance created by 'bulky polysaccharides' can decrease the receptor-ligand interaction by altering kinetics (175, 176). We examined a complementary route by which hyaluronan could impact cell adhesion, namely that the interfacial HA matrix exerts a direct repulsive force between the cell and substrate, weakening the adhesion of the cell to the substrate. Using the hydrodynamic spinning disk apparatus, we quantitatively documented the impact on the adhesion strength of RCJ-P and PC3 cells before and after HA matrix degradation. After HAdase or ChABC enzymes treatments, the adhesion strength of cells with HA matrix increased significantly, while cells without HA matrix remain the same. This result demonstrated the adhesion strength increase is result from HA removal and not an artifact caused by the enzyme. However, the mechanism of the adhesion strength alteration by the HA matrix is still unclear. Our analysis is based on several assumptions we tried to address in the chapters, but the repulsive interfacial HA matrix hypothesis still needs to be examined further.

In addition, we combine a convenient and popular method, wound healing assay, with our techniques to provide the first direct visualization of the asymmetric hyaluronan distribution of the PCM around migrating cells. Our work provides the visual evidence for the hypothesis that cells utilize various amount of HA to facilitate a gradient of adhesion strength to the substrate during cell migration.

Our efforts in the lab throughout the duration of this thesis have been focused on characterizing the physical impact of PCM on the two most obvious possible processes that the cell coat might have (i) passage of objects to and from the surface and (ii) the mechanics of cell adhesion. As summarized above, we have made some good progress in a widely uncharted territory. Moving forward, there is much to do and as we have become more familiar and experienced with the biology of a structure that few appreciate exists; and as we have developed tools to study the PCM, we are now in the exciting position to make significant headway. The topics to be pursued are numerous. Each thread of investigation listed below has some fundamental biophysical research question related combined with an important question or application in biology, medicine or bioengineering.

We have some immediate follow-up for the work presented in this thesis. In chapter 4, we demonstrated that the small and positively charged molecule, histone, concentrated and attached to the CSPG. Our work with histone was a proof of principle showing that PCM can sequester positive charged molecules. Since the main goal has always been studying the sequestration of growth factor inside PCM, immediately relevant are follow up studies examining growth factor sequestration to the PCM, investigation of its release, and its possible effects on cell. For example, after fluorescently labeling the BMP-2, looking at whether the growth factor is sequestered and concentrated to high enough concentrations to drive differentiation of stem cells would be an excellent example of how PCM can be utilized by cells as a molecular reservoir.

In chapter 5 and chapter 6, depleting the interfacial HA and CS increases the cell adhesion strength. The enzyme treatment is not the ideal treatment to study the mechanical effect of HA matrix on adhesion because of its various possible side effects discussed in the chapters. An improved method to control the HA presence is varying the expression level of HA synthases (HAS). We will use a well-established method by our collaborator Dr. Heldin, who agreed to share her adenovirus constructs and expertise to up-regulate the expression of HAS. We can also down-

regulate HAS using siRNA following protocols developed and tested in Dr. Heldin's lab (80). Comparing the adhesion strength of the increased amount of HA synthesis with the control cells can cleanly distinguish the mechanical effect of the HA matrix on adhesion events.

While our work presented here was performed on different cell types, mainly on rat's chondrocytes and human prostate cancer cells, we still want to broaden our base and bring our research to other related cell lines. Human breast cancer cell, Hs578T, is our target for its impact on human disease well-being. The advantage of this cell line also includes its popularity and the many researches related to hyaluronan have been done (58, 80, 177–179). As mentioned previously, we have started the preliminary investigation for characterization of the PCM with PEA, showing that an average thickness of 5.79 ± 0.74 μm (N=41) in chapter 3.3.1. Fluorescent paxillin transfection has also been done on the breast cancer cell showing spatial anti-correlation between the interfacial HA and FAs (Figure 5.5). However, to move on to the next step of quantitative adhesion strength measurement by spinning disk apparatus, we need to device micropatterned surfaces to control the irregular cell shape for the quality insurance of the adhesion strength measurement. We have started putting together micro-contact printing method (180). The procedure involves making PDMS stamps with positive micropatterns of our choosing with protein attached, transferring the patterned protein onto cover glass and then passivating the un-patterned surfaces with polyethylene glycol compound to prevent cell attachment to the un-patterned locations. The stamps have been made but the patterning process suitable for cell adhesion is still under optimization. After the optimization is done, adhesion strength of the breast cancer cells with various HA matrix conditions can be measured with a well-controlled cell shape and area.

Another direct follow up for the work presented in this thesis is the cell migration presented in chapter 7. The wound healing assay can incentivize the cells to migrate in a certain direction and is widely used (181–183), but that is not well fitted for our purpose to investigate the local

PCM status during migration because of the concerted movement of the cells during such assay. It was hard to study PCM on individual cell because they are packed close together. Other methods are considered including microfluidic (184), chemotaxis (185), and the one currently being pursued in our lab, a gradient of ligand concentration driving the cells toward more concentrated area. A more controlled cell migration can potentially allow us to monitor the PCM during migration on single cells and elucidate its effect.

One of our recent related work on cell adhesion has been done in collaboration with Dr. Salaita in Emory University. The Salaita group created a protein based molecular tension sensor to measure the tension on individual integrin bond (186). A changeable spring-like molecule connects integrin binding ligand with a fluorescent dye to a nano-particle fluorescence quencher bound to the substrate. When relaxed, the fluorescent dye is close to the nano-particle and the fluorescent intensity is low undergoing resonance energy transfer (RET). After cell attaching to the ligand on the other end of the sensor stretches the spring-like molecule, the distance between the dye and quencher increases to produce higher fluorescent intensity. The fluorescent intensity varies with the distance between the dye and the nano-particle quencher on the surface denoting the different tension on the integrin. Molecules with various stiffness can be used as the probe of the tension sensor.

In our preliminary experiment, different molecules were tested with the cell lines studied, including the 27^{th} immunoglobulin domain of cardiac titin proteins, DNA hairpin and polyethylene glycol (PEG) polymer. The most probable unfolding force for the probes are ~80-200 pN for the titin sensor, ~4-50 pN for DNA denaturation and ~2-6 pN with the polymer probe stretching. Trials with the RCJ-P and PC3 cells even on the polymer probe showed the contraction force was too weak to produce significant fluorescent signal from the sensor. The breast cancer cell, Hs578T, was used to monitor the adhesion molecular tension before and after HA matrix removal because

the cell line is strong enough to denature the strongest titin sensor and exhibit clear signal from the tension sensor.

Our preliminary experiment showed the average fluorescent intensity from the sensor decreases by about 10% (N=14) after bacterial HAdase digested the HA matrix on the breast cancer cell, Hs578T. One would naively think that means the tension on the integrin bonds is smaller after the HA matrix depletion, which corresponds to our theory that interfacial HA exerts a repulsive force between cell and substrate. The detail experimental setup and account will be in Appendix A. However, more studies need to be done before conclusion is made.

The goal of this work was to study the structure and mechanics of the pericellular matrix using various biophysical tools. The insights gained into the PCM microstructure build the knowledge base for future studies on the matrix and a wide variety of the physiological processes the matrix influence. A tighter focus of the effect of PCM on the adhesion events provides an alternative direction for the elucidation of the matrix mechanics complementing the signal pathway approach. We hope our work will inspire further discoveries on the PCM and help improve the health and disease research on human kind.

REFERENCES

1. Marcellin, E., J.A. Steen, and L.K. Nielsen. 2014. Insight into hyaluronic acid molecular weight control. Appl. Microbiol. Biotechnol. 98: 6947–6956.
2. Tran, D., M. Golick, H. Rabinovitz, D. Rivlin, G. Elgart, et al. 2000. Hematoxylin and safranin O staining of frozen sections. Dermatol. Surg. 26: 197–9.
3. Toole, B.P. 1997. Hyaluronan in morphogenesis. J. Intern. Med. 242: 35–40.
4. Laurent, T. 1992. Hyaluronan. FASEB J. 6: 2397–2404.
5. Burd, D.A.R., M. Ritz, S. Regauer, M.T. Longaker, J.W. Siebert, et al. 1991. Hyaluronan and wound healing: a new perspective. Br. J. Plast. Surg. 44: 579–584.
6. Chen, W.Y.J., and G. Abatangelo. 1999. Functions of hyaluronan in wound repair. Wound Repair Regen. 7: 79–89.
7. Camenisch, T.D., A.P. Spicer, T. Brehm-Gibson, J. Biesterfeldt, M. Lou Augustine, et al. 2000. Disruption of hyaluronan synthase-2 abrogates normal cardiac morphogenesis and hyaluronan-mediated transformation of epithelium to mesenchyme. J. Clin. Invest. 106: 349–360.
8. Toole, B.P. 2001. Hyaluronan in morphogenesis. Semin. Cell Dev. Biol. 12: 79–87.
9. Gibbs, D.A., E.W. Merrill, K.A. Smith, and E.A. Balazs. 1968. Rheology of hyaluronic acid. Biopolymers. 6: 777–791.
10. Ogston, A.G., and J.E. Stanier. 1953. The physiological function of hyaluronic acid in synovial fluid; viscous, elastic and lubricant properties. J. Physiol. 119: 244.
11. Chong, B.F., L.M. Blank, R. Mclaughlin, and L.K. Nielsen. 2005. Microbial hyaluronic acid production. Appl. Microbiol. Biotechnol. 66: 341–351.
12. Wight, T.N. 1996. The vascular extracellular matrix. Atheroscler. Coron. artery Dis. Philadelphia Lippincott-Raven. 1: 421–440.
13. Toole, B.P. 2004. Hyaluronan: from extracellular glue to pericellular cue. Nat Rev Cancer. 4: 528–539.
14. Evanko, S.P., M. Tammi, R. Tammi, and T. Wight. 2007. Hyaluronan-dependent pericellular matrix. Adv. Drug Deliv. Rev. 59: 1351–1365.
15. Pyka, M., C. Wetzel, A. Aguado, M. Geissler, H. Hatt, et al. 2011. Chondroitin sulfate proteoglycans regulate astrocyte-dependent synaptogenesis and modulate synaptic activity in primary embryonic hippocampal neurons. Eur. J. Neurosci. 33: 2187–2202.
16. Ghazarian, H., B. Idoni, and S.B. Oppenheimer. 2011. A glycobiology review: carbohydrates, lectins and implications in cancer therapeutics. Acta Histochem. 113: 236–247.
17. Karlsson, K.-A. 1991. Glycobiology: a growing field for drug design. Trends Pharmacol. Sci. 12: 265–272.
18. Spagnoli, C., A. Korniakov, A. Ulman, E.A. Balazs, Y.L. Lyubchenko, et al. 2005.

Hyaluronan conformations on surfaces: effect of surface charge and hydrophobicity. Carbohydr. Res. 340: 929–941.

19. Laurent, T.C. 1987. Biochemistry of Hyaluronan. Acta Otolaryngol. 104: 7–24.

20. Mendichi, R., Š. Ladislav, and A.G. Schieroni. 2003. Evaluation of Radius of Gyration and Intrinsic Viscosity Molar Mass Dependence and Stiffness of Hyaluronan. .

21. Balazs, E.A. 1974. The Physical Properties of Synovial Fluid and the Special Role of Hyaluronic Acid. Disord. Knee. : 63–75.

22. Weigel, P.H. 2002. Functional Characteristics and Catalytic Mechanisms of the Bacterial Hyaluronan Synthases. IUBMB Life (International Union Biochem. Mol. Biol. Life). 54: 201–211.

23. Jiang, D., J. Liang, and P.W. Noble. 2011. Hyaluronan as an immune regulator in human diseases. Physiol. Rev. 91: 221–264.

24. Stern, R., and M.J. Jedrzejas. 2006. Hyaluronidases: Their genomics, structures, and mechanisms of action. Chem. Rev. 106: 818–839.

25. Hardingham, T. 1981. Proteoglycans: their structure, interactions and molecular organization in cartilage. Biochem. Soc. Trans. 9: 489–97.

26. Rhodes, K.E., and J.W. Fawcett. 2004. Chondroitin sulphate proteoglycans: Preventing plasticity or protecting the CNS? J. Anat. 204: 33–48.

27. Doege, K.J., M. Sasaki, T. Kimura, and Y. Yamada. 1991. Complete coding sequence and deduced primary structure of the human cartilage large aggregating proteoglycan, aggrecan. Human-specific repeats, and additional alternatively spliced forms. J. Biol. Chem. 266: 894–902.

28. Wight, T.N., and M.J. Merrilees. 2004. Proteoglycans in atherosclerosis and restenosis: key roles for versican. Circ. Res. 94: 1158–67.

29. Yamaguchi, Y. 2000. Lecticans: organizers of the brain extracellular matrix. C. Cell. Mol. Life Sci. 57: 276–289.

30. Knudson, W., and C.B. Kundson. 1991. Assembly of a chondrocyte-like pericellular matrix on non-chondrogenic cells. Role of the cell surface hyaluronan receptors in the assembly of a pericellular matrix. J Cell Sci. 99: 227–235.

31. Wu, Y.J., D.P. La Pierre, J. Wu, A.J. Yee, and B.B. Yang. 2005. The interaction of versican with its binding partners. www.cell-research.com | Cell Res. 15: 483–494.

32. Schmidt, G., H. Hausser, and H. Kresse. 1991. Interaction of the small proteoglycan decorin with fibronectin. Involvement of the sequence NKISK of the core protein. Biochem. J. 280.

33. Bidanset, D.J., C. Guidry, L.C. Rosenberg, H.U. Choi, R. Timpl, et al. 1992. Binding of the proteoglycan decorin to collagen type VI. J. Biol. Chem. 267: 5250–6.

34. Hedbom, E., and D. Heinegård. 1993. Binding of fibromodulin and decorin to separate sites on fibrillar collagens. J. Biol. Chem. 268: 27307–12.

35. Macri, L., D. Silverstein, and R.A.F. Clark. 2007. Growth factor binding to the pericellular matrix and its importance in tissue engineering. Adv. Drug Deliv. Rev. 59: 1366–1381.

36. Avnur, Z., and B. Geiger. 1984. Immunocytochemical localization of native chondroitin-sulfate in tissues and cultured cells using specific monoclonal antibody. Cell. 38: 811–822.

37. Yamagata, M., S. Saga, M. Kato, M. Bernfield, and K. Kimata. 1993. Selective distributions of proteoglycans and their ligands in pericellular matrix of cultured fibroblasts. Implications for their roles in cell-substratum adhesion. J. Cell Sci. 106 (Pt 1: 55–65.

38. Rilla, K., M.J. Lammi, R. Sironen, K. Törrönen, M. Luukkonen, et al. 2002. Changed lamellipodial extension, adhesion plaques and migration in epidermal keratinocytes containing constitutively expressed sense and antisense hyaluronan synthase 2 (Has2) genes. J. Cell Sci. 115: 3633–3643.

39. Cohen, M., Z. Kam, L. Addadi, B. Geiger, A. Albersdorfer, et al. 2006. Dynamic study of the transition from hyaluronan- to integrin-mediated adhesion in chondrocytes. EMBO J. 25: 302–11.

40. Clarris, B.J., and J.R.E. Fraser. 1968. On the pericellular zone of some mammalian cells in vitro. In: Experimental Cell Research. . pp. 181–193.

41. Ricciardelli, C., D.L. Russell, M.P. Ween, K. Mayne, S. Suwiwat, et al. 2007. Formation of Hyaluronan- and Versican-rich Pericellular Matrix by Prostate Cancer Cells Promotes Cell Motility. J. Biol. Chem. 282: 10814–10825.

42. Evanko, S.P., J.C. Angello, and T.N. Wight. 1999. Formation of Hyaluronan- and Versican-Rich Pericellular Matrix Is Required for Proliferation and Migration of Vascular Smooth Muscle Cells. Arter. Thromb Vasc Biol. 19.

43. Heldin, P., and H. Pertoft. 1993. Synthesis and Assembly of the Hyaluronan-Containing Coats around Normal Human Mesothelial Cells. Exp. Cell Res. 208: 422–429.

44. Ween, M.P., K. Hummitzsch, R.J. Rodgers, M.K. Oehler, and C. Ricciardelli. 2011. Versican induces a pro-metastatic ovarian cancer cell behavior which can be inhibited by small hyaluronan oligosaccharides. Clin. Exp. Metastasis. 28: 113–25.

45. Nishida, Y., C.B. Knudson, W. Eger, K.E. Kuettner, and W. Knudson. 2000. Osteogenic protein 1 stimulates cell-associated matrix assembly by normal human articular chondrocytes: Up-regulation of hyaluronan synthase, CD44, and aggrecan. Arthritis Rheum. 43: 9.

46. Hascall, V.C., A.K. Majors, C. a De La Motte, S.P. Evanko, A. Wang, et al. 2004. Intracellular hyaluronan: a new frontier for inflammation? Biochim. Biophys. Acta. 1673: 3–12.

47. Maroudas, A., J. Mizrahi, E.P. Katz, E.J. Wachtel, and M. Soudry. 1986. Physicochemical properties and functional behavior of normal and osteoarthritic human cartilage. Articul. Cartil. Biochem. 1: 311–330.

48. Yu, M., S. Jambhrunkar, P. Thorn, J. Chen, W. Gu, et al. 2013. Hyaluronic acid modified mesoporous silica nanoparticles for targeted drug delivery to CD44-overexpressing cancer cells. Nanoscale. 5: 178–83.

49. Duchesne, L., V. Octeau, R. Bearon, and A. Beckett. 2012. Transport of fibroblast growth factor 2 in the pericellular matrix is controlled by the spatial distribution of its binding sites in heparan sulfate. PLoS Biol. 10.

50. Bourguignon, L.Y.W., H. Zhu, A. Chu, N. Iida, L. Zhang, et al. 1997. Interaction between

the adhesion receptor, CD44, and the oncogene product, p185 HER2, promotes human ovarian tumor cell activation. J. Biol. Chem. 272: 27913–27918.

51. Oliferenko, S., I. Kaverina, J.V. Small, and L.A. Huber. 2000. Hyaluronic acid (HA) binding to CD44 activates Rac1 and induces lamellipodia outgrowth. J. Cell Biol. 148: 1159–1164.

52. Bourguignon, L.Y.W. 2000. CD44 Interaction with Tiam1 Promotes Rac1 Signaling and Hyaluronic Acid-mediated Breast Tumor Cell Migration. J. Biol. Chem. 275: 1829–1838.

53. Savani, R.C., C. Wang, B. Yang, S. Zhang, M.G. Kinsella, et al. 1995. Migration of bovine aortic smooth muscle cells after wounding injury. The role of hyaluronan and RHAMM. J. Clin. Invest. 95: 1158.

54. Gardner, D.K., H. Rodriegez-Martinez, and M. Lane. 1999. Fetal development after transfer is increased by replacing protein with the glycosaminoglycan hyaluronan for mouse embryo culture and transfer. Hum. Reprod. 14: 2575–2580.

55. Alexopoulos, L.G., G.M. Williams, M.L. Upton, L.A. Setton, and F. Guilak. 2005. Osteoarthritic changes in the biphasic mechanical properties of the chondrocyte pericellular matrix in articular cartilage. J. Biomech. 38: 509–517.

56. Itano, N., T. Sawai, O. Miyaishi, and K. Kimata. 1999. Relationship between hyaluronan production and metastatic potential of mouse mammary carcinoma cells. Cancer Res. 59: 2499–2504.

57. Stamenkovic, I. 2000. Matrix metalloproteinases in tumor invasion and metastasis. In: Seminars in cancer biology. . pp. 415–433.

58. Herrera-Gayol, a, and S. Jothy. 1999. CD44 modulates Hs578T human breast cancer cell adhesion, migration, and invasiveness. Exp. Mol. Pathol. 66: 99–108.

59. Tian, X., J. Azpurua, C. Hine, A. Vaidya, M. Myakishev-Rempel, et al. 2013. High-molecular-mass hyaluronan mediates the cancer resistance of the naked mole rat. Nature. 499: 346–349.

60. Han, Y., S.C. Cowin, M.B. Schaffler, and S. Weinbaum. 2004. Mechanotransduction and strain amplification in osteocyte cell processes. Proc. Natl. Acad. Sci. U. S. A. 101: 16689–16694.

61. Vincent, T.L., C.J. McLean, L.E. Full, D. Peston, and J. Saklatvala. 2007. FGF-2 is bound to perlecan in the pericellular matrix of articular cartilage, where it acts as a chondrocyte mechanotransducer. Osteoarthr. Cartil. 15: 752–763.

62. Henry, C.B., and B.R. Duling. 1999. Permeation of the luminal capillary glycocalyx is determined by hyaluronan. Am. J. Physiol. 277: H508–H514.

63. Lieleg, O., R.M. Baumgartel, and A.R. Bausch. 2009. Selective Filtering of Particles by the Extracellular Matrix: An Electrostatic Bandpass. Biophys. J. 97: 1569–1577.

64. Zhou, R., H. Zhou, B. Xiong, Y. He, and E.S. Yeung. 2012. Pericellular Matrix Enhances Retention and Cellular Uptake of Nanoparticles. J. Am. Chem. Soc. .

65. Cohen, M., D. Joester, B. Geiger, and L. Addadi. 2004. Spatial and temporal sequence of events in cell adhesion: from molecular recognition to focal adhesion assembly. Chembiochem. 5: 1393–9.

66. Zamir, E., and B. Geiger. 2001. Molecular complexity and dynamics of cell-matrix

adhesions. J. Cell Sci. 114: 3583–3590.

67. Balaban, N.Q., U.S. Schwarz, D. Riveline, P. Goichberg, G. Tzur, et al. 2001. Force and focal adhesion assembly: a close relationship studied using elastic micropatterned substrates. Nat. Cell Biol. 3: 466–472.

68. Ballestrem, C., B. Hinz, B.A. Imhof, and B. Wehrle-Haller. 2001. Marching at the front and dragging behind differential $α$V$β$3-integrin turnover regulates focal adhesion behavior. J. Cell Biol. 155: 1319–1332.

69. Holt, M.R., Y. Calle, D.H. Sutton, D.R. Critchley, G.E. Jones, et al. 2008. Quantifying cell--matrix adhesion dynamics in living cells using interference reflection microscopy. J. Microsc. 232: 73–81.

70. Rid, R., N. Schiefermeier, I. Grigoriev, J.V. Small, and I. Kaverina. 2005. The last but not the least: the origin and significance of trailing adhesions in fibroblastic cells. Cell Motil. Cytoskeleton. 61: 161–171.

71. Zamir, E., M. Katz, Y. Posen, N. Erez, K.M. Yamada, et al. 2000. Dynamics and segregation of cell--matrix adhesions in cultured fibroblasts. Nat. Cell Biol. 2: 191–196.

72. Zaidel-Bar, R., M. Cohen, L. Addadi, and B. Geiger. 2004. Hierarchical assembly of cell--matrix adhesion complexes. Biochem. Soc. Trans. 32: 416–420.

73. Gardel, M.L., B. Sabass, L. Ji, G. Danuser, U.S. Schwarz, et al. 2008. Traction stress in focal adhesions correlates biphasically with actin retrograde fl ow speed. J. Cell Biol. 183: 999–1005.

74. Jones, M.C., P.T. Caswell, and J.C. Norman. 2006. Endocytic recycling pathways: emerging regulators of cell migration. Curr. Opin. Cell Biol. 18: 549–557.

75. Huttenlocher, A., S.P. Palecek, Q. Lu, W. Zhang, R.L. Mellgren, et al. 1997. Regulation of cell migration by the calcium-dependent protease calpain. J. Biol. Chem. 272: 32719–32722.

76. Itano, N., F. Atsumi, T. Sawai, Y. Yamada, O. Miyaishi, et al. 2002. Abnormal accumulation of hyaluronan matrix diminishes contact inhibition of cell growth and promotes cell migration. Proc. Natl. Acad. Sci. U. S. A. 99: 3609–3614.

77. Schmidt, E.P., Y. Yang, W.J. Janssen, A. Gandjeva, M.J. Perez, et al. 2012. The pulmonary endothelial glycalyx regulates neutrophil adhesion and lung injury during experimental sepsis. Nat Med. 18: 1–20.

78. Heldin, P., M. Suzuki, P. Teder, and H. Pertoft. 1995. Chondroitin sulfate proteoglycan modulates the permeability of hyaluronan-containing coats around normal human mesothelial cells. J. Cell. Physiol. 165: 54–61.

79. Kultti, A., S. Pasonen-Seppänen, M. Jauhiainen, K.J. Rilla, R. Kärnä, et al. 2009. 4-Methylumbelliferone inhibits hyaluronan synthesis by depletion of cellular UDP-glucuronic acid and downregulation of hyaluronan synthase 2 and 3. Exp. Cell Res. 315: 1914–23.

80. Li, Y., L. Li, T.J. Brown, and P. Heldin. 2007. Silencing of hyaluronan synthase 2 suppresses the malignant phenotype of invasive breast cancer cells. Int. J. Cancer. 120: 2557–2567.

81. Liu, N., F. Gao, Z. Han, X. Xu, C.B. Underhill, et al. 2001. Hyaluronan synthase 3

overexpression promotes the growth of TSU prostate cancer cells. Cancer Res. 61: 5207–5214.

82. Misra, S., P. Heldin, V.C. Hascall, N.K. Karamanos, S.S. Skandalis, et al. 2011. Hyaluronan-CD44 interactions as potential targets for cancer therapy. FEBS J. 278: 1429–43.

83. Aya, K.L., and R. Stern. 2014. Hyaluronan in wound healing: rediscovering a major player. Wound Repair Regen. 22: 579–93.

84. Fotia, C., G.M. Messina, G. Marletta, N. Baldini, and G. Ciapetti. 2013. Hyaluronan-based pericellular matrix: substrate electrostatic charges and early cell adhesion events. Eur. Cell. Mater. 26: 133–49.

85. Hall, C.L., C. Wang, L.A. Lange, and E.A. Turley. 1994. Hyaluronan and the hyaluronan receptor RHAMM promote focal adhesion turnover and transient tyrosine kinase activity. J. Cell Biol. 126: 575–588.

86. Kim, Y., Y.-S. Lee, J. Choe, H. Lee, Y.-M. Kim, et al. 2008. CD44-epidermal growth factor receptor interaction mediates hyaluronic acid-promoted cell motility by activating protein kinase C signaling involving Akt, Rac1, Phox, reactive oxygen species, focal adhesion kinase, and MMP-2. J. Biol. Chem. 283: 22513–22528.

87. Twarock, S., M.I. Tammi, R.C. Savani, and J.W. Fischer. 2010. Hyaluronan stabilizes focal adhesions, filopodia, and the proliferative phenotype in esophageal squamous carcinoma cells. J. Biol. Chem. 285: 23276–23284.

88. Paszek, M.J., C.C. DuFort, O. Rossier, R. Bainer, J.K. Mouw, et al. 2014. The cancer glycocalyx mechanically primes integrin-mediated growth and survival. Nature. 511: 319–25.

89. Gardel, M.L., I.C. Schneider, Y. Aratyn-Schaus, and C.M. Waterman. 2010. Mechanical integration of actin and adhesion dynamics in cell migration. Annu. Rev. Cell Dev. Biol. 26: 315.

90. Riveline, D., E. Zamir, N.Q. Balaban, U.S. Schwarz, T. Ishizaki, et al. 2001. Focal contacts as mechanosensors externally applied local mechanical force induces growth of focal contacts by an mdia1-dependent and rock-independent mechanism. J. Cell Biol. 153: 1175–1186.

91. Goffin, J.M., P. Pittet, G. Csucs, J.W. Lussi, J.-J. Meister, et al. 2006. Focal adhesion size controls tension-dependent recruitment of $α$-smooth muscle actin to stress fibers. J. Cell Biol. 172: 259–268.

92. Tan, J.L., J. Tien, D.M. Pirone, D.S. Gray, K. Bhadriraju, et al. 2003. Cells lying on a bed of microneedles: an approach to isolate mechanical force. Proc. Natl. Acad. Sci. 100: 1484–1489.

93. Stricker, J., Y. Aratyn-Schaus, P.W. Oakes, and M.L. Gardel. 2011. Spatiotemporal constraints on the force-dependent growth of focal adhesions. Biophys. J. 100: 2883–2893.

94. Clarris, B.J., J.R. Fraser, and S. Rodda. 1974. Effect of cell-bound hyaluronic acid on infectivity of Newcastle disease virus for human synovial cells in vitro. Ann. Rheum. Dis. 33: 240.

95. Itano, N. 1999. Three Isoforms of Mammalian Hyaluronan Synthases Have Distinct

Enzymatic Properties. J. Biol. Chem. 274: 25085–25092.

96. Zhang, H., S.L. Baader, M. Sixt, J. Kappler, and U. Rauch. 2004. Neurocan-GFP fusion protein: a new approach to detect hyaluronan on tissue sections and living cells. J. Histochem. Cytochem. 52: 915–22.

97. McLane, L.T., P. Chang, A. Granqvist, H. Boehm, A. Kramer, et al. 2013. Spatial Organization and Mechanical Properties of the Pericellular Matrix on Chondrocytes. Biophys. J. 104: 986–996.

98. Chang, P.S., L.T. McLane, R. Fogg, J. Scrimgeour, J.S. Temenoff, et al. 2016. Cell Surface Access Is Modulated by Tethered Bottlebrush Proteoglycans. Biophys. J. 110: 2739–2750.

99. Kim, A.J., V.N. Manoharan, and J.C. Crocker. 2005. Swelling-Based Method for Preparing Stable, Functionalized Polymer Colloids. J. Am. Chem. Soc. 127: 1592–1593.

100. Valentine, M.T., Z.E. Perlman, M.L. Gardel, J.H. Shin, P. Matsudaira, et al. 2004. Colloid Surface Chemistry Critically Affects Multiple Particle Tracking Measurements of Biomaterials. Biophys. J. 86: 4004–4014.

101. Scrimgeour, J., J.K. Cho, V. Breedveld, and J. Curtis. 2011. Microfluidic dialysis cell for characterization of macromolecule interactions. Soft Matter. 7: 4762.

102. Crocker, J.C., and D.G. Grier. 1996. Methods of Digital Video Microscopy for Colloidal Studies. J. Colloid Interface Sci. 179: 298–310.

103. Boehm, H., T. a. Mundinger, C.H.J. Boehm, V. Hagel, U. Rauch, et al. 2009. Mapping the mechanics and macromolecular organization of hyaluronan-rich cell coats. Soft Matter. 5: 4331.

104. Röck, K., K. Fischer, and J.W. Fischer. 2010. Hyaluronan Used for Intradermal Injections Is Incorporated into the Pericellular Matrix and Promotes Proliferation in Human Skin Fibroblasts in vitro. Dermatology. 221: 219–228.

105. Wang, D., and J. Fawcett. 2012. The perineuronal net and the control of CNS plasticity. Cell Tissue Res. 349: 147–160.

106. Knudson, C.B., and B.P. Toole. 1985. Changes in the pericellular matrix during differentiation of limb bud mesoderm. Dev. Biol. 112: 308–318.

107. Auvinen, P., R. Tammi, J. Parkkinen, M. Tammi, U. Agren, et al. 2000. Hyaluronan in peritumoral stroma and malignant cells associates with breast cancer spreading and predicts survival. Am. J. Pathol. 156: 529–536.

108. Kimata, K., Y. Honma, M. Okayama, and H. Metastatic. 1983. Increased Synthesis of Hyaluronic Acid by Mouse Mammary Carcinoma Cell Variants with High Metastatic Potential Increased Synthesis of Hyaluronic Acid by Mouse Mammary Carcinoma Cell. : 1347–1354.

109. Bernert, B., H. Porsch, and P. Heldin. 2011. Hyaluronan synthase 2 (HAS2) promotes breast cancer cell invasion by suppression of tissue metalloproteinase inhibitor 1 (TIMP-1). J. Biol. Chem. 286: 42349–42359.

110. Wight, T.N. 2002. Versican: a versatile extracellular matrix proteoglycan in cell biology. Curr. Opin. Cell Biol. 14: 617–623.

111. Wight, T.N., B.P. Toole, and V.C. Hascall. 2011. Hyaluronan and the Aggregating

Proteoglycans. In: Mecham PR, editor. The Extracellular Matrix: an Overview. Berlin, Heidelberg: Springer Berlin Heidelberg. pp. 147–195.

112. Weigel, P.H. 1998. Bacterial hyaluronan synthases. Sci. hyaluronan today. Available online www. GlycoForum. gr. ip. .

113. Knudson, C.B. 1993. Hyaluronan receptor-directed assembly of chondrocyte pericellular matrix. J. Cell Biol. 120: 825–834.

114. IyerS., G. M., Subba-RaoV., W. D., and I. Sokolov. 2009. Atomic force microscopy detects differences in the surface brush of normal and cancerous cells. Nat Nano. 4: 389–393.

115. Simon, M., M. Dokukin, V. Kalaparthi, E. Spedden, I. Sokolov, et al. 2016. Load Rate and Temperature Dependent Mechanical Properties of the Cortical Neuron and Its Pericellular Layer Measured by Atomic Force Microscopy. Langmuir. 32: 1111–1119.

116. Evanko, S.P., P.Y. Johnson, K.R. Braun, C.B. Underhill, J. Dudhia, et al. 2001. Platelet-Derived Growth Factor Stimulates the Formation of Versican-Hyaluronan Aggregates and Pericellular Matrix Expansion in Arterial Smooth Muscle Cells. Arch. Biochem. Biophys. 394: 29–38.

117. Attili, S., and R.P. Richter. 2013. Self-assembly and elasticity of hierarchical proteoglycan–hyaluronan brushes. Soft Matter. 9: 10473.

118. Souslov, A., J.E. Curtis, and P.M. Goldbart. 2015. Beads on a string: structure of bound aggregates of globular particles and long polymer chains. Soft Matter. 11: 8092–8099.

119. Milner, S.T., T.A. Witten, and M.E. Cates. 1988. Theory of the grafted polymer brush. Macromolecules. 21: 2610–2619.

120. Milner, S.T. 1991. Polymer brushes. Artic. Feb. 22.

121. Johnson, M., R. Kamm, C. Ethier, and T. Pedley. 1987. Scaling laws and the effects of concentration polarization on the permeability of hyaluronic acid. Physicochem Hydrodyn. .

122. Cohen, M., E. Klein, B. Geiger, and L. Addadi. 2003. Organization and Adhesive Properties of the Hyaluronan Pericellular Coat of Chondrocytes and Epithelial Cells. Biophys. J. 85: 1996–2005.

123. Attili, S., and R.P. Richter. 2012. Combining Colloidal Probe Atomic Force and Reflection Interference Contrast Microscopy to Study the Compressive Mechanics of Hyaluronan Brushes. Langmuir. 28: 3206–3216.

124. Seror, J., Y. Merkher, N. Kampf, L. Collinson, A.J. Day, et al. 2011. Articular Cartilage Proteoglycans As Boundary Lubricants: Structure and Frictional Interaction of Surface-Attached Hyaluronan and Hyaluronan–Aggrecan Complexes. Biomacromolecules. 12: 3432–3443.

125. Knudson, W., D.J. Aguiar, Q. Hua, and C.B. Knudson. 1996. CD44-anchored hyaluronan-rich pericellular matrices: an ultrastructural and biochemical analysis. Exp. Cell Res. 228: 216–28.

126. Knudson, C.B., and W. Knudson. 2001. Cartilage proteoglycans. Semin. Cell Dev. Biol. 12: 69–78.

127. de Gennes, P.G. 1980. Conformations of Polymers Attached to an Interface.

Macromolecules. 13: 1069–1075.

128. Zhou, R., B. Xiong, Y. He, and E.S. Yeung. 2010. Slowed diffusion of single nanoparticles in the extracellular microenvironment of living cells revealed by darkfield microscopy. Anal. Bioanal. Chem. 399: 353–359.

129. Xu, R., B. Xiong, R. Zhou, H. Shen, E.S. Yeung, et al. 2014. Pericellular matrix plays an active role in retention and cellular uptake of large-sized nanoparticles. Anal. Bioanal. Chem. 406: 5031–5037.

130. Yaron, M., I. Yaron, O. Smetana, E. Eylan, and M. Herzberg. 1976. Hyaluronic acid produced by human synovial fibroblasts. Effect of polyinosinic-polycytidylic acid (POLY I:C) and interferon. Arthritis Rheum. 19: 1315–1320.

131. Record, M., K. Carayon, M. Poirot, and S. Silvente-Poirot. 2014. Exosomes as new vesicular lipid transporters involved in cell–cell communication and various pathophysiologies. Biochim. Biophys. Acta - Mol. Cell Biol. Lipids. 1841: 108–120.

132. Raposo, G., and W. Stoorvogel. 2013. Extracellular vesicles: Exosomes, microvesicles, and friends. J. Cell Biol. . 200: 373–383.

133. Tian, T., Y. Wang, H. Wang, Z. Zhu, and Z. Xiao. 2010. Visualizing of the cellular uptake and intracellular trafficking of exosomes by live-cell microscopy. J. Cell. Biochem. 111: 488–496.

134. Ng, L., A.J. Grodzinsky, P. Patwari, J. Sandy, A. Plaas, et al. 2003. Individual cartilage aggrecan macromolecules and their constituent glycosaminoglycans visualized via atomic force microscopy. J. Struct. Biol. 143: 242–257.

135. Pizzorusso, T., P. Medini, N. Berardi, S. Chierzi, J.W. Fawcett, et al. 2002. Reactivation of Ocular Dominance Plasticity in the Adult Visual Cortex. Science (80-.). 298: 1248–1251.

136. Brecht, M., U. Mayer, E. Schlosser, and P. Prehm. 1986. Increased hyaluronate synthesis is required for fibroblast detachment and mitosis. Biochem. J. 239: 445–50.

137. van Oosten, A.S., and P.A. Janmey. 2013. Extremely charged and incredibly soft: physical characterization of the pericellular matrix. Biophys. J. 104: 961–3.

138. Laabs, T., D. Carulli, H.M. Geller, and J.W. Fawcett. 2005. Chondroitin sulfate proteoglycans in neural development and regeneration. Curr. Opin. Neurobiol. 15: 116–120.

139. Mark, M.P., J.R. Baker, K. Kimata, and J.-V. Ruch. 1990. Regulated changes in chondroitin sulfation during embryogenesis: an immunohistochemical approach. Int J Dev Biol. 34: 191–204.

140. Morgenstern, D.A., R.A. Asher, and J.W. Fawcett. 2002. Chondroitin sulphate proteoglycans in the CNS injury response. Prog. Brain Res. 137: 313—332.

141. Galtrey, C.M., and J.W. Fawcett. 2007. The role of chondroitin sulfate proteoglycans in regeneration and plasticity in the central nervous system. Brain Res. Rev. 54: 1–18.

142. Knudson, C., and W. Knudson. 1993. Hyaluronan-binding proteins in development, tissue homeostasis, and disease. FASEB J. 7: 1233–1241.

143. Shi, S., S. Grothe, Y. Zhang, M.D. O'Connor-McCourt, a R. Poole, et al. 2004. Link protein has greater affinity for versican than aggrecan. J. Biol. Chem. 279: 12060–6.

144. Papagiannopoulos, A., T.A. Waigh, T. Hardingham, and M. Heinrich. 2006. Solution Structure and Dynamics of Cartilage Aggrecan. Biomacromolecules. 7: 2162–2172.

145. Lei, J., L.T. McLane, J.E. Curtis, and J.S. Temenoff. 2014. Characterization of a multilayer heparin coating for biomolecule presentation to human mesenchymal stem cell spheroids. Biomater. Sci. 2: 666.

146. Baranova, N.S., E. Nilebäck, F.M. Haller, D.C. Briggs, S. Svedhem, et al. 2011. The inflammation-associated protein TSG-6 cross-links hyaluronan via hyaluronan-induced TSG-6 oligomers. J. Biol. Chem. 286: 25675–86.

147. Baranova, N.S., S.J. Foulcer, D.C. Briggs, V. Tilakaratna, J.J. Enghild, et al. 2013. Inter-α-inhibitor impairs TSG-6-induced hyaluronan cross-linking. J. Biol. Chem. 288: 29642–29653.

148. Baranova, N.S., A. Inforzato, D.C. Briggs, V. Tilakaratna, J.J. Enghild, et al. 2014. Incorporation of pentraxin 3 into hyaluronan matrices is tightly regulated and promotes matrix cross-linking. J. Biol. Chem. 289: 30481–30498.

149. Limozin, L., and K. Sengupta. 2009. Quantitative reflection interference contrast microscopy (RICM) in soft matter and cell adhesion. ChemPhysChem. 10: 2752–2768.

150. García, A.J., P. Ducheyne, and D. Boettiger. 1997. Quantification of cell adhesion using a spinning disc device and application to surface-reactive materials. Biomaterials. .

151. Gallant, N.D., and A.J. Garcia. 2005. Cell Adhesion Strengthening: Contributions of Adhesive Area, Integrin Binding, and Focal Adhesion Assembly. Mol. Biol. Cell. 16: 4329–4340.

152. Rigden, D.J., and M.J. Jedrzejas. 2003. Structures of streptococcus pneumoniae hyaluronate lyase in complex with chondroitin and chondroitin sulfate disaccharides: Insights into specificity and mechanism of action. J. Biol. Chem. 278: 50596–50606.

153. Pasapera, A.M., I.C. Schneider, E. Rericha, D.D. Schlaepfer, and C.M. Waterman. 2010. Myosin II activity regulates vinculin recruitment to focal adhesions through FAK-mediated paxillin phosphorylation. J. Cell Biol. 188: 877–890.

154. Bhadriraju, K., M. Yang, S. Alom Ruiz, D. Pirone, J. Tan, et al. 2007. Activation of ROCK by RhoA is regulated by cell adhesion, shape, and cytoskeletal tension. Exp. Cell Res. 313: 3616–3623.

155. Choi, C.K., M. Vicente-Manzanares, J. Zareno, L.A. Whitmore, A. Mogilner, et al. 2008. Actin and alpha-actinin orchestrate the assembly and maturation of nascent adhesions in a myosin II motor-independent manner. Nat. Cell Biol. 10: 1039–50.

156. Kakizaki, I., K. Kojima, K. Takagaki, M. Endo, R. Kannagi, et al. 2004. A novel mechanism for the inhibition of hyaluronan biosynthesis by 4-methylumbelliferone. J. Biol. Chem. 279: 33281–9.

157. Vigetti, D., A. Genasetti, E. Karousou, M. Viola, M. Clerici, et al. 2009. Modulation of hyaluronan synthase activity in cellular membrane fractions. J. Biol. Chem. 284: 30684–30694.

158. Raedler, J., H. Strey, and E. Sackmann. 1995. Phenomenology and Kinetics of Lipid Bilayer Spreading on Hydrophilic Surfaces. Langmuir. 11: 4539–4548.

159. Barr, V.A., S.C. Bunnell, V.A. Barr, and S.C. Bunnell. 2009. Interference Reflection Microscopy. In: Current Protocols in Cell Biology. Hoboken, NJ, USA: John Wiley & Sons, Inc. p. 4.23.1-4.23.19.

160. Parsons, J.T., A.R. Horwitz, and M.A. Schwartz. 2010. Cell adhesion: integrating cytoskeletal dynamics and cellular tension. Nat. Rev. Mol. cell Biol. 11: 633–643.

161. Shyjan, A.M., P. Heldin, E.C. Butcher, T. Yoshino, and M.J. Briskin. 1996. Functional cloning of the cDNA for a human hyaluronan synthase. J. Biol. Chem. 271: 23395–23399.

162. Ishizuka, S., E.B. Askew, N. Ishizuka, C.B. Knudson, and W. Knudson. 2016. 4-Methylumbelliferone Diminishes Catabolically-Activated Articular Chondrocytes and Cartilage Explants Via a Mechanism Independent of Hyaluronan Inhibition. J. Biol. Chem. 291: jbc.M115.709683.

163. Zimmerman, E., B. Geiger, and L. Addadi. 2002. Initial Stages of Cell-Matrix Adhesion Can Be Mediated and Modulated by Cell-Surface Hyaluronan. Biophys. J. 82: 1848–1857.

164. Hautanen, A., J. Gailit, D.M. Mann, and E. Ruoslahti. 1989. Effects of modifications of the RGD sequence and its context on recognition by the fibronectin receptor. J. Biol. Chem. 264: 1437–1442.

165. Garcia, A.J., P. Ducheyne, and D. Boettiger. 1997. Cell Adhesion Strength Increases Linearly with Adsorbed Fibronectin Surface Density. Tissue Eng. 3: 197–206.

166. Yamagata, M., S. Suzuki, S.K. Akiyama, K.M. Yamada, and K. Kimata. 1989. Regulation of cell-substrate adhesion by proteoglycans immobilized on extracellular substrates. J. Biol. Chem. 264: 8012–8018.

167. Ricciardelli, C., A.J. Sakko, M.P. Ween, D.L. Russell, and D.J. Horsfall. 2009. The biological role and regulation of versican levels in cancer. Cancer Metastasis Rev. 28: 233–45.

168. Papagiannopoulos, A., T.A. Waigh, H. T., and M. Heinrich. 2006. Solution Structure and Dynamics of Cartilage Aggrecan. Biomacromolecules. 7: 2162–2172.

169. Aruffo, A., I. Stamenkovic, M. Melnick, C.B. Underhill, and B. Seed. 1990. CD44 is the principal cell surface receptor for hyaluronate. Cell. 61: 1303–1313.

170. Naujokas, M.F., M. Morin, M.S. Anderson, M. Peterson, and J. Miller. 1993. The chondroitin sulfate form of invariant chain can enhance stimulation of T cell responses through interaction with CD44. Cell. 74: 257–268.

171. Ponta, H., L. Sherman, and P.A. Herrlich. 2003. CD44: from adhesion molecules to signalling regulators. Nat. Rev. 4.

172. Rodriguez, L.G., X. Wu, and J.-L. Guan. 2005. Wound-Healing Assay. In: Guan J-L, editor. Cell Migration: Developmental Methods and Protocols. Totowa, NJ: Humana Press. pp. 23–29.

173. Wang, C., M. Tammi, H. Guo, and R. Tammi. 1996. Hyaluronan distribution in the normal epithelium of esophagus, stomach, and colon and their cancers. Am. J. Pathol. 148: 1861–9.

174. Riessen, R., T.N. Wight, C. Pastore, C. Henley, and J.M. Isner. 1996. Distribution of Hyaluronan During Extracellular Matrix Remodeling in Human Restenotic Arteries and

Balloon-Injured Rat Carotid Arteries. Circulation. 93.

175. Jeppesen, C., J.Y. Wong, T.L. Kuhl, J.N. Israelachvili, N. Mullah, et al. 2001. Impact of Polymer Tether Length on Multiple Ligand-Receptor Bond Formation. Science (80-.). 293.

176. Evans, E.A., and D.A. Calderwood. 2007. Forces and Bond Dynamics in Cell Adhesion. Science (80-.). 316.

177. Culty, M., M. Shizari, E.W. Thompson, and C.B. Underhill. 1994. Binding and degradation of hyaluronan by human breast cancer cell lines expressing different forms of CD44: Correlation with invasive potential. J. Cell. Physiol. 160: 275–286.

178. Bohrer, L.R., P. Chuntova, L.K. Bade, T.C. Beadnell, R.P. Leon, et al. 2014. Activation of the FGFR–STAT3 Pathway in Breast Cancer Cells Induces a Hyaluronan-Rich Microenvironment That Licenses Tumor Formation. Cancer Res. 74.

179. Wu, M., M. Cao, Y. He, Y. Liu, C. Yang, et al. 2015. A novel role of low molecular weight hyaluronan in breast cancer metastasis. FASEB J. 29: 1290–8.

180. Théry, M., and M. Piel. 2009. Adhesive micropatterns for cells: A microcontact printing protocol. Cold Spring Harb. Protoc. 4: 1–11.

181. Cai, A.Q., K.A. Landman, and B.D. Hughes. 2007. Multi-scale modeling of a wound-healing cell migration assay. J. Theor. Biol. 245: 576–594.

182. Yarrow, J.C., Z.E. Perlman, N.J. Westwood, T.J. Mitchison, M. Wong, et al. 2004. A high-throughput cell migration assay using scratch wound healing, a comparison of image-based readout methods. BMC Biotechnol. 4: 21.

183. Liang, C.-C., A.Y. Park, and J.-L. Guan. 2007. In vitro scratch assay: a convenient and inexpensive method for analysis of cell migration in vitro. Nat. Protoc. 2: 329–333.

184. Nie, F.-Q., M. Yamada, J. Kobayashi, M. Yamato, A. Kikuchi, et al. 2007. On-chip cell migration assay using microfluidic channels. Biomaterials. 28: 4017–4022.

185. Heit, B., and P. Kubes. 2011. Measuring Chemotaxis and Chemokinesis : The Under-Agarose Cell Migration Assay MATERIALS EQUIPMENT RECIPES. 2003.

186. Salaita, K., K. Galior, Y. Liu, K. Yehl, and S. Vivek. 2015. Titin-based Nanoparticle Tension Sensors Map High-Magnitude Integrin Forces within Focal Adhesions. Nano Lett. : acs.nanolett.5b03888.